Optoelectronic properties of 2-dimensional materials

Grant Aivazian

A dissertation
submitted in partial fulfillment of the
requirements for the degree of

Doctor of Philosophy

University of Washington

2015

Reading Committee:

Xiaodong Xu, Chair

David Cobden

Paul Wiggins

Program Authorized to Offer Degree:
Department of Physics

University of Washington

Abstract

Optoelectronic properties of 2-dimensional materials

Grant Aivazian

Chair of the Supervisory Committee:
Assistant Professor Xiaodong Xu
Department of Physics

Layered materials when thinned down to their monolayer limit exhibit remarkable properties owing to their two-dimensional nature and strong electron confinement. In particular this class of materials displays strong optical properties, showing promise for applications towards future optoelectronic devices; however, due to their relative recent isolation, the optical properties of these monolayers have been largely unexplored. This thesis focuses on the interaction of these layered materials with incident optical radiation, with the focus being on monolayers of WSe_2 and graphene.

In the first half of this thesis the strong excitonic physics of semiconducting WSe_2 monolayers is investigated. These excitons exhibit large interaction effects due to the strong 2D confinement which are further explored here using ultrafast pump probe techniques. Additionally these excitons possess a unique quantum degree of freedom, known as the valley pseudospin. It has been shown that this pseudospin can be optically addressed and readout using its unique circular dichroism. Here the degenerate pseudospin is controlled using an external magnetic field coupled to its valley pseudospin magnetic moment. From this work the valley pseudospin in monolayer WSe_2 can be further explored as a possible qubit in future quantum computing and quantum information applications.

Graphene photodetectors are the focus of the second half of the thesis. Monolayer graphene is a gapless semi-metal that has been shown to display an ultrafast optoelectronic response that is dominated by hot carriers. Here these effects are investigated as a band gap

is generated through the application of a perpendicular electric field in bilayer graphene and through the application of a perpendicular magnetic field in monolayer graphene inducing a Landau level quantization of the band structure. It is observed that in both cases the disruption of the continuous band structure has profound impacts on the photo-excited hot carriers. This work helps lay the foundation for future ultrafast photodetectors made out of graphene.

TABLE OF CONTENTS

LIST OF FIGURES

ABBREVIATIONS

AOM: Acousto-optic modulator

BN: Boron nitride

BG: Bottom gate

FET: Field effect transistor

HWP: Half wave plate

LL: Landau Level

PC: Photocurrent

PL: Photoluminescence

QHE: Quantum Hall Effect

QWP: Quarter wave plate

TG: Top gate

TMD: Transistion metal dichalcoginide

WSe_2 : Tungsten Diselenide

τ_Z: Valley index

$\hat{\sigma}$: Valley pseudospin

ACKNOWLEDGMENTS

An undertaking as daunting as a doctorate certainly cannot be accomplish alone. I have many people to thank for helping me get through all of this.

First and foremost is my advisor, Xiaodong Xu. He made sure to keep me busy and to keep me funded. I've learned so much through his guidance and support.

I greatly appreciate all the comments and criticisms from my reading committee, David Cobden and Paul Wiggins. Its good to know someone will have read this thing. Thanks also to my other committee members, Anton Andreev, Sanjay Reddy, and Stefan Stoll.

Thank you also to all the members of the Xu lab, past and present. For all the learning, and teaching, and sitting together in the dark, I thank you.

Thank you to all of my friends who helped keep me sane over the years of grad school, from my old buddies is Colorado to the new ones in Seattle, you know who you are. Thanks for all the beer, and board games, and BBQ. Thanks for all the camping, and climbing, and car trips. Its definitely been fun these last few years!

Big shout out to Mama and Papa Aivazian for all of the support, and love, and cookies. To Reed and Meggie for keeping my liberalism in check. To the Bryants for letting me join the family and quietly accepting the delayed grandchildren.

And finally thanks to The Mrs. for all the fun and the laughs. And for making me get this dang thesis done.

DEDICATION

to Wylie,

for always greeting me at the door with a ball and a wagging tail

Chapter 1

INTRODUCTION TO 2-DIMENSIONAL MATERIALS

Since the isolation of a single layer of graphene from a layered graphite source in 2004 [55, 53], the study of two-dimensional layered materials has exploded with both popularity and beautiful results. Bulk crystals of these layered materials can be thought of like a ream of paper: composed of many individual sheets which are strongly bound in-plane, though only weakly bound, via van der Waals forces, between sheets. These crystals have interesting properties in their own right, but with minimal effort, using mechanical exfoliation (the so called "scotch-tape method" [54]), a single layer may be isolated displaying remarkably different properties than the host crystal.

Electrons in these materials are absolutely confined in the out of plane direction leading to some very interesting quantum physics arising from their two-dimensional nature. Additionally, since these materials are all surface area they are particularly sensitive to changes in their environment; for instance as sensors for chemicals absorbed onto their surfaces, or, as will be the focus of this thesis, as sensors for incident light. Finally, they may be easily stacked on top of each other to form vertical heterostructures [19, 60]. Since different layered materials act as metals, insulators, semiconductors, or superconductors in their monolayer limit [55], different heterostructures of different materials can run the full spectrum of imaginable device architectures [16, 26].

Two of the most interesting of such materials for optoelectronic applications will be investigated in this thesis: graphene and semiconducting transition metal dichalcoginides, namely WSe_2 .

1.1 Graphene

Monolayer graphene is composed of a single sheet of carbon atoms arranged in a honeycomb lattice. It has been shown over the years to display many remarkable electronic properties [8,

18] such as world record electron mobilities [16] and a unique quantum hall effect (which has even been demonstrated at room temperature [56]). Additionally it can easily be fabricated into, even complicated, device architectures using standard clean room techniques.

It is not obvious, however, that graphene would respond well to optical excitation, being only one atom thick. Remarkably, graphene has been shown to display a broadband absorption of 2.3% [5], which, obviously, isn't acceptable for an energy harvesting application but is surprisingly large for being only one atom thick. Graphene photodetectors have been shown to exhibit reasonable responsivities and ultrafast response times to optical excitation [36, 50, 82, 97], making them promising candidates for ultrafast photomodulators and detectors.

Graphene's biggest weakness for its use in converting absorbed radiation to an electrical signal is its lack of a band gap. Photoexcited electron/hole pairs have little inhibiting them from recombining and wasting their absorbed energy into heating the lattice. However gaps in the continuous band structure can be produced by applying a perpendicular electric field in bilayer graphene [47] or a perpendicular magnetic field in monolayer graphene [20]. The optoelectronic properties in these regimes will be investigated in this thesis.

1.2 TMDs

Monolayer transition metal dichalcoginides (TMDs), such as WSe_2 , are a semiconducting cousin of graphene. In these materials a layer of group VI transition metal atoms (such as W or Mo) is sandwiched between two layers of chalcogen atoms (S or Se) in a hexagonal lattice [55], explicitly breaking inversion symmetry resulting in a band gap in the 1.2-2.5 eV (near IR- visible) range. The presence of the band gap gives these materials a strong absorption resonance dominated by excitons [25, 59]. These properties have led to the demonstration of LEDs based on a pn-junction in WSe_2 [62].

Additionally, electrons in TMDs have an extra quantum mechanical degree of freedom, the valley index, which can be described in a similar manor as the spin, giving rise to the so call "valley pseudospin" [92]. Already much work has been done in demonstrating a valley polarization, coherence [95], and even the valley hall effect [41]. With further development this pseudospin can be expanded into a qubit for quantum computing or information

applications.

1.3 Thesis Organization

This thesis explores several different responses of these 2D materials to optical excitations. In Part I different spectroscopic methods are used to examine the excitonic nature of monolayer WSe_2 . Chapter 2 will cover the basic properties of TMDs, namely WSe_2 , including its excitonic and valley physics. In Chapter 3 the lifetimes and many-body interactions of excitons in WSe_2 are explored using an ultrafast resonant pump-probe spectroscopy experiment. The final chapter of Part I covers the use of an external magnetic field to control the valley pseudospin in WSe_2 . Part II covers the optical excitation of photocurrents in graphene FETs, particularly their ultrafast generation, using a pump-probe photocurrent experiment. Chapter 5 explores this effect in semi-metallic single layer graphene PN junctions. What happens to the photocurrent generation when the continuous band structure of semi-metallic graphene is broken is investigated in Chapters 6 and 7 by opening up a band gap in bilayer graphene and by forming discretely quantized Landau Levels using an external magnetic field, respectively.

Part I

VALLEY EXCITONS IN MONOLAYER TUNGSTEN DISELENIDE

Chapter 2

EXCITONS AND VALLEY PSEUDOSPIN IN TMDS

TMDs are layered semiconductors that show rich optical properties as monolayers. This chapter will explore some of these fundamental characteristics from the literature including the direct band gap, bright excitons, and valley pseudospin. Much of this work was done in the Xu lab. While most of these properties are true for many different species of TMDs, the work of this thesis will focus entirely on WSe_2 as it displays some of the best excitonic lines with large circular dichrosim. In the next chapter the lifetime and ultrafast interactions of excitons in WSe_2 will be measured. Chapter 4 will then look at using an external magnetic field as a knob to control the valley pseudospin.

2.1 Structure

When thinned down to a single layer, TMDs are three atoms thick: composed of a group VI transition metal atom sandwiched in between two sheets of chalcogen atoms in a honeycomb lattice. This is shown in the Fig 2.1 for WSe_2 .

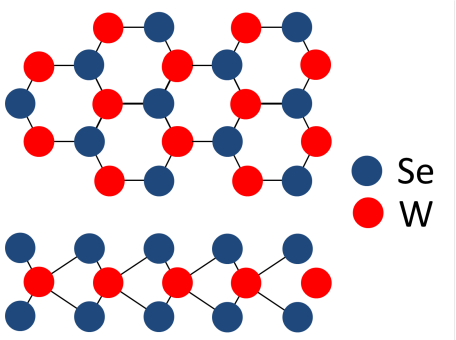

Figure 2.1: Schematic of WSe_2 structure from the top (top figure) and the side (bottom figure). Hexagonal lattice has inversion symmetry explicitly broken.

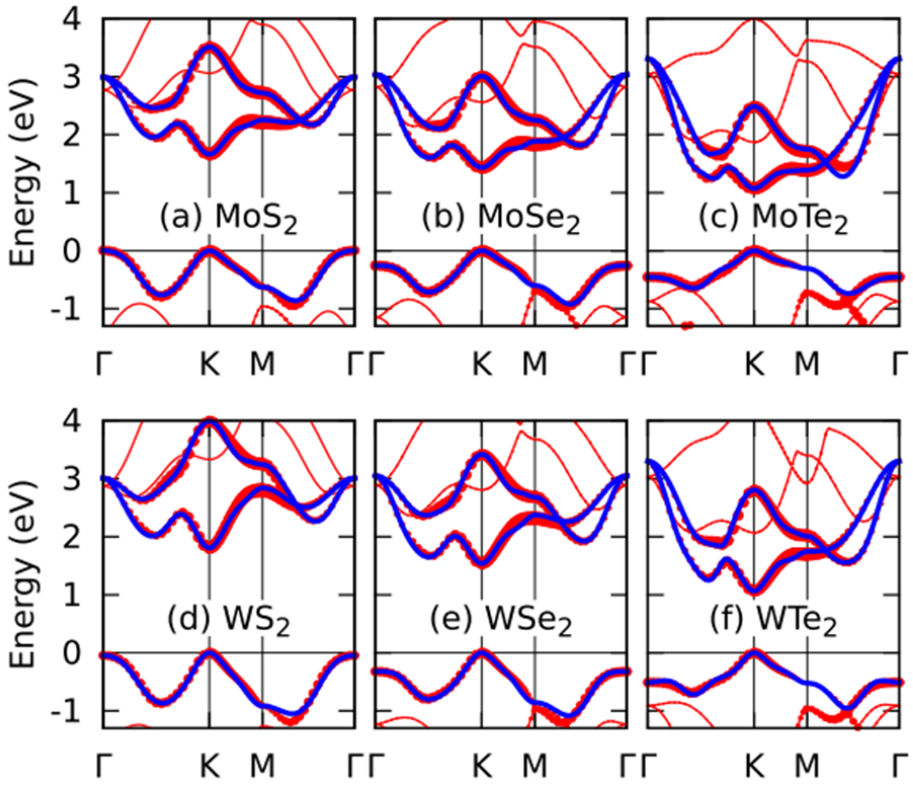

Figure 2.2: DFT calculation of TMD band structures. Red lines are full first principle calculations, blue curves are from simplified tight binding model, and red dotes are from the three band model. Image taken from Ref [38]

It is evident that in this form the crystal has broken inversion symmetry. This property allows for the existence of a direct band gap in the material. Indeed first principle calculations show this to be the case [38, 106, 9] (see Fig 2.2), with the band extrema at the K points at the edge of the first Brillouin zone. Additionally, this optically active direct band gap has been confirmed in several materials using photoluminescent spectroscopy [45, 72] (see section 4.1 for experimental details of PL spectroscopy). Fig 2.3 shows the spectra obtained from molybdenum disulfide crystals of various thicknesses [45]. Clearly the signal from the monolayer sample is pronounced compared to the thicker samples demonstrating that only with inversion symmetry strongly broken, as in the monolayer case, will an optically active band gap form and photoluminescence appear. In the presence of inversion symmetry, as

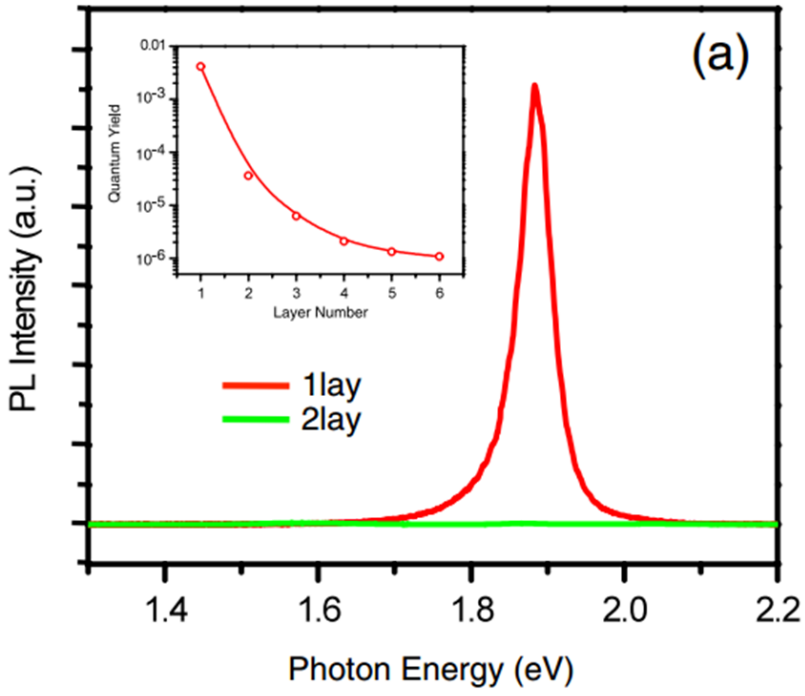

Figure 2.3: Photoluminescent spectrum taken from 1- and 2-layer MoS_2 samples. Inset shows strong quenching of the PL peak with increasing layer thickness. Image taken from Ref [45]

for thicker samples, the crystals form an indirect band gap that is not optically active.

Unique physics arises from the fact that the band edges are at the edge of the first Brillouin zone. These points, called the K points in crystallography, at the corners of the hexagonal lattice form two inequivalent, but degenerate sets: the +K and -K points. This added two-fold degeneracy can be treated as a spin-1/2 pseudospin, $\hat{\sigma}$, dubbed the valley pseudospin after the electronic energy valleys of the band structure at these points [99, 93, 95, 92]. As will be shown in the following sections these valleys can be individually addressed with circularly polarized light and the energy degeneracy can be controlled with an externally applied magnetic field. With this addressability and control one can imagine using the valley pseudospin as an information carrier, analogous to the electron spin in the burgeoning field of spintronics, to form valley-based electronics systems, or valleytronics.

TMDs appear to the be ideal platform for developing such systems, but there is much investigative work to be done first to define and explain the properties of their valleys.

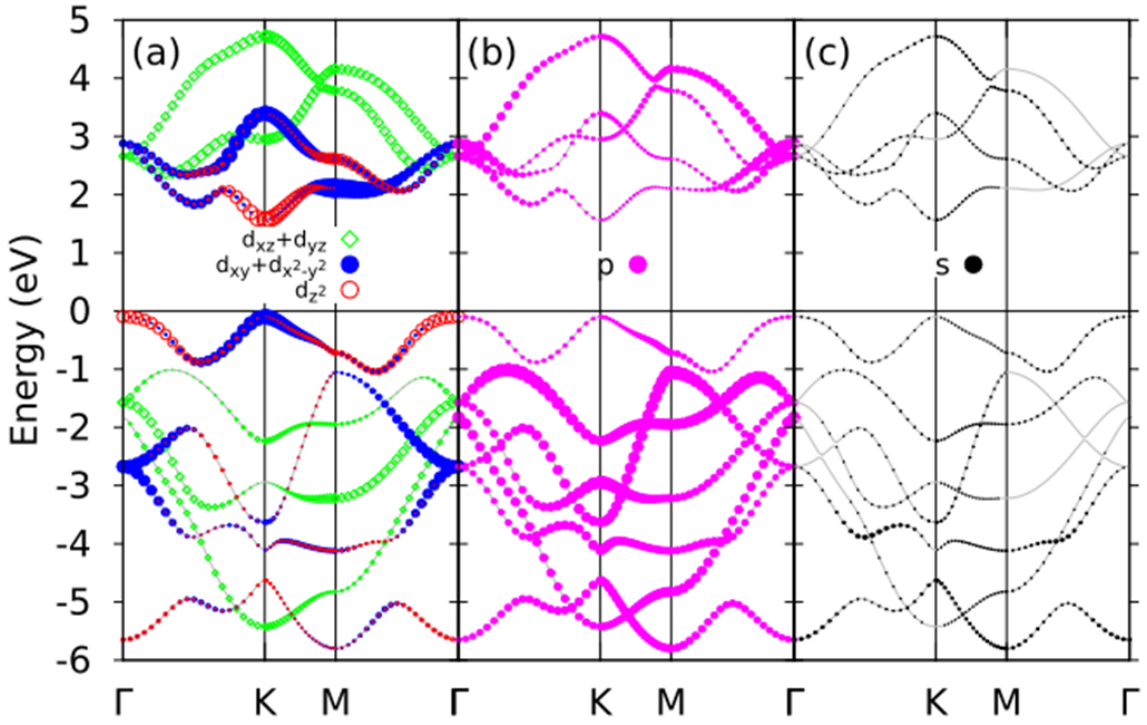

Figure 2.4: Relative contributions of individual atomic orbitals to the band structure of MoS_2. Image taken from Ref [38]

Low energy physics around the K points can be describe very effectively using a three band model [38]. Fig 2.4 shows the band structure of MoS_2 where the relative contribution of each of the individual atomic orbitals to the total band structure is portrayed by the dot size. Near band edges at the K points the dominant contributions are from the d_{z^2} (red) and the $d_{xy}+d_{x^2-y^2}$ (blue) orbitals in the left subfigure. By just considering these atomic contribution in the DFT calculations a very accurate representation of the whole band structure can be computed (see Fig 2.2). Additionally, these d orbitals contain significant amount of angular momentum. Since these crystal are monolayers, the symmetry is broken such that the magnetic quantum number, m, of these orbitals describes the amount of angular

momentum in the z-direction (out of plane). The d_{z^2} (red) orbitals which predominately make up the conduction band have $m = 0$, whereas the $d_{xy} + d_{x^2-y^2}$ (blue) orbitals which comprise the valence band have $|m| = 2$. In addition to this extra angular momentum in the out of plane direction associated with these parent atomic orbitals, the bands also acquire a nonzero magnetic moment which will be of particular interest for magnetic control of the valley pseudospin as described in Chapter 4.

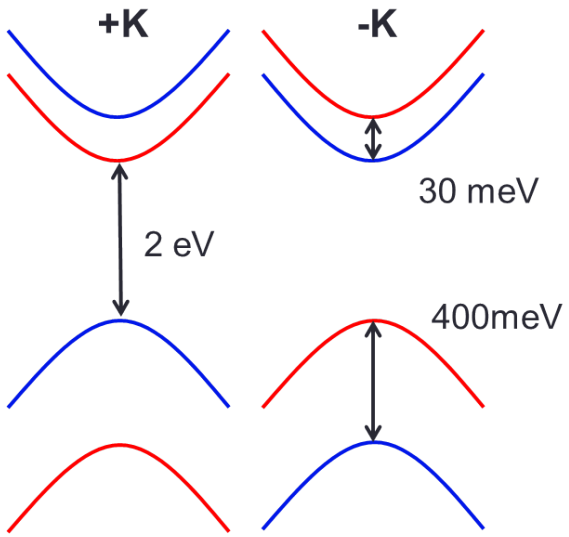

Figure 2.5: Low energy band structure of WSe_2 showing band splitting due to spin orbit coupling. The blue (red) bands are spin up (down).

Thanks in part to the high-Z nucleus of the transition metal atoms, spin orbit coupling effects play a major role in TMDs [38, 106]. Both the conduction and valence band are spin split, with opposite splitting of the bands in the opposite valleys. The splitting of the low energy band structure around the K points for WSe_2 is shown in Fig 2.5, where the blue (red) bands denote spin up (down). Clearly the band gap is the largest energy scale here ($\sim$2 eV); however, the splitting of the valence band is so large ($\sim$400 meV) that for most low energy optical excitations we can neglect the lower spin split valence band. The conduction band splitting of $\sim$30 meV is much smaller, and one must still consider the higher energy band; especially since optical transitions in WSe_2 conserve spin. Therefore, the dominate

low energy, optical transition in the +K valley is from spin up band (blue) to spin up as shown in the left panel of Fig 2.8.

2.2 Excitonic Properties

Optical excitation above the band gap in direct gap semiconductors leads to the formation of an electron population in the bottom of the conduction band and a population of positively charged holes in the top of the valence band. The Coulomb attraction between these two types of particles can result in a neutral bound state called an exciton (denoted X^o) with energy less than the band gap energy by the exciton binding energy, E_B. The formation of excitons is typically very fast, so the optical properties of these types of semiconductors are dominated by the excitons. Furthermore, if the semiconductor is heavily doped, say with extra electrons, when forming excitons after optical excitation there will be leftover electrons who, when unscreened, have strong Coulomb repulsion. It becomes energetically favorable at some doping level for excitons to bind an extra electron (see Fig 2.6), to benefit from the Coulomb screening of the hole, and form a charged, three-body bound state, the electron trion (X^-), with an energy of the exciton energy less a charging energy, E_C. Similarly in

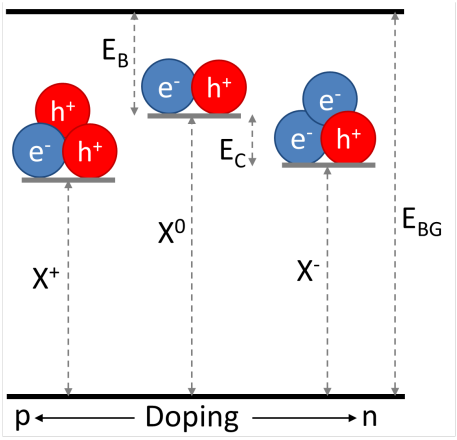

Figure 2.6: Schematic of electron and hole configuration in neutral and charged excitons versus the doping of the crystal. Relevant energies are denoted: band gap energy,E_{BG}; exciton binding energy, E_B; trion charging energy, E_C; exciton and trion energies.

a hole doped system a positively charged hole trion (X^+) can form. The charging energy of these two charged exciton species, in general, need not be the same, and is given by the relative effective mass of the electron and the hole.

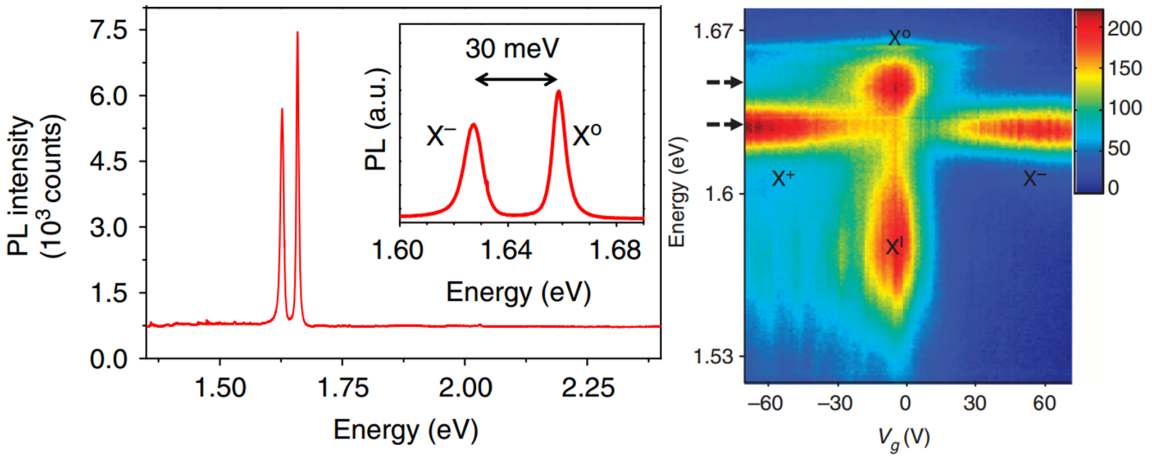

Figure 2.7: Photoluminescence of exciton species in $MoSe_2$. Left: typical PL spectra near neutral doping showing an exciton (right) and trion (left). Spectra is expanded in the inset for clarity. Right: PL map as a function of the gate voltage showing the transition between dominant exciton species. Image taken from Ref [63]

In TMDs, strong excitonic properties have been observed. Due to their 2-D nature the Coulomb interaction is exceptionally strong, resulting in very large binding energies and sharp, well-defined exciton/trion spectra typically measured with PL spectroscopy[43, 63, 28]. In Fig 2.7, the typical low temperature (T=20K) PL spectrum of monolayer $MoSe_2$ is shown in the left panel [63]. Two well defined peaks are observed which can be attributed to an exciton and trion. By applying a gate voltage to dope the system from a near neutral state to either a strongly p or n doped system the trion signal becomes more prominent than the exciton. This is shown in the right panel of Fig 2.7. The vertical axis is the energy of PL emission, while the bottom axis is voltage applied to the gate. The different excitonic species present at each doping (gate) level are clearly marked. The lowest energy peak, denoted X^I is thought the be result of impurity bound excitons. In $MoSe_2$ the emission

energy of both the X- and X+ peaks are identical, indicating that the effective mass of the electron and the hole are the same in this system, again, this is not strictly necessary.

As was mentioned before these excitons can exist in one of two valleys at the K points, forming a degenerate pair. The Coulomb exchange interaction between the electrons and holes of the excitons in the two valleys will act to couple the two valley configurations [100]. This leads to an effective interaction between the exciton's center of mass momentum, $\mathbf{k}$, and its valley pseudospin, $\hat{\sigma}$, shown in the left panel of Fig 2.8. The strength of this interaction, V_k, is given by the product of the momentum squared and the Fourier transform of the Coulomb potential, $V_C(k)$ (See Ref [100]). In TMDs the Coulomb potential takes its unscreened form: $V_C(k) \propto \frac{1}{k}$. This leaves the potential energy in the pseudospin basis as

$$V = \begin{bmatrix} 0 & V_k \\ V_k & 0 \end{bmatrix} \tag{2.1}$$

$$V_k = J * k^2 * \frac{1}{k} = J\frac{k}{K} \tag{2.2}$$

Where K is the momentum associated with the K points, and J is the energy scaling factor, calculated to be approximately 1 eV.

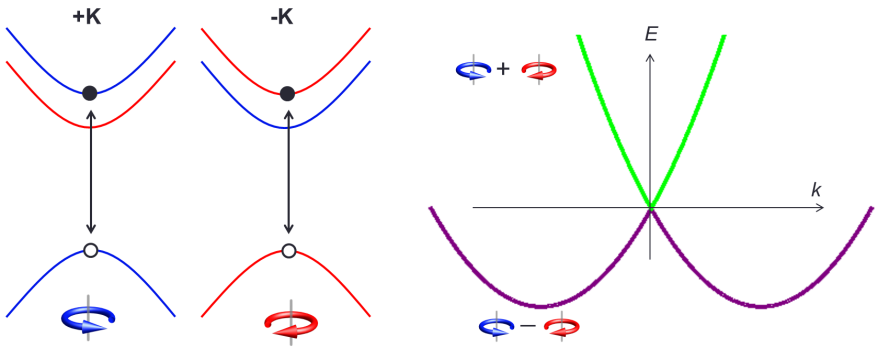

Figure 2.8: Left: excitons in both valleys using exciton basis. Right:exciton dispersion with the valley-orbit interaction Hamiltonian. The eigenstates of the Hamiltonian for the upper and lower branch of the dispersion are denoted by their color: blue and red for $|\sigma^+\rangle$ and $|\sigma^-\rangle$, and purple and green for their linear superpositions.

The eigenstates of the Hamiltonian with potential matrix given by Eq. 2.1 are no longer the individual pseudospins, but rather a linear combination of the two: $|\psi_{\pm}\rangle \propto |\sigma^{+}\rangle \pm |\sigma^{-}\rangle$. Fig 2.8, in the right panel, plots the eigenvalues of this new valley-orbit coupled exciton Hamiltonian as a function of the exciton momentum, $\mathbf{k}$, where the color of the upper and lower branch represents its eigenstate– being a superposition of $|\sigma^{+}\rangle$ (blue) and $|\sigma^{-}\rangle$ (red).

This model has many interesting features in its own right, particularly the implied degeneracy of the two pseudospins and the linear exciton dispersion for small momentum. In Chapter 4, this exciton Hamiltonian will be expanded upon to include the valley Zeeman effect to help explain some of the exciton physics in a magnetic field.

2.3 Berry Curvature and Valley Physics

The breaking of the crystal inversion symmetry in TMDs, along with strong spin-orbit coupling, leads to some very profound consequences to the valley pseudospin, namely the two valleys become distinguishable [99, 93, 92]. While the two valleys are degenerate, inversion symmetry allows for pseudovectors, such as the Berry curvature and orbital magnetic moment, to be nonzero with opposite sign in opposite valleys[92, 95]. For instance, the Berry curvature of MoS_2 is calculated under the three band model[38] in Fig 2.9. The first Brillouin zone is highlight with the dark black line. The Berry curvature reaches a maximum value around the K points, where it is equal, but with opposite sign, between the two valleys. This Berry curvature leads to the valley Hall effect recently observed [41].

Similarly the orbital magnetic moment of electrons at the K points is found to be nonzero, with opposite signs in opposite valleys. Using the simple Dirac fermion model for the electrons at the K points, this "valley magnetic moment" can be shown[95] to take the form $\mathbf{m} = -\hat{\mathbf{z}}\tau_z\mu_B^*$ where $\mu_B^* = e\hbar/2m^*$ is the Bohr magneton with the reduced electron mass and we define $\tau_z = \pm 1$ as the valley index for the $\pm$K valley. The ramifications of this effect are explored more in Chapter 4.

As mentioned in Section 2.1, the valence bands in TMDs are primarily composed of the $d_{xy} + d_{x^2-y^2}$ atomic orbitals with magnetic quantum number $|m_{AO}| = 2$. The inversion symmetry dictates that this, too, must have opposite sign between the two valleys: $m_{AO} = 2\tau_z$. Therefore, the magnetic moment associated with this angular momentum of the valence

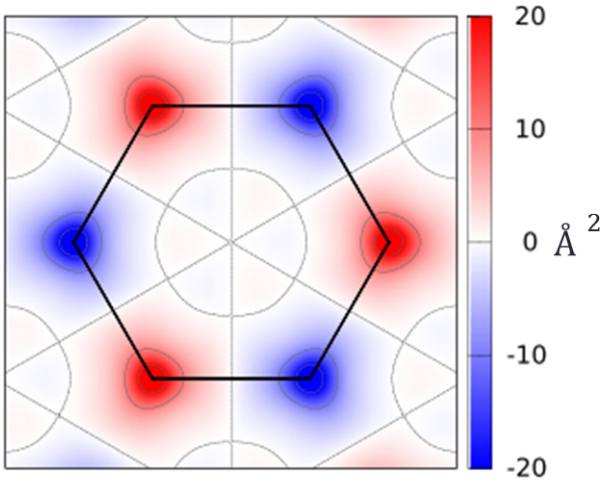

Figure 2.9: Map of the Berry Curvature in the first Brillouin zone for MoS_2. Image taken from Ref [38]

band due to the parent atomic orbitals is also valley selective.

This last valley asymmetry also has a very interesting consequence on optical absorption in TMDs. The conduction and valence bands at the K points have magnetic quantum number $m_{AO,C} = 0$ and $m_{AO,V} = 2\tau_z$, respectively. The selection rules for optical dipole transitions dictate that $\Delta m = \pm 1, 0$, modulo the degree of rotational symmetry (which in the case of hexagonal TMDs is 3). Therefore, only the $\Delta m = +1$ transition, or σ^+ circularly polarized optical excitation, is allowed in the +K valley, and similarly $\Delta m = -1$ (σ^- polarization) in the -K valley. So optical excitation with circular polarization of one handedness will result in excitation of electron/hole pairs in only one valley [92]. Using this valley selective circular dichroism a valley polarization can be created.

2.4 Valley Selective Circular Dichroism

Experimentally the creation of a valley polarization using circularly polarized excitation has been demonstrated using polarization resolved PL in MoS_2 [7, 101, 44, 90] and WSe_2 [28]. In this experiment a circularly polarized laser is used to excited electron/hole pairs in one

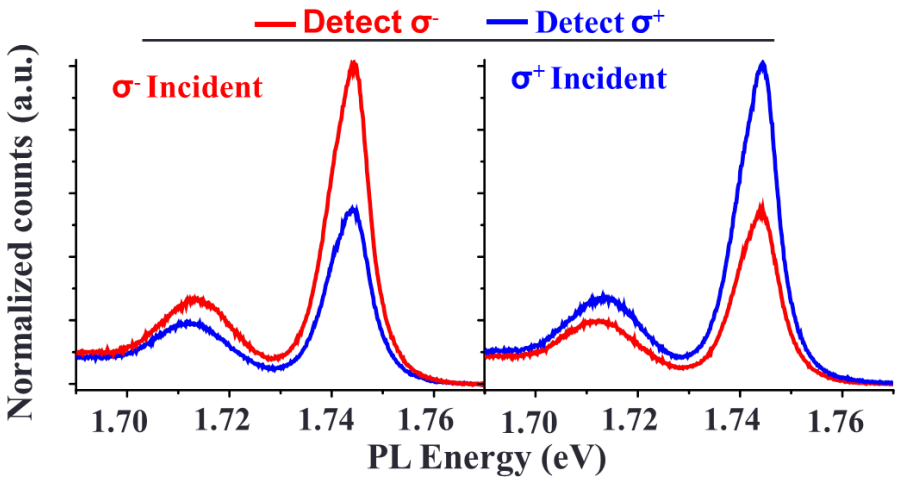

Figure 2.10: Circular polarization resolved PL of WSe_2 . Saturation of cross polarized detected peak is indicative of valley polarization.

valley. These optically excited particles will preferentially form excitons in the same valley, since the large momentum difference between the K points makes them robust to scattering. The emitted PL spectra for both circular polarizations are then detected. Stronger emission is observed in the co-polarized spectra than the cross polarized spectra (see Fig 2.10), indicating that, indeed, the photo-excited carriers preferentially formed excitons in the valley they were excited in creating a valley polarization. The valley polarization is defined as $\rho_{\sigma^+} = \Big(PL(\sigma^+) - PL(\sigma^-)\Big) / \Big(PL(\sigma^+) + PL(\sigma^-)\Big)$, and has values for the exciton typically around 0.3-0.4 for WSe_2 , but have been reported at nearly 1 [89]. Both species of trions also display valley polarization under circularly polarized excitation as shown in Fig 2.10.

Using circularly polarized light to create a valley polarization is an important first step towards creating a valleytronic system. To use the valley pseudospin as a qubit, though, one must be able to create a coherent superposition of the pseudospin states. Linearly polarized light, being a superposition of σ^+ and σ^- light, has been shown to excite a linearly superposition of valley pseudospin[28], as shown in Fig 2.11. Vertically polarized light is incident on the sample and the detected PL spectra for the exciton shows a saturation of the

cross-polarized signal compared to the co-polarized one, again indicating that the excited quantum state is more populated than the orthogonal one. This is a demonstration of the creation of a coherent superposition of valley pseudospin. Notice, however, that the trion peak shows no polarization dependence. This is due to the fact that when the trion emits a photon it leaves behind an extra particle. The state of this particle for a $|\sigma^+\rangle$ trion and a $|\sigma^+\rangle$ trion are orthogonal, therefore destroying the coherence of the emitted photon. A more detailed discussion of this is available in Ref [28].

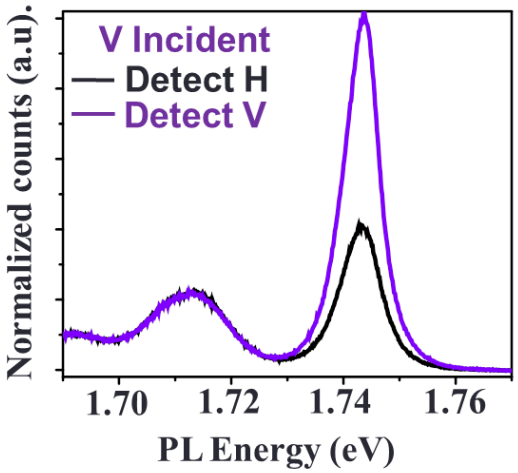

Figure 2.11: Linear polarization resolved PL of WSe_2 . Saturation of cross polarized detected peak is indicative of valley coherence.

Chapter 3

ULTRAFAST DYNAMICS OF EXCITONS IN MONOLAYER WSe_2

As discussed in Chapter 2 the optical properties of monolayer WSe_2 are dominated by its bright excitons. Using PL and linear absorption spectroscopies many interesting properties have been explored [95], particularly the gate tunability of trion species and the valley pseudospin. More recently many ultrafast optical experiments have been performed to investigate the exciton lifetime [13, 67, 40], exciton/trion coupling [68], and valley scattering dynamics [33, 85, 86, 87]. In this chapter nonlinear, ultrafast pump probe techniques will be used to investigate the interactions between excitons and other particles during their brief lifetimes.

3.1 Ultrafast Resonant Pump Probe Spectroscopy

Ultrafast resonant pump probe spectroscopy is used to measure the dynamics of exciton interactions. A schematic view of the optical setup is shown in Fig 3.1.

This process starts with an ultrafast pulsed laser: Coherent MIRA Ti:Sapphire laser pumped with a 10W Verdi. The pulses are approximately 200 fs wide with a repetition rate of 76 MHz. A beamsplitter is used to separate the pulse train into two nearly identical pathways, creating degenerate pump and probe beams. The probe beam traverses a fixed path length, while the pump beam's path is variable using a mechanical delay stage. When the two beams are recombined using another beamsplitter there will be a variable time delay, τ, between the pulses from each beam depending on the position of the delay stage. Data is taken with a fixed delay between the pulses. The pump pulse comes in and excites the exciton population, which then is free to interact and decay. After the delay time τ has passed the probe pulse comes in and measure the dielectric constant of the sample, which carries information about the exciton population and energy. The temporal delay can range from tens of fs to ns with a meter long delay stage, making this technique capable

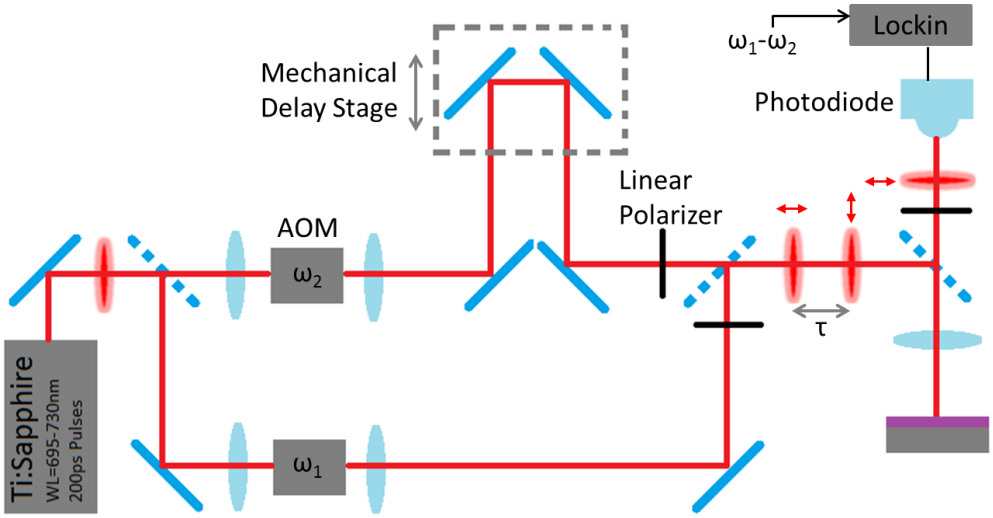

Figure 3.1: Schematic of the optical setup for ultrafast resonant pump probe spectroscopy.

of measuring timescales much shorter than detectable with even the fastest electronics using basic DC techniques.

In this experiment the laser frequency (of both the pump and the probe) is swept across the resonance of the WSe_2 exciton and the intensity of the probe pulse after it is reflected off of the sample is measured on an amplified photodiode to determine the dielectric constant of the sample under those excitation conditions. The pump and probe beams are cross linearly polarized using linear polarizers placed right before the recombining beamsplitter. This reduces optical interference between the two beams when $\tau = 0$, and allows the pump beam to be filtered out with another linear polarizer placed in the reflected beampath before the photodiode. Both beams are individually modulated with an acousto-optical modulator (AOM) at frequencies around 100 KHz. The signal from the photodiode is then fed into a lockin amplifier detecting at the difference frequency of the two beam's modulations (~30 KHz). In this way the measured signal is only due to nonlinear (third order) effects in the dielectric constant. The basic properties of the excitons are ignored in favor of the nonlinear interaction effects.

3.2 Ultrafast Data from Excitons in WSe_2

A WSe_2 sample is exfoliated onto a substrate of 300 nm of SiO_2 on Si using the "scotch tape method". This sample is then mounted into a chip carrier in a closed cycle, liquid helium cryostat, cooled down to a temperature of 20K and a pressure of several tens of micro-torr. The pump and probe beams are colinearly incident onto a high numerical aperture, long working distance, 40x microscope objective which focuses both beams to coincident spots, with radii of 1-2 μm, onto the sample. The reflected signal passes through a 50/50 beamsplitter, a linear polarizer to remove the pump beam, and then is focused onto an amplified photodiode. The differential reflectivity signal, dR, is recorded in one lockin amplifier at the frequency $\omega_1 - \omega_2$, while the total reflectivity of the probe beam, R, used to normalize the reflected signal, is detected from another lockin amplifier at only the probe modulation frequency, ω_1.

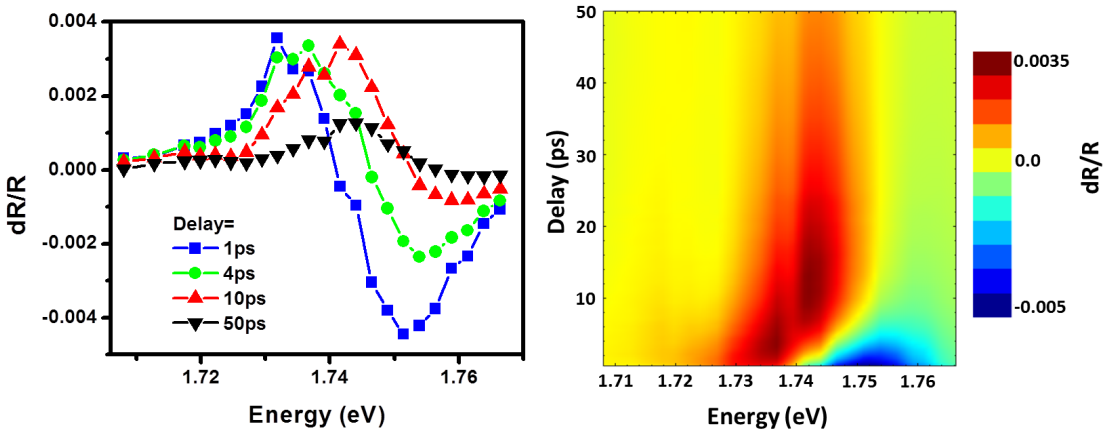

Figure 3.2: Differential reflectivity signal versus the optical excitation energy and the pump-probe time delay. On the left are line cuts of the exciton resonance for constant time delay, on the right is the full 2D map.

The laser excitation wavelength is swept across the exciton resonance while the pump probe time delay is also swept. In this was a 2-dimensional map of the exciton resonance

as a function of time is mapped out. This is shown in Fig 3.2, for an incident laser power of 10 μW for both the pump and the probe beams.

There are several readily identifiable features present in the data. This first is the change from a relatively plus/minus symmetric, dispersive signal at low time delay, to a solely positive peak at longer time scales. The second is a general blue shift in the resonance with increasing time delay. To explain these features a theory must be developed to describe the exciton lifetimes and interactions in WSe_2 and how they related to the overall changed in the measurable dielectric constant. An initial theory and its applicability to the data is explored in the next section.

3.3 Model of Nonlinear Exciton Interactions

To develop a theoretical model to describe the dielectric constant of WSe_2 , a Hamiltonian for the exciton must be written down which includes the interaction effects of not only the exciton with the optical fields, but also other excitons and free carriers. While, in this experiment, the optical fields are resonant with the exciton, and therefore too far below the band edge to excite free carriers directly, higher order Auger processes can create free electron/hole pairs through nonradiant exciton annihilation [80, 84, 88]. This Hamiltonian is shown in Eq 3.1 below, where B and $B^\dagger$ are the lowering and raising operators which destroy or create a $\mathbf{k} = 0$ exciton.

$$H = E_X B^\dagger B + uB^\dagger B^\dagger BB + (1 - N_0)(\Omega(t)B^\dagger + h.c.) - f(\Omega(t)B^\dagger B^\dagger B + h.c.) \qquad (3.1)$$

The first term in the Hamiltonian is the single exciton energy, E_X; the second term describes exciton/exciton interactions, parameterized by u; the third term is the exciton/laser interaction, where $\Omega(t)$ is the laser Rabi frequency and $(1 - N_0)$ accounts for the phase space filling of the excited free carriers, N_0; and the last term accounts for higher-order exciton/photon interactions due to the phase space filling from other excitons, parameterized by f. From Ref [78] $u \sim 6E_b a_B^2/A$ and $f \sim \frac{4}{7}\pi a_B^2/A$, with E_b the exciton binding energy, a_B the exciton Bohr radius, and A the illuminated area.

Let $P \equiv \langle B \rangle$ and $n \equiv \langle B^\dagger B \rangle$ be the optical polarization and the exciton population [61], respectively, then the Heisenberg equation of motion for the polarization can be found to be the following:

$$i\frac{d}{dt}P = E_X P + 2unP + (1 - N_0 - 2fn)\Omega(t) \tag{3.2}$$

The exciton number excited by the pump laser, n, is assumed to be known and slowly varying over the duration of the pump pulse.

Assuming a harmonic dependence to P and Ω, *i.e.* $P(t) \equiv \delta P(\omega)e^{-i\omega t}$ and $\Omega(t) \equiv \delta\Omega(\omega)e^{-i\omega t}$, then the total optical susceptibility can be given by

$$\chi_T(\omega) \equiv \frac{\delta P(\omega)}{\delta\Omega(\omega)} = \frac{1 - N_0 - 2fn}{\omega - E_X - 2un + i\gamma} \tag{3.3}$$

Define $x \equiv \pi a_B^2 n/A = \rho_{ex}\pi a_B^2$ as the exciton density induced by the pump pulse, then $2fn \approx x$. The exciton/exciton Coulomb interaction strength is given by the parameter $\kappa \equiv un/x \sim 2E_b \approx 1eV$.

The linear susceptibility can be expressed as

$$\chi_L(\omega) = \frac{1}{\omega - E_{X0} + i\gamma_0} \tag{3.4}$$

where E_{X0} and γ_0 are the equilibrium exciton energy and resonance width, respectively.

To find the nonlinear susceptibility, which is the quantity measured in Section 3.2, the linear susceptibility in Eq 3.4 can be subtracted from the total susceptibility in Eq 3.3 to give

$$\chi_{NL}(\omega,t) \equiv \chi_T(\omega,t) - \chi_L(\omega) = \frac{1 - N_0(\omega,t) - 2x(\omega,t)}{\omega - E_X(N_0) - 2\kappa x(\omega,t) + i\gamma} - \frac{1}{\omega - E_{X0} + i\gamma_0} \tag{3.5}$$

where the population variables x and N_0 are functions not only of time, but also of the laser excitation frequency, ω. Both populations are excited by the pump pulse and therefore will decay with their own time dependence. Additionally, one would expect that the initial populations would depend on were they pump frequency lies within the exciton resonance: $x(\omega,t) \propto \frac{\gamma}{(\omega - E_{X0})^2 + \gamma^2}$ and similarly for N_0.

The dependence on N_0 is twofold. First is the phase space filling effect explicitly denoted in the numerator of Eq 3.5. Secondly is a band gap renormalization effect where excess free carriers narrows the exciton energy [30], implicitly denoted $E_X(N_0)$. By defining $\Delta E_X(N_0) \equiv E_X(N_0) - E_{X0}$ as the change in the exciton resonance from its equilibrium energy, the excitation energy dependence can also be extracted $\Delta E_X(N_0) = \frac{\gamma}{(\omega - E_{X0})^2 + \gamma^2} \Delta E_X(\omega)$. Coulomb screening by these free carriers should be a negligible effect since, as a 2D material, most of the electric field lines from the carriers in WSe_2 are out of the plane of the sample where there are no charges to screen the field.

Combining all of these results into Eq 3.5 gives a final equation for the nonlinear susceptibility where all frequency dependence is explicitly stated, and the time dependence is located completely within the population variables.

$$\chi_{NL}(\omega, t) = \frac{1 - \frac{\gamma}{(\omega - E_{X0})^2 + \gamma^2}\Big(N_0(t) + 2x(t)\Big)}{\omega - E_{X0} - \frac{\gamma}{(\omega - E_{X0})^2 + \gamma^2}\Big(\Delta E_X(t) + 2\kappa x(t)\Big) + i\gamma} - \frac{1}{\omega - E_{X0} + i\gamma_0} \tag{3.6}$$

This equation can now be used to fit the data presented in Fig 3.2 for constant time delay. Eq 3.6 has five fitting parameters: an overall scaling factor A, such that $dR/R = A * \chi_{NL}$; the equilibrium exciton energy, E_{X0}; the resonance width, γ; the unitless term in the numerator, $N(t) \equiv N_0(t) + 2x(t)$; and the energy shift term in the denominator (in eV), $d(t) \equiv \Delta E_X(t) + 2\kappa x(t)$. The first two terms here are sample dependent only; while the third term is not dependent on the time delay, but is dependent on the pump power as we shall see in Section 3.5. It is only the last two terms, $N(t)$ and $d(t)$, that are time dependent. So for a complete 2-D scan, like in the right panel of Fig 3.2, A, E_{X0}, and γ are global parameters, while $N(t)$ and $d(t)$ will be individually fit for each line of constant time delay. The time dependence of both of these parameters will fall out of the fits.

Physically, $N(t)$ describes either the filling of phase space, from either free carriers or other excitons, or the transfer of optical oscillator strength of the exciton to trion species in the presence of the optically excited free carriers—both of which limit further excitation of excitons in the sample. The other term, $d(t)$, describes a shift in the resonance energy of the exciton either due to the renormalization of the single particle band gap due to the presence

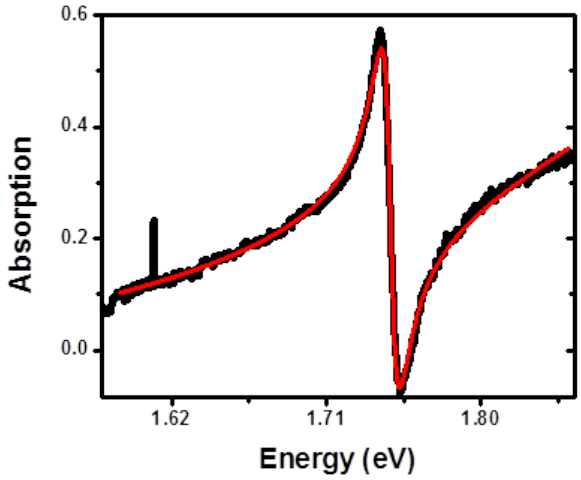

Figure 3.3: White light linear absorption of WSe_2 fit with Eq 3.4 to extract out the equilibrium exciton energy and the optical system scaling factor.

of optically excited free carriers or from the Coulomb repulsion between excitons. Both of these terms describe the interaction of optically excited excitons with other particles, and their ultrafast time dependences is of fundamental interest.

The A and E_{X0} parameters can be nailed down by separately measuring the linear absorption with white light reflectivity (see Ref [63] for details). By taking the difference in the light reflected from a white light source illuminating the sample from that just illuminating the substrate, a spectra of the band edge and exciton absorptions can be found as shown in Fig 3.3. This spectra is fit with the linear susceptibility (Eq 3.4), added to a linear offset to account for the tail of the band edge absorption. From this the parameters are found to be $A = 0.0034$ and $E_{X0} = 1.747$ eV. The width turns out to be power dependent, and so the value of γ used to fit the ultrafast differential reflectivity data cannot be determined from the linear reflectivity measurement.

Armed with these fixed parameters, the rest of the 2D data can be fit, line by line, by varying $N(t)$ and $d(t)$ and a global best fit of γ. Therefore, all the variation present within Fig 3.2 can be expressed with only two fitting parameters. With this in mind, Equation 3.6

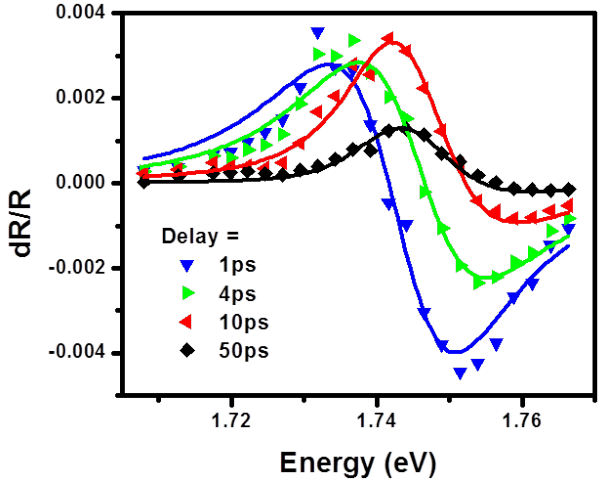

Figure 3.4: Fit of Eq 3.6 to constant time line cuts of the exciton resonance.

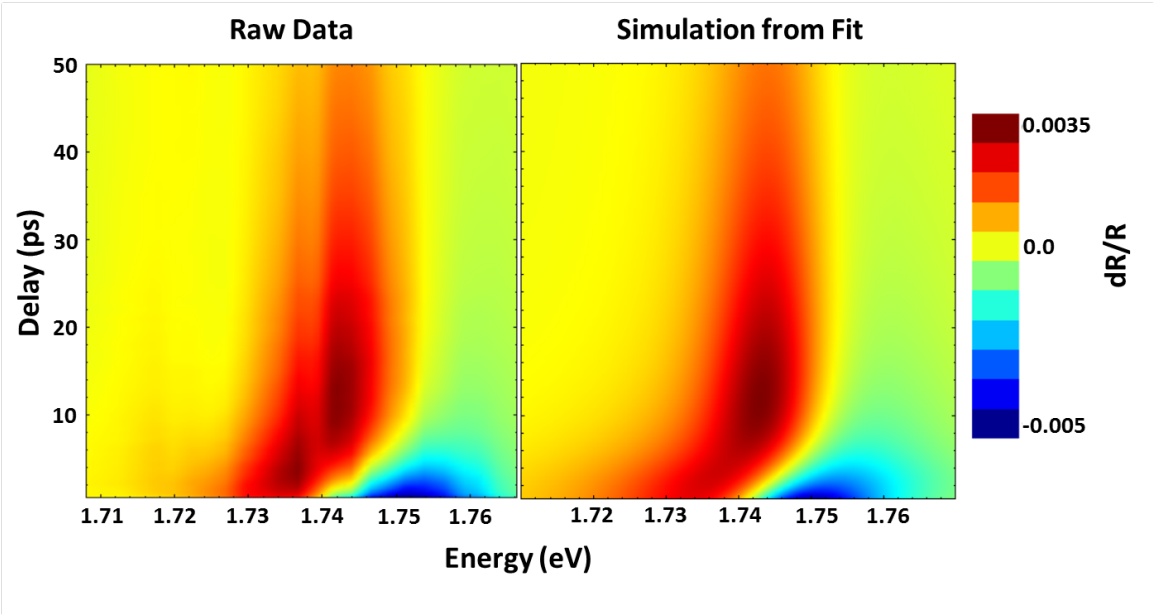

Figure 3.5: Differential reflectivity signal versus the optical excitation energy and the pump-probe time delay. On the left is the raw data, on the right is the interpolated 2D map from the fit resonance curves.

fits the data remarkably well, as shown in Fig 3.4. Indeed, by plotting the fitted curves in 2D along side the raw data in Fig 3.5 the agreement is striking.

3.4 Time Dependence of Exciton Interactions

Based on the agreement of the fit to the data alone, the theory presented in Section 3.3 seems to be a remarkable success. The next step is to extract out the time dependence of the $N(t)$ and $d(t)$ parameters and see if physical sense can be made — particularly if nonlinear interaction effects can be observed.

Remember the two time dependent fitting parameters are actually the sum of two individual terms: $N(t) = N_0(t) + 2x(t)$ from the phase space filling and oscillator strength transfer (OST), and $d(t) = \Delta E_X(t) + 2\kappa x(t)$ describing the resonance shift. While the population variables N_0 and x are strictly positive, as well as κ, ΔE_X should be entirely negative since the free carriers result in a band gap narrowing upon renormalization [30]. From this analysis, one would expect $N(t)$ to be composed of two positively decaying exponentials, while $d(t)$ should have a positive and negative one. Extracting out the best fit values of these parameters as a function of the time delay confirms this fact (Fig 3.6).

In both cases there exists a fast component which can be attributed to the exciton population effects ($x(t)$ and $2\kappa x(t)$), with lifetimes around 10 ps comparable with those reported elsewhere [13, 67, 40], and a slow component that can be attributed to the free carrier effects (N_0 and $\Delta E_X(t)$), that has a lifetime of several tens of ps. Importantly both fit constants approach zero at large time delay as the system tends towards its equilibrium value.

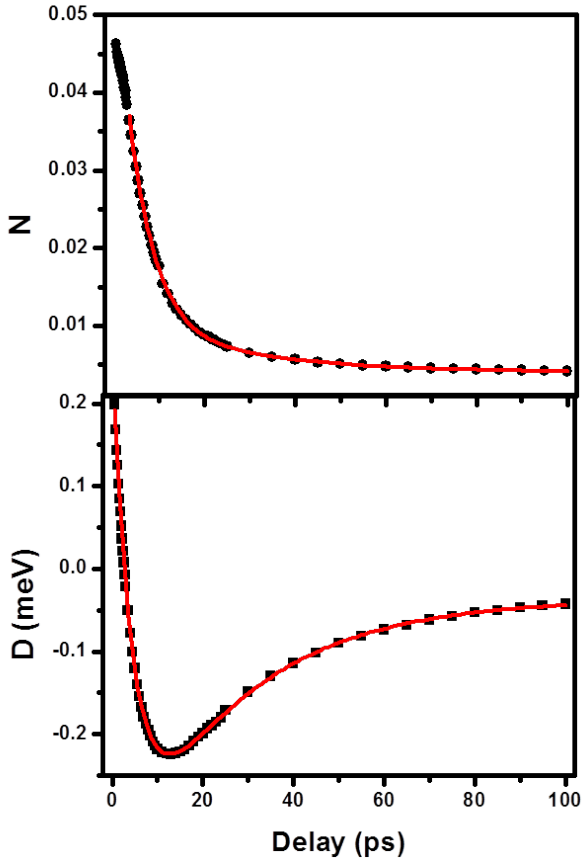

Figure 3.6: Extracted time dependence of fit parameters from Eq 3.6. On the top is the phase-space filling factor, on the bottom is the resonance energy shift (in meV). The red curves are double exponential fits to the data.

3.5 Power Dependence of Exciton Interactions

To really determine the nonlinear nature of these interactions the effect on the time dependence is monitored as a function of the pump power, which modulates the excited carrier populations. For each power a full 2D map, similar to Figure 3.2, is created. Again the scaling factor, A, and the equilibrium resonance energy, E_{X0}, are independent of the pump power. However the resonance width, γ, and the time dependent parameters, $N(t)$ and $d(t)$, will be a function of the excited carrier populations. The time dependence of the two fit parameters are extracted as a function of the pump power, as shown in Figure 3.7. Qualitatively all the curve show similar features as a function of the incident pump power, though the effects obviously become larger with increasing power.

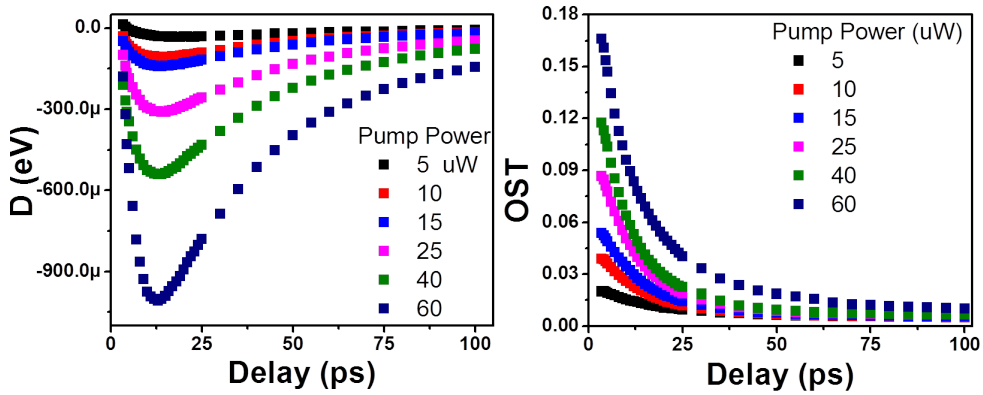

Figure 3.7: Temporal evolution of the fit parameters $d(t)$ and $N(t)$ describing the resonance peak shift (left) and the oscillator strength transfer (OST, right) as a function of the incident pump power.

Each curve can be fit nicely to a double exponential, similar to Figure 3.6, where fit constants are described by the following equations

$$d(t) = D1e^{-t/R1} + D2e^{-t/R2} \tag{3.7}$$

$$N(t) = N1e^{-t/T1} + N2e^{-t/T2} \tag{3.8}$$

The power dependence of these eight fit parameters are extracted and shown in Figure 3.8, with the parameters for the resonance peak shift, $d(t)$, shown on the left and the oscillator strength transfer, $N(t)$, shown on the right. The red data points are those attributed to the free carrier population dependent terms ($N_0(t)$ and $\Delta E_X(t)$) and the black data points from the exciton population dependent terms ($x(t)$ and $2\kappa x(t)$).

The free population variables, $N_0(t)$ and $x(t)$, are both present in the OST fit on the right. The power dependence of their populations makes rough sense. At low pump powers the exciton population, depicted as N1, grows linearly while the free carrier population, N2, is approximately zero. It is only at high pump powers that the excitation population saturates and the free carrier population begins to rise. Here the exciton population has become large enough that the Auger process rates begin to become appreciable and excitons are destroyed in favor or promoting electron/hole pairs to the band edge. Some modeling needs to be done to verify that these relative populations make sense, but qualitatively the process seems reasonable.

The exponential lifetimes of these populations generally show faster decay rates with increasing pump power, and with the free carrier lifetime much longer than the exciton one. The fact that the lifetimes decrease with power hints at interaction effects: large populations promote faster recombination. Again, the decay times of the exciton population, T1, of $\sim$10 ps is consistent with other measurements [13, 67, 40], which is a reassuring test of the theory.

The terms that make up the $d(t)$ fitting parameter are functions of the exciton and free carrier populations. The D1 parameter is describing the power dependent amplitude of $2\kappa x(t)$, and the fact that it behaves differently than the bare $x(t)$ from N1 implies a power dependence of κ. This is reasonable, as κ denotes the exciton-exciton Coulomb interaction, at some large population the effect surely behaves nonlinear. In this case D1 is linear while N1 is, but then goes superlinear, implying that the Coulomb interaction becomes increasingly strong as the excitons become more and more densely packed. D2 describes the band gap normalization,$\Delta E_X(t)$, due to the presence of free carriers. When the free carrier density becomes strong, behaving superlinear with pump power at higher powers, so too does the D2 term. Careful analysis of the relationship between these two power dependences may shed light on the functional form of $\Delta E_X(N_0(t))$ and the mechanisms of

band gap renormalization.

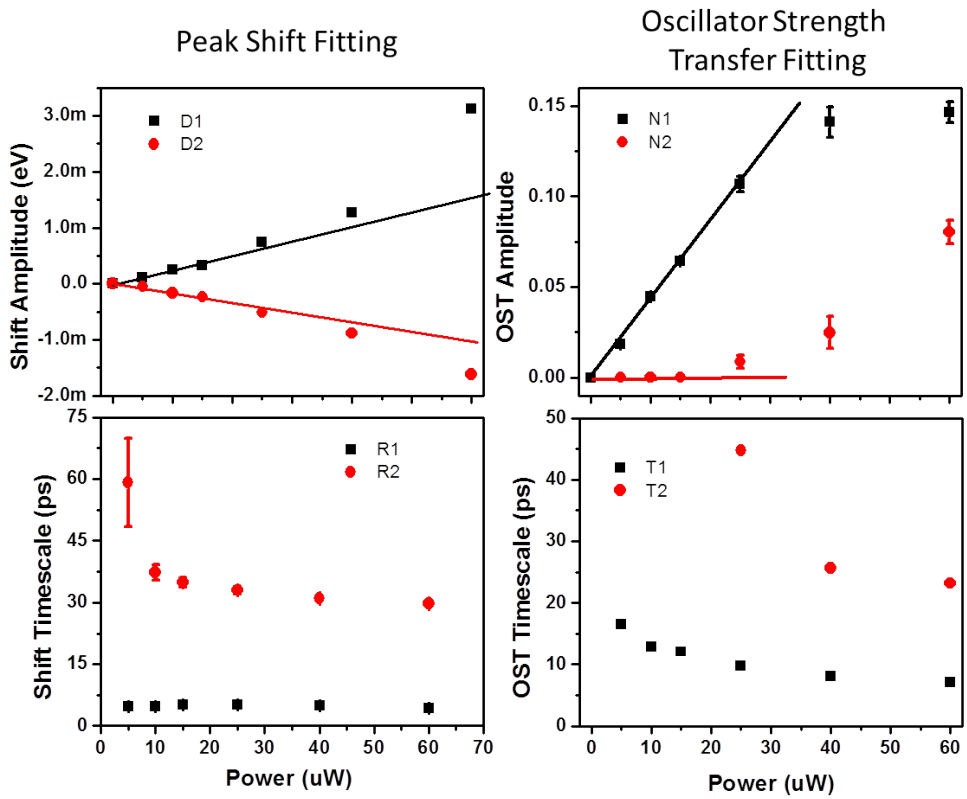

Figure 3.8: Power dependence of the fit parameters to the temporal evolution of the resonance peak shift (left) and the oscillator strength transfer (OST, right). The definition of the fit parameters are given in equations 3.7 and 3.8. The top plots show the amplitude of the fitted exponentials and the lower plots show the exponential decay time.

Finally the extracted resonance width is plotted as a function of the incident pump power in Figure 3.9. The width increases rather dramatically, and follows a roughly linear dependence on the pump power. The precise mechanism for this is not yet known, but it could arise from excitation induced dephasing [66]. Here the larger populations of excitons lead to more collisions, creating dephasing between the coherent pump probe signals and a general increase in an optical resonance width.

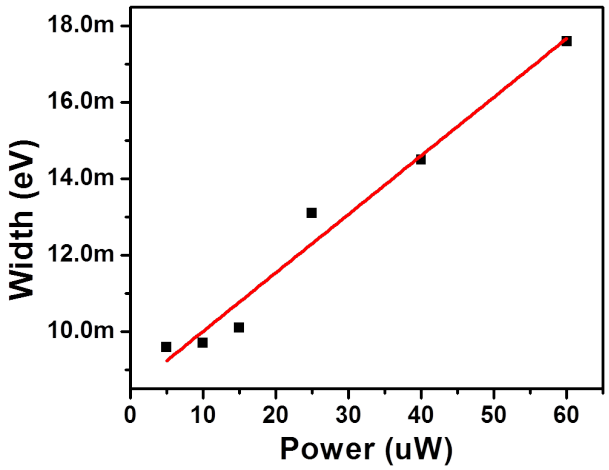

Figure 3.9: Broadening of the exciton resonance width as a function of the incident pump power. Width is extracted as a best global fit to each line individually in a 2D map like shown in Figure 3.2.

3.6 Outlook and Future Work

Nonlinear effects are large in WSe_2 . The confinement into 2D leads to greater wavefunction overlap between particles, and the planar nature leaves electric fields unscreened out of the plane. The aim of this work has been to try to investigate the ultrafast interactions between photoexcited carriers that stems from these nonlinear effects.

A concise theory has been developed to explain the data in terms of fundamental photoexcited carrier populations. From this theory the time and power dependence of these populations have been extracted and they show an inherently nonlinear dependence on the pump power. However, the precise mechanism leading to these nonlinear interactions has yet to be worked out. Further investigations into the cause of these effect is in order to fully understand the effect interactions play on the excitonic properties like their lifetime and scattering. Finally, the theory made several assumptions that have yet to be experimentally proved, most notably the presence of free carriers. Since the excitation is below the band gap, there can be no direct excitation of free carriers in this system; however, nonlinear

Auger processes can promote one photoexcited electron/hole pair to the free carrier continuum via the non-radiative decay of another pair. This process has been the focus of many other investigations [80, 84, 88], but has not been shown to be definitively occurring here.

A major limitation in this work was the use of a, relatively, large probe power so that the signal could be detected with high signal-to-noise. However, when the probe field is too large it creates a significant population of carriers of its own that will in turn effect its reflectivity. These kinds of effects can lead to extra nonlinearities that can be difficult to explain, and have been ignored in the theory developed here. Traditionally the probe beam should be an order of magnitude weaker than the probe to limit these effects. This may be possible in this experiment by replacing the amplified photodiode detector with a high gain avalanche photodiode. However, greater care must be taken in removing the pump beam so small leakage does not overpower the probe.

Additionally the experimental ease of doing this as a *degenerate* pump probe spectroscopy has some complications. It required the theory to assume a particular frequency dependence to the photo-excited populations to account for the fact that the pump was sweeping across the absorption resonance. A non-degenerate experiment, with the pump fixed in the center of the resonance, would provide for a simpler and more easily interpreted theory.

Chapter 4

MAGNETIC CONTROL OF VALLEY PHYSICS IN MONOLAYER WSe_2

As was discussed in Section 2.3, due to inversion symmetry breaking in WSe_2 the orbital magnetic moments of low energy electrons at the K points is nonzero, with opposite signs in opposite valleys. Additionally, the atomic orbitals that make up the valence band structure also have a nonzero magnetic moment that switches signs between the two valleys. In this chapter, an external magnetic field is coupled to these magnetic moments and used to break the valley degeneracy. The magnetic field is shown to be an external control of many of the valley phenomena which is an important step for valleytronic applications of WSe_2 . The next section describes the experimental techniques. Section 4.2 will demonstrate the breaking of the valley degeneracy through the valley Zeeman effect. Its consequences on the valley polarization and valley coherence, as well as the gate dependence of these phenomena, will then be discussed in the following sections. Much is this work is published in Ref [1], with similar findings in Refs [37, 39, 73] in both WSe_2 and $MoSe_2$.

4.1 Magneto- Photoluminescence

To measure the valley pseudospin properties such as the exciton energy and valley polarization, a polarization resolved micro- photoluminescence (PL) spectroscopy is used as outlined in Figure 4.1. The sample is cooled under vacuum to a temperature of around 10 K inside a superconducting magnet capable of applying bipolar fields of up to 7 T perpendicular to the plane of the sample (Faraday geometry).

PL spectroscopy is performed by optical excitation of carriers in a material with a (relatively) high energy laser. These carriers non-radiatively relax down to the band edge, defect sites, or exciton states. From there they may finally recombine and emit light, below the energy of the incident laser radiation, with an optical energy describing the energy of their final state. The resulting spectrum describes the available (semi-) long lived states,

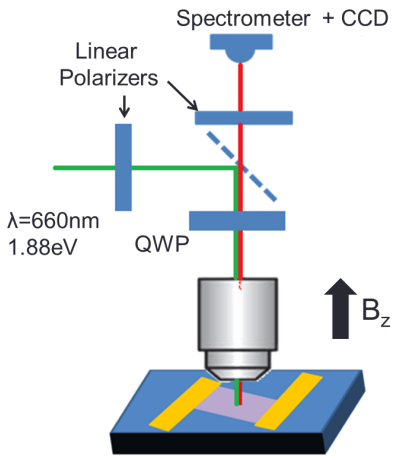

Figure 4.1: Schematic of the magneto- photoluminescence setup.

their energies, and relative populations.

In this experiment the incident laser has an energy of 1.88 eV (λ=660 nm), denoted by the green line in Fig 4.1, which is smaller than the band gap energy ($\sim$2 eV) but greater than the exciton energy ($\sim$1.74 eV) of WSe_2 . Therefore, the laser excites virtual electrons and holes which then bind to form real excitons. The polarization of the incident laser is set with a high extinction ratio linear polarizer. The beam is then reflected off of a dichroic mirror, passes through a quarter wave plate (QWP) before being focused to a $\sim$2 μm spot size on the sample with an aspheric lens. By selecting either "H" or "V" polarized light with the linear polarizer, the QWP turns the polarization at the sample into σ^+ or σ^-. The emitted PL (red line in Fig 4.1) is collected by the same lens, passes through the QWP (which turns it back into a linear polarization), passes through the dichroic mirror, and through another high extinction ratio linear polarizer. This polarizer is used to select the helicity of the emitted radiation. This light is then filtered with a high pass filter (to remove the residual laser light) and is spectrally resolved onto a liquid nitrogen cooled CCD through a spectrometer. By varying the two linear polarizers between "H" and "V" the different valley pseudospin configurations can be measured: $\sigma^+_{excite}/\sigma^+_{detect}$, $\sigma^+_{excite}/\sigma^-_{detect}$, and the similar terms for σ^- excitation. These four spectra are measured as a function of

the applied, out of plane magnetic field to investigate the magnetic properties of the valley pseudospin.

4.2 Valley Zeeman Splitting

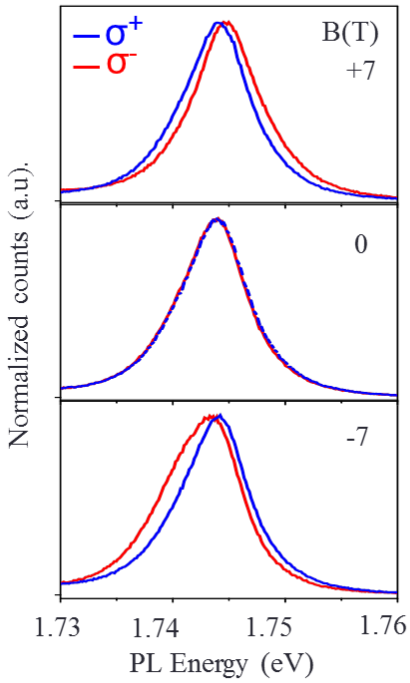

Figure 4.2: Spectra of σ^+ (blue) and σ^- (red) polarized exciton PL for an applied magnetic field of +7 T (top), 0 T (middle), and -7 T (bottom). Under an applied field the two spectra split due to the valley Zeeman effect.

In Figure 4.2 the normalized PL spectra of the neutral exciton for both valley pseudospin are plotted for select values of the applied magnetic field. With out the field (middle) the two curves lie directly on top of each other as would be expected from time reversal symmetry. As a positive field is turned on (top) the two spectra shift, with the σ^- polarized peak appearing at higher energy than the σ^+ polarized peak. The opposite is true with

a negative field (bottom). This is the first observation of a valley Zeeman effect, and by measuring the splitting as a function of field one can calculate the valley magnetic moment.

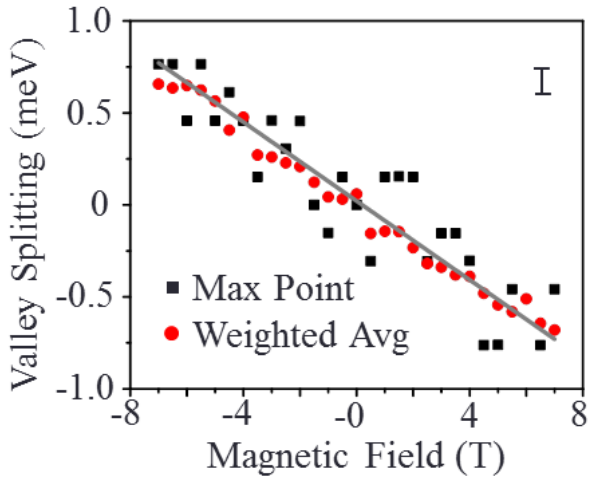

Figure 4.3: Splitting of the exciton resonance ($|\sigma^+\rangle_{peak} - |\sigma^-\rangle_{peak}$) as a function of magnetic field. The splitting is computed using two different techniques as described in the text. The measurement error (from the CCD pixel width) is shown in the top right.

The asymmetry of some of the lineshapes are artifacts due, primarily, to sample inhomogeneity, and make getting a reliable fit to the peaks difficult. To overcome this the peak position is calculated in two different ways in order to quantitatively determine the Zeeman shift. The first, the "Max Point" method, takes the fifteen points in the spectra with the most counts and assigns the peak position to the median point. This method is insensitive to the sample asymmetry and the presence of the trion peak at lower energy, but very sensitive to noise in the spectra since it takes into account only a few points. The second method, the "Weighted Average," computes the center of mass of the peak $\int Ef(E)dE / \int f(E)dE$, where $f(E)$ is the PL spectral density and E is the photon energy. The sensitivity to noise is greatly reduced in this method as it makes use of several hundred points in the computation of the peak, but peak asymmetry or the presence of a strong

trion peak at lower energy can skew the calculated position. Using both methods, the peak splitting of the valley pseudospin ($|\sigma^+\rangle_{peak} - |\sigma^-\rangle_{peak}$) is determined as a function of the applied field, see Figure 4.3. Both methods of calculation agree well with each other, and the splitting can clearly be seen to be linear in the applied field. Fitting the noisier "Max Point" data to a line gives a valley splitting of -0.11 ± 0.01 meV $\mathrm{T}^{-1} = -(1.9 \pm 0.2)\mu_B$.

The observed splitting of the valley pseudospin can be explained by the combination of several magnetic moments in the sample. As discussed in Sec 2.3 the breaking of inversion symmetry in WSe_2 results in a nonzero orbital magnetic moment related to the Berry curvature called the "valley magnetic moment," m_v [95, 99]. Additionally the valence band is composed predominately of the high angular momentum d-orbitals of the tungsten atoms, giving rise to another magnetic moment, m_A. Finally, due to the large spin orbit coupling interaction, the bands are spin split resulting in a spin magnetic moment for each band, denoted m_s. The overall Zeeman shift is due to the sum of these three magnetic moments, leading to an effective g-factor different than the vacuum value of 2.

The low energy band structure of WSe_2 along with the shift of each band due to the three individual magnetic moments is pictorially shown in Figure 4.4 with the optical transitions marked. As mentioned in Sec 2.1, optical transition in TMDs conserve spin. While the spin magnetic moment shifts the individual bands ($\Delta_s = 2s_z\mu_B B$, black arrows), and the shift is opposite for the two valley pseudospins, the shift is the same in the conduction and the valence band resulting in no change to the valley resonance energy. The magnetic moment due to the atomic orbitals does result, however, in a shift in the resonance, since only the valence bands shifts ($\Delta_A = 2\tau_z\mu_B B$, purple arrows). The net shift in the optical resonance is then $-2\tau_z\mu_B B$, where $\tau_z = \pm 1$ is the valley index for the $\pm$K valleys.

The shift due to the valley magnetic moment is $\Delta_v = \alpha_i\tau_z\mu_B B$ (green arrows) where α_i is the valley g-factor for each band $i = c, v$. To leading order the band edge carriers can be described as massive Dirac fermions[92, 95] with $\alpha = (m_o/m^*)$ and the effective mass, m^*, the same for both the conduction and valence bands. Within this approximation there would be no effect from the valley magnetic moment on the optical resonance since all bands in each valley shift identically. However, corrections beyond the Dirac fermion model give different masses and magnetic moments for electrons and holes[32, 38]. This would give rise

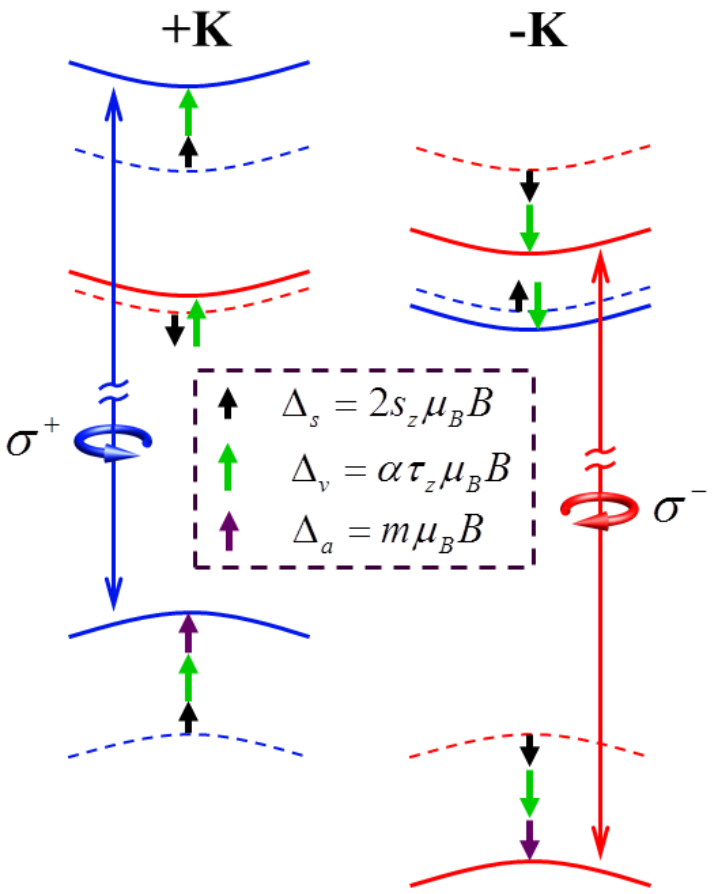

Figure 4.4: Low energy band structure of WSe_2 showing the effect of the different magnetic moments on the bands with an applied positive magnetic field. The arrows represent the shifts due to the spin magnetic moment (black), the valley magnetic moment (green) and the atomic orbital contribution (purple).

to a shift in the optical resonance of $\tau_z\Delta\alpha\mu_B B$, where $\Delta\alpha = \alpha_c - \alpha_v$.

The net effect is a valley dependent linear shift in the exciton resonance of $-\tau_z\Delta(B)/2$, where $\Delta(B) = 2(2-\Delta\alpha)\mu_B B$ is the exciton valley Zeeman splitting. This implies that for $B > 0$ the -K valley exciton (with $\tau_z = -1$) should have higher energy than the +K valley exciton (with $\tau_z = +1$), and vice versa for $B < 0$, as seen in Figure 4.2. The fits to the data

in Fig 4.3 gives $\Delta\alpha = 1.1 \pm 0.1$, implying that the carriers are indeed not Dirac fermions and that the valley magnetic moment is definitely nonzero in WSe_2 . However, it must be noted that there was considerable spread in the measured Zeeman splittings of different samples. This is attributed to the sample doping and will be discussed further in Sec 4.4.

In terms of the valley-orbit coupled exciton theory [100] developed in Section 2.2, the valley Zeeman effect can be modeled as an extra term in the potential energy matrix

$$V = \begin{bmatrix} -\Delta(B)/2 & V_k \\ V_k & \Delta(B)/2 \end{bmatrix} \tag{4.1}$$

With V_k, defined in equation 2.2, describing the coupling between the valley index of the exciton and its momentum k. The effect on the exciton dispersion relation of an applied magnetic field is shown in Figure 4.5. For $B = 0$ the two branches of the dispersion are described by the two different linear superpositions of the valley pseudospin states, and they are degenerate at $k = 0$. When a positive field is turned on (right panel) a gap opens up at $k = 0$ of magnitude $\Delta(B)$, and the individual valley pseudospins become the eigenstates at low momentum, with the upper branch gaining $|\sigma^-\rangle$ flavor (red) and the lower branch gaining $|\sigma^+\rangle$ flavor (blue). The opposite is true for negative field (left panel). This will have important ramifications to the valley polarization as described in the next section.

4.3 Magnetic Dependence of Valley Polarization

The breaking of the valley pseudospin degeneracy with an applied magnetic field enables control of the valley polarization. As described in Sec 2.4 pumping a sample with a circularly polarized laser, $\sigma^\pm$, results in the formation of carriers in the $\pm$K valley. These carriers preferentially form excitons in the valley they are created in, since the large separation of the valleys in K-space suppresses scattering, and thus the light emitted will be preferentially $\sigma^\pm$ polarized. A saturation of a cross-polarized detected peak ($\sigma^\pm_{excite}/\sigma^\mp_{detect}$) compared to the co-polarized detected peak ($\sigma^\pm_{excite}/\sigma^\pm_{detect}$) is indicative of a valley polarization in the $\pm$K valley, respectively. The degree of polarization for excitation with σ^+ is represented as $\rho_{\sigma^+} = \Big(PL_{peak}(\sigma^+) - PL_{peak}(\sigma^-)\Big)/\Big(PL_{peak}(\sigma^+) + PL_{peak}(\sigma^-)\Big)$. The aim of this section is to investigate what effect an applied magnetic field has on $\rho_{\sigma^\pm}$.

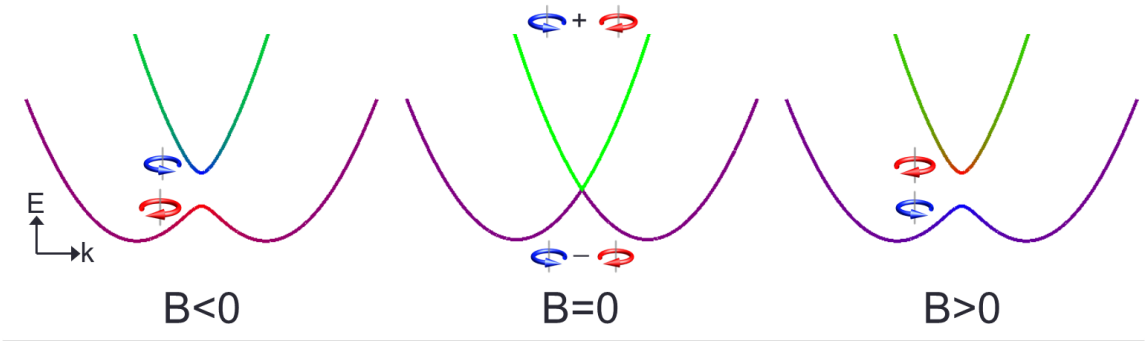

Figure 4.5: Energy spectra of the exciton in the valley-orbit coupled basis for different magnetic fields. For $B = 0$ (center) the case is the same as presented in Fig 2.8. When a positive field is turned on (right) a gap is opened with the energy eigenstate of the upper (lower) band taking on that of $|\sigma^-\rangle$ ($|\sigma^+\rangle$). The opposite is true for negative fields (left).

At zero applied field, inversion symmetry dictates that the degree of polarization for both σ^+ and σ^- excitation are equal. Figure 4.6 shows the exciton and negative trion spectra for the four polarization excitation/detection combinations with $B = -7T$ (top) and $B = +7T$ (bottom). On the left (right) are the co- and cross-polarized spectra for σ^- (σ^+) excitation. Clearly the cross-polarized peak is saturated compared to the co-polarized peak in both cases; however, the degree of saturation is different. For positive applied field the saturation with σ^+ excitation is less (the cross-polarized peak is larger) than that for σ^- excitation, implying that the valley polarization in the +K valley is less than the -K valley. The negative applied field case is the time reversed analog of this case with stronger valley polarization in the +K valley over the -K. This observation implies that, while the helicity of the emitted radiation is determined by the incident helicity, the degree of polarization is determined by the relationship between the helicity and the applied magnetic field.

The top panel of figure 4.7 shows the degree of exciton valley polarization for both σ^+(blue) and σ^-(red) polarized excitation as a function of the applied magnetic field. Both helicities show linear behavior, but with opposite sign. This "X" pattern implies that the magnetic field induces an asymmetry in the valley scattering. At positive field, for example,

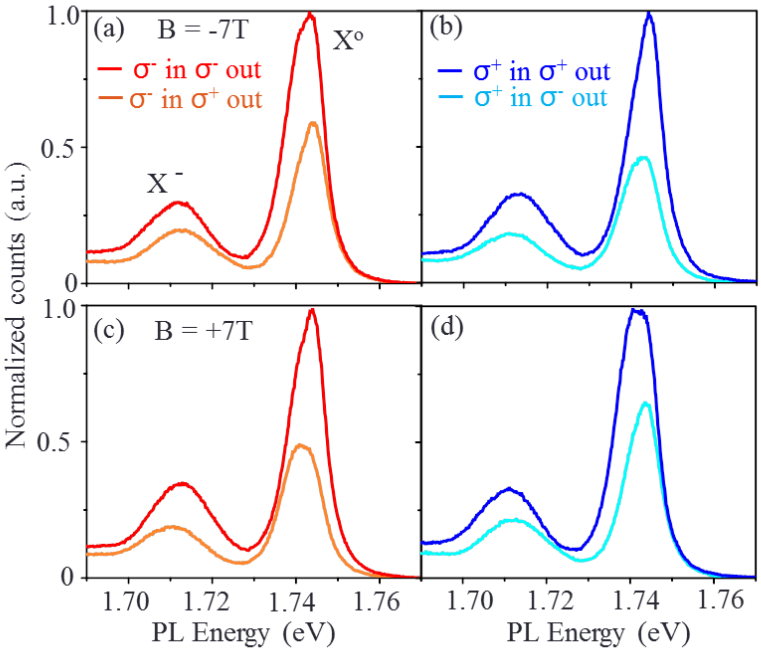

Figure 4.6: PL spectra for four incident/detection polarization configurations at B= -7T (top) and B= +7T (bottom) of X^o and X^-. Left panels are for σ^- polarized pump with co- (red) and cross-polarized (orange) detection. Right panels are the same for σ^+ polarized pump. Difference in cross-polarized peak saturation at different fields shows magnetic control over the degree of valley polarization.

carriers excited in the -K valley are less likely to scatter to the +K valley than vice versa. It is interesting to note that at positive magnetic field the $|\sigma^-\rangle$ state has a higher energy than the $|\sigma^+\rangle$ state, and it also has a larger valley polarization contrary to what would be expected under simple thermal relaxation. Contrast this behavior to the "V" pattern of the negative trion valley polarization shown in the bottom panel of figure 4.7, where the application of a field only serves to decrease valley scattering and enhance valley polarization.

All of these phenomena can be explained by looking at the valley-orbit coupled dispersions described by the potential matrix in equation 4.1. Depolarization can occur either in

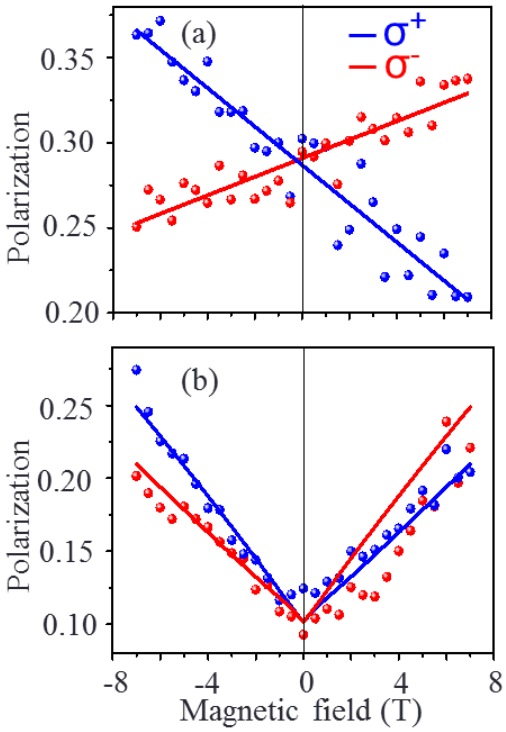

Figure 4.7: Degree of valley polarization for the neutral exciton (top) and the negative trion (bottom). Red (blue) corresponds to the $|\sigma^-\rangle$ ($|\sigma^-\rangle$) valley. "X" and "V" patterns stem from different intrinsic depolarization mechanisms for the two exciton states. Lines are fits to a rate equation model, see Ref [1].

the exciton formation process, or from relaxation between ground states once the exciton is formed. Detailed rate equations have been formulated for the case of both the exciton and trion valley polarizations in Ref [1]. Solving these rate equations for the different formation pathways and ground state recombination, taking into account the measured valley splitting, the data in Fig. 4.7 can be nicely fit.

For neutral excitons it is observed that the higher energy state in all cases has a larger degree of depolarization than the lower energy one, which is not what would be expected

from thermal relaxation between the ground states. This implies that the leading order depolarization mechanism is during the exciton formation. The case for the "X" pattern of the neutral exciton is due to the easier path of formation of σ^-excitons for $B > 0$ and σ^+excitons for $B < 0$ because of how the magnetic field shifts the excitonic dispersion.

When $B > 0$, σ^+excitation results in electron/hole pairs created near $\mathbf{k}$=0 in the +K valley which can relax to form $|\sigma^+\rangle$ excitons (in the lower branch of the dispersion) or flip valley and form $|\sigma^-\rangle$ excitons (in the upper branch) as shown in Fig 4.5. The rate of these two processes is different, as evidenced by the presence of the valley polarization; however, the effect of the magnetic field on both of these processes will be different. Since, for $B > 0$, σ^- emission occurs at the minimum of the upper branch we would expect the rates of processes resulting in a $|\sigma^-\rangle$ exciton to increases relative to the $B = 0$ case. Likewise, since σ^+ emissions occurs at the maximum of the upper branch we would expect the rates of processes resulting in a $|\sigma^+\rangle$ exicton to decrease relative to the $B = 0$ case. These results combined would imply $\rho_{\sigma^-}(B > 0) > \rho_{\sigma^\pm}(B = 0) > \rho_{\sigma^+}(B > 0)$, as observed. The case for $B < 0$ is the time reversal of this analysis.

The negative trion picture is a little more complicated due to the presence of the extra electron. As shown in the top of Fig 4.8 there are four lowest energy combinations of a valley exciton and an extra electron, which can each be denoted by its valley pseudospin and electron spin. However, when all three particles have the same spin a large exchange interaction breaks the degeneracy between the $|\sigma^+,\uparrow\rangle$ ($|\sigma^-,\downarrow\rangle$) and $|\sigma^-,\uparrow\rangle$ ($|\sigma^+,\downarrow\rangle$). At $B = 0$, these can be arrange into two degenerate sets of valley-orbit coupled bands with an opened gap, $\delta \sim 6$ meV[100], at $\mathbf{k}$=0. Since δ is much larger than the valley Zeeman splitting at all fields, asymmetry of the exciton formation rates does not dominate the magnetic field dependence of the valley polarization. Instead, the field breaks the degeneracy between the two set of dispersion curves and suppresses valley flipping scattering between them. In this way an applied field of either sign serves to suppress valley flipping and increases the valley polarization, as observed.

The fundamental difference between the "X" and "V" patterns is the difference in valley depolarization mechanisms. Depolarization during exciton formation results in and "X" pattern as formation prefers the lower momentum upper branch. Whereas depolarization

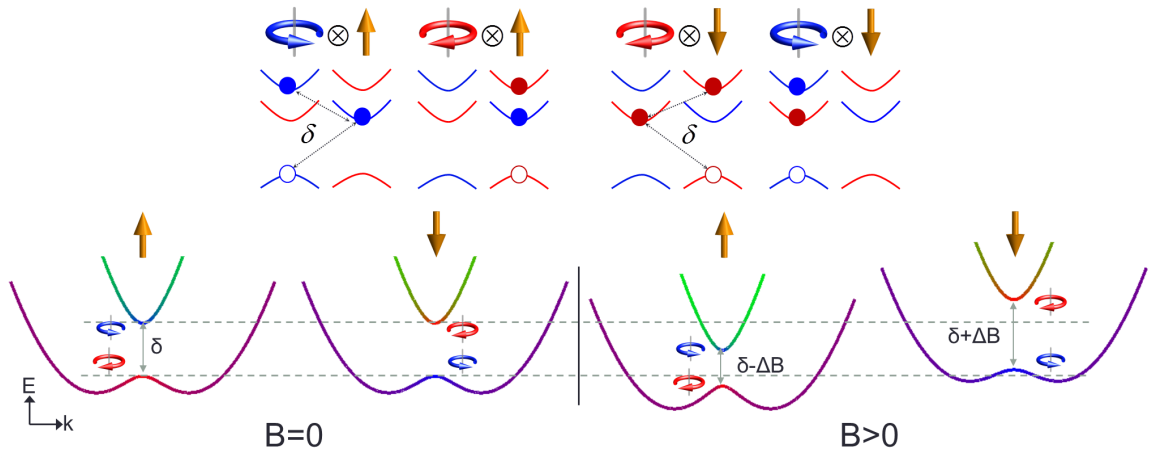

Figure 4.8: The four different trion configurations are given in the top panel denoted by the helicity of the initial exciton (blue and red circular arrows) and the spin of the extra electron (gold up and down arrow). Due to the exchange interaction the states $|\sigma^+,\uparrow\rangle$ and $|\sigma^-,\downarrow\rangle$ have a higher energy than the other two states. This is shown in the bottom figure at left, for $B = 0$, with the two separate trion dispersion curves showing an opened gap and a different valley trion in both the upper and lower branches of each dispersion curve (denoted by the red and blue colors at the band edges). The valley Zeeman effect (right panel) is then a small perturbation on the already present gap, breaking the degeneracy between the two dispersion curves.

occurring from the ground state will give a "V" pattern since the field only serves to suppress valley flipping.

For the positive trion, the picture is more like that of the exciton. The large spin orbit splitting of the valence band results in no holes in the lower band, so there is only one X^+ configuration for each valley, and it has no exchange interaction since the lowest energy state requires the extra hole in the trion to be in the opposite valley and thus have the opposite spin as the other two particles in the trion. This would then imply that the magnetic dependence of the valley polarization should have an "X" dependence, which is indeed observed (see Figure 4.9b).

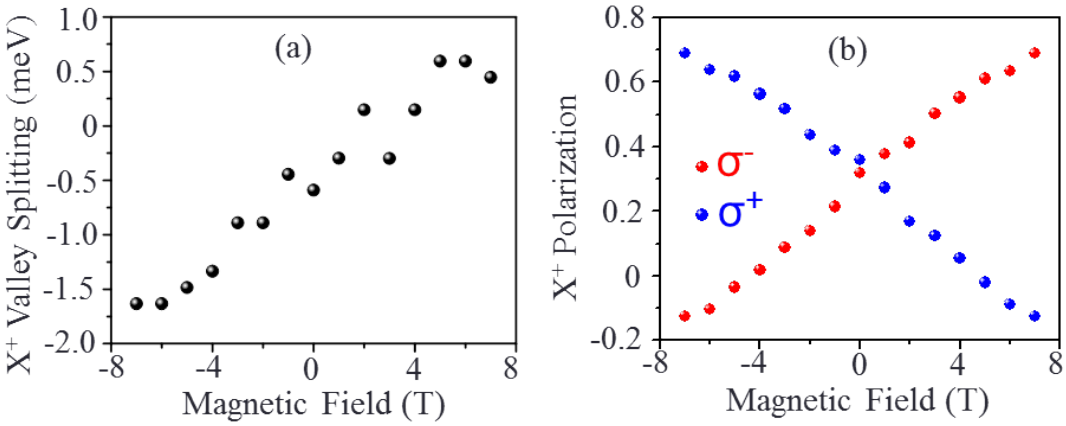

Figure 4.9: Valley splitting (left) and polarization (right) for the positive trion.

As shown in Figure 4.9, the magnetic dependence of the valley physics for the hole trions show many very interesting features. In (a), the valley splitting as a function of field has a similar linear trend as for the exciton and the electron trion; the splitting slope, while being of similar magnitude, is of the opposite sign, however. The polarization "X" pattern is, again similar to what is seen with the neutral exciton, except the tuning range of the field is much larger, and even crosses zero. For large fields the dominate polarization of the emitted PL is no longer set by the incident polarization, but by the sign of the magnetic field.

This is shown in more detail in Figure 4.10, where the full spectra are plotted at different magnetic field. In the center at B= 0T, the spectra behave as expected, with the co-polarized peak (blue in the top row and red in the bottom row) is larger than the cross polarized peak for both X^+ and X^o. At B= +7T (right panels) the dominant X^+ emission is σ^- polarized (red) regardless of the incident polarization. While in both pump configurations the cross-polarized exciton peak is saturated compared to the co-polarized one. The opposite is true for B= -7T. A theory to explain these observation is still being worked on.

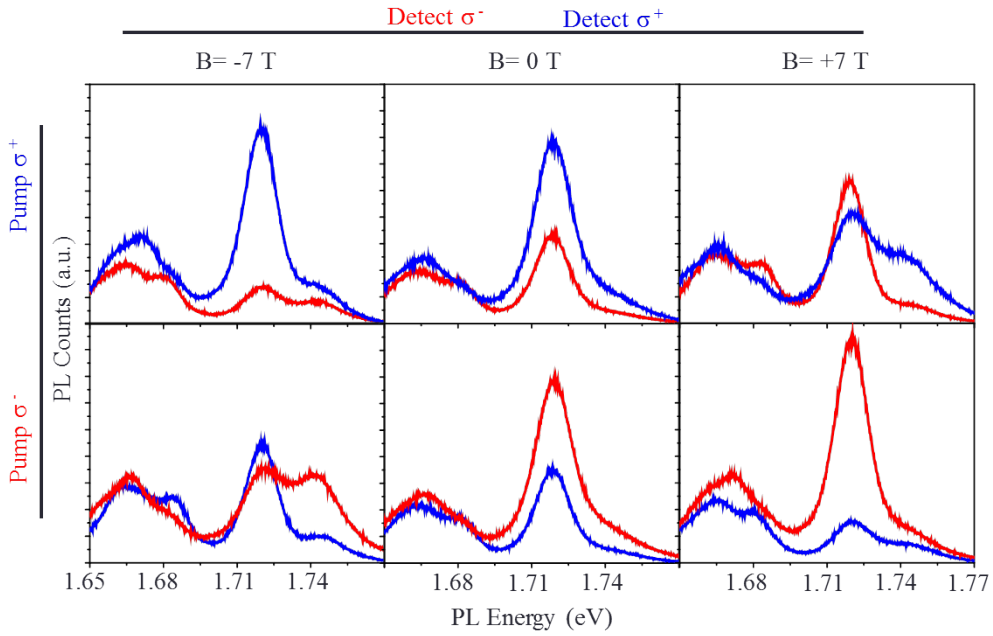

Figure 4.10: PL spectra for four incident/detection polarization configurations at B= -7T (left), B= 0T (middle), and B= +7T (right) for X^+. Top (bottom) panel shows spectra for σ^+ (σ^-) polarized pump, with blue (red) being σ^+ (σ^-) detected PL. At high field sign of dominant X^+ emission is determined by the field not the pump polarization.

4.4 Gate Dependence of Valley g-Factor

Over the course of this experiment many different samples were measured and it was noticed that there was a significant spread in the measured valley splitting. This is commented on in Ref [1], but at the time the reason for the spread was unknown. However, a very interesting trend falls out of the seemingly random spread if the valley splitting is plotted as a function of the trion-to-exciton ratio, which serves as a proxy for the sample doping. This is shown in Figure 4.11. The bottom axis, X^i/X^o, is the peak amplitude of the trion species X^i ($i = +, -$) divided by the peak amplitude of the exciton in each spectra, for example the spectra in figure 4.6 have a ratio of ~0.3. The plot shows data from over a dozen different samples, and some samples measured on multiple cool downs. This ratio serves as a rough

identifier with the doping in the sample; however, it must be noted that the doping is not necessarily linear in this ratio, but it is at least monotonic. A value of 0 corresponds to an exclusively exciton PL, while ± 1 corresponds to equal amplitudes of X^o and $X^{\mp}$.

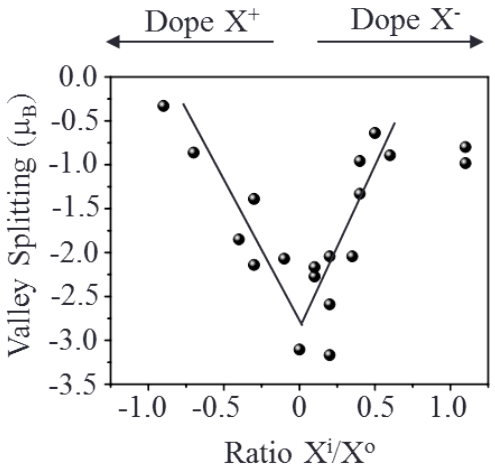

Figure 4.11: Exciton valley splitting of 15 different samples plotted against the ratio of the trion amplitude to the exciton amplitude, as a proxy for the sample doping. Valley splitting shows a clear dependence with the largest splitting at no doping.

Obviously the exciton valley splitting has a strong dependence on this ratio, and thus the sample doping. Near zero doping the exciton has a g-factor of nearly -3.5 μ_B, corresponding to a smaller, but still positive, $\Delta\alpha$ than presented in Section 4.2. This indicates that in this regime the carriers behave closer to massive Dirac fermions and the overall valley splitting is dominated by the magnetic moment associated with the parent atomic orbitals, Δ_A. The splitting then becomes smaller (closer to zero) as the sample is doped, implying that the contribution from the valley magnetic moment, Δ_v, and subsequently $\Delta\alpha$, grows larger. This may be due to the presence of extra carriers distorting the band structure and pushing the carriers away from the simple massive Dirac fermion picture. However, theoretical simulations of this effect have not yet been performed to confirm this.

For a more complete understanding of this effect a gated sample is measured as a function of the gate voltage (doping) for a fixed magnetic field, B= +5T in this case. For each

gate voltage the four combinations of incident/detected polarizations are measured to investigate the gate dependence of the valley splitting and valley polarization. This is shown in Figure 4.12. Panel (a) shows the peak amplitude of the different exciton species as a function of the gate voltage. At large negative bias the sample's PL is dominated by the X^+ trion (green) as would be expected. Around 0V this gives way to the neutral exciton (black), X^o. However, the negative trion, X^- (purple), does not come in strongly at the applied voltages, meaning that the measurement is only probing the left half of figure 4.11.

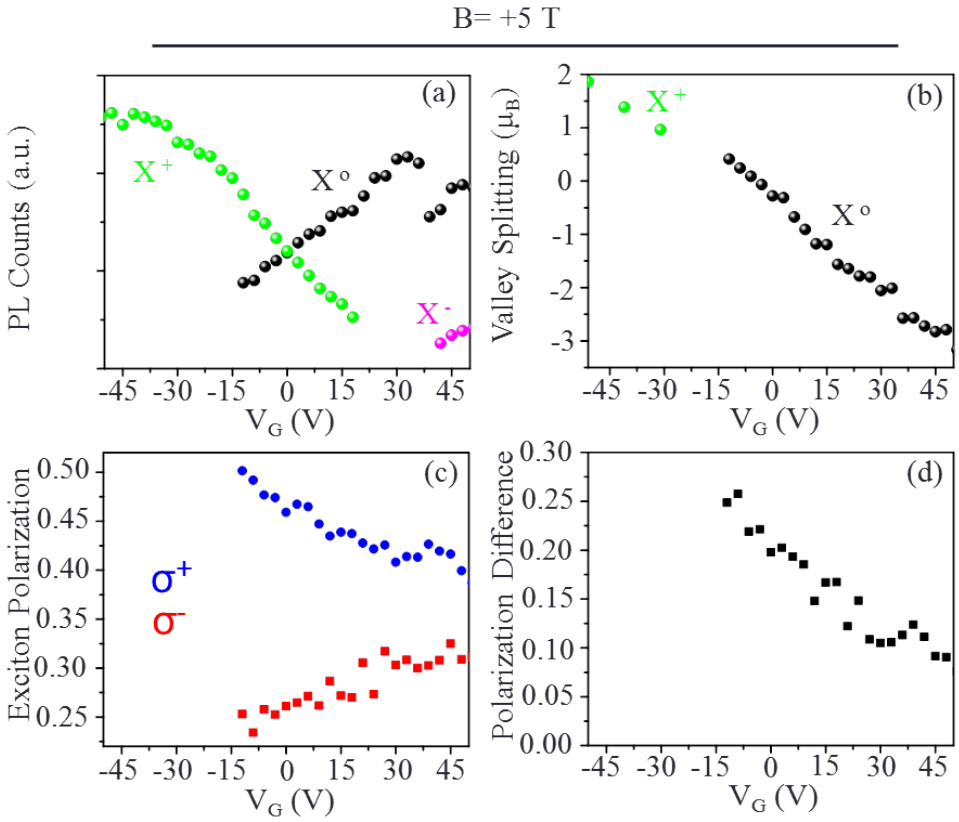

Figure 4.12: Gate dependence of magnetic valley physics at B= +5T. A) amplitudes of the different exciton species as a function of the gate voltage. B) valley splitting of X^0 and X^+ shows gate tunability. C) exciton valley polarization and (D) difference in valley polarization ($\rho_{\sigma^+} - \rho_{\sigma^-}$) is also strongly modulated by the gate.

Figure 4.12b shows the measured valley splitting for the positive trion (green) and the neutral exciton (black). The gate clearly has a strong dependence on both of these values, and the exciton splitting shows as similar range of tunability as indicated in Figure 4.11 for different samples. However, since the full spectrum of the doping could not be applied to bring out the negative trion at higher gate voltages, it is unclear yet if the spectrum will indeed turn around as hinted in Figure 4.11 and what the peak valley splitting will be. This preliminary data, though, looks very promising.

In Figure 4.12c the valley polarization for both the $|\sigma^+\rangle$ and $|\sigma^-\rangle$ neutral excitons also show a strong gate dependence. The difference in the polarization, $\rho_{\sigma^+} - \rho_{\sigma^-}$, is shown in panel d. Interestingly this shows the $|\sigma^+\rangle$ exciton is more strongly polarized at B= +5T than the $|\sigma^-\rangle$ one (positive polarization difference), which is the opposite of what was seen previously in Figure 4.6 (negative polarization difference). The previous spectra, however, where taken under electron doping (positive effective gate) whereas this data is taken under hole doping (negative effective gate). Clearly the gate dependence in Figure 4.12d shows the polarization difference trending towards a sign switch and negative values at higher gate; which would agree with the previous observations.

It then appears that the while the magnetic field serves to beak the valley degeneracy, the sign of the breaking is determined by the doped free carriers in the system, not on the valley exciton dispersion splitting theory presented in the previous section. This is a very interesting results and offers yet another method of controlling the valley physics in WSe_2 ; however, more work still needs to be done. As of yet, no theory has been developed to explain these observations, and a complete set of data must be taken to confirm that the trends set up in Figure 4.12 continue under electron doping. Unfortunately the cryostat these measurements are taken in has been found to be hole doping the samples, preventing the application of gate voltages large enough to reach electron doping. As of the time of this writing, this issue is currently being investigated.

Previous work [90] investigated the use of an electric field to break the inversion symmetry in bilayers of MoS_2 and thus tune the valley magnetic moment, from positive through zero to negative values. There the gate serves only to provide a vector to break inversion symmetry and not for the doping of the sample. Here it seems the magnetic moment's

modulation is due to the effects of doping not the applied electric field.

4.5 Magnetic Dependence of Valley Coherence

The presence of a magnetic field breaks the valley degeneracy and introduces an asymmetry in the valley scattering, this should have an effect on the valley coherence. As discussed in Section 2.4 a valley superposition can be created through excitation with linearly polarized light [28, 95], as shown by the saturation of the cross-linearly polarized signal compared to the co-linearly polarized one. Figure 4.13 shows the linear polarization of the exciton and negative trion for $B = -7$T (left), $B = 0$T (middle), and $B = +7$T (right) for V polarized excitation. Clearly in all cases the the cross polarized peak (H, black) is saturated compared to the co-polarized one (V, purple); however, when the field is applied this saturation is reduced, indicating a suppression of the valley coherence. This can be seen clearly in the lower panel where the degree of linear polarization if plotted as a function of the applied field for both V (purple) and H (green) polarized excitation. Both cases show a "Λ" shape demonstrating the reduced valley coherence in the presence of the applied field. The fact that both polarization agree implies that this effect is inherent in the sample, and not dependent on some particular crystal axis. Also notice that there is still no saturation of the negative trion signal, implying these states are still not coherent in the applied field.

Decoherence of the valley pseudospin, like valley depolarization, can occur either during the formation process or from ground state relaxation. The later process can occur through the procession of the spin, known as the Hanle process, and is consistent with the observed "Λ" pattern. In this case the half width of the peak in Fig 4.13 corresponds to the decoherence rate. However, the extracted value of $\sim$ 1ps[1] is much faster than those extracted from time resolved measurements[85]. Therefore, it is like that the exciton formation mechanism is the dominate pathway for valley decoherence. In the presence of a magnetic field, the pathways through which free electron/hole pairs create $\mathbf{k}$=0 excitons in either the valley (upper/lower branch) will be different. It is most like this difference that results in decoherence in the formation of the excitons, and a reduced linear polarization.

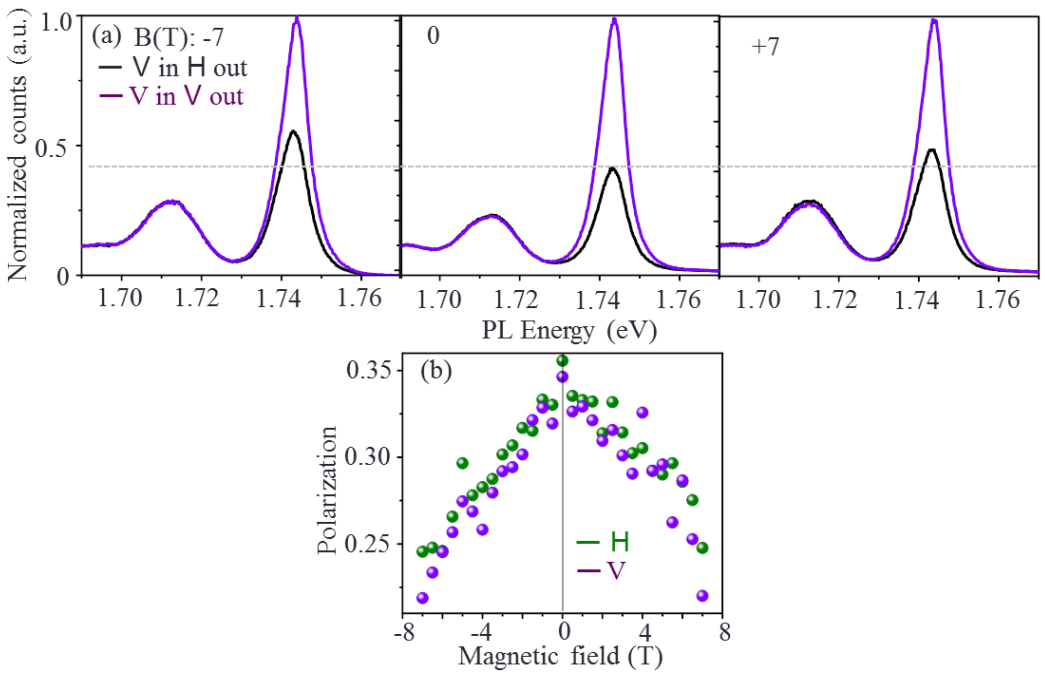

Figure 4.13: Field dependence of valley coherence. Top shows spectra with linear excitation and detection and -7 T (left), 0 T (middle), and +7 T (right) applied field. The degree of saturation of the cross polarized peak (which is related to the valley coherence) diminishes with applied field. Bottom shows this saturation as a function of the applied field strength.

4.6 Outlook and Future Work

The valley pseudospin in WSe_2 is a good quantum number as valley excitons are robust against inter-valley scattering. Through excitation with circularly polarized light a valley polarization can be established and read-out via the polarization of the emitted PL with good fidelity [95]. The work presented in this chapter represents the first investigation of the use of a magnetic field as a way to control these valley properties. With more refinement the valley pseudospin has a potential use as a qubit in future quantum computers, and external magnetic fields have now been shown to provide the control needed to perform possible

quantum operations.

Before that can be a realistic possibility much more work needs to be done in exploring these magnetic valley properties. As was shown in Section 4.4, these properties are strongly modulated by a gate, but the mechanism behind that is not fully explained theoretically and in fact is often at odds with the current explanations for the magnetic valley properties. Much more experimental and theoretical work is still in need of before these phenomena can be fully understood. First and foremost in the completion of the gate dependent sweeps to include all three trion species and fully map out the gate tunability.

Other properties may also play an important role in the observation of these magnetic properties. The Zeeman splitting is fairly small ($\approx$1 meV) at these fields, so the temperature of the lattice is very important. At some higher temperature there would be enough thermal energy to overcome the Zeeman splitting and wash out the magnetic observations. Additionally it would be of interest to push the field to higher strengths to investigate the limit to the linearity of the Zeeman effect. At the National High Magnetic Field Lab, a setup is already in place to measure these phenomena up to fields of 17T. Finally, strain in the crystal lattice can serve to mix the two valleys which may have interesting consequences on the Zeeman splitting. Additionally, when under stain the band edges perturb which will certainly alter the valley magnetic moment.

One of the major limitations of using PL to monitor these magnetic valley effects is that the width of the standard PL peak ($\sim$5 meV) is much larger than the valley Zeeman splitting strength, making it difficult to accurately extract out the valley splittings. Especially so, since the PL peaks do not fit well to a standard Lorentzian or Gaussian profile. Using a higher resolution spectroscopy could serve to more precisely quantify the splittings in an applied field.

Part II

PHOTOCURRENT GENERATION IN GRAPHENE FETS

Chapter 5

ULTRAFAST PHOTOCURRENT GENERATION IN GRAPHENE

The second half of this thesis will focus on the generation of photo-excited currents in graphene FETs. This chapter will describe the general properties of semi-metallic single layer graphene and investigate the photocurrents create at PN-junctions in this material. It will be shown that the creation of the photocurrent is dominated by hot carriers and its subsequent decay characteristics due to the small overlap in phase space of electrons and phonons, as well as the electronic bottleneck created at the Dirac point where the density of states goes to zero. The subsequent chapters will explore the effects of breaking the continuous band structure with small energy gaps on photocurrent generation and lifetimes. In chapter 6 a band gap of several hundred meV is opened up in bilayer graphene leading to enhanced photocurrent generation and prolonged lifetimes of the excited carriers. Finally in chapter 7 a magnetic field is used to create discrete Landau level through which electronic cooling must take place leading to oscillations in both the photocurrent generation and cooling times.

There are many excellent reviews of the electrical [8, 20] and optical [5] properties of graphene, as well as a recent experimental outlook [12, 18], for the interested reader.

5.1 Graphene Stucture and Electronic Properties

5.1.1 Electronic Properties

Graphene is composed of a single layer of carbon atoms arranged into a two-dimensional honeycomb lattice. Similarly to the TMDs presented in Part I, its low energy band structure is located at the edges of the first Brillouin zone, at the K points; however, graphene is inversion symmetric which requires the absence of a band gap. Indeed near the K-points graphene's band structure displays a linear, conical shape, with the conduction and valence bands meeting at a single point, known as the Dirac point, see Figure 5.1. Interestingly

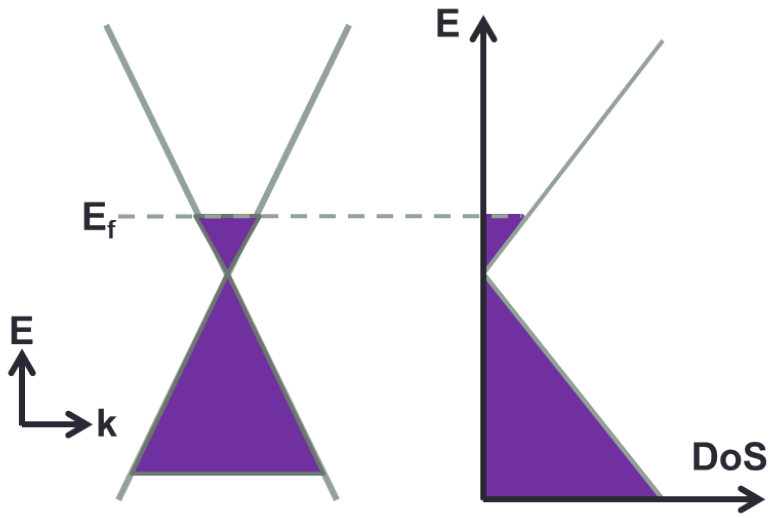

Figure 5.1: Left: Plot of the low energy electric band structure near the K-point of single layer graphene, showing the linear dispersion and the Dirac point. Right: Plot of the corresponding density of states which vanishes at the Dirac point.

due to its linear dispersion and 2-D nature, the density of states in single layer graphene is also linear in the energy, with a vanishing density of states right at the Dirac point. This has interesting consequences to photoexcited carriers. Graphene is typically thought of as a semi-metal– while it in fact does have a continuous band structure, the vanishing density of states creates an electronic bottleneck which can slow electron cooling.

The presence of inversion symmetry also makes the two valleys, $\pm$K, indistinguishable as well as degenerate, unlike in TMDs. Additionally since graphene is composed solely of light nuclei the spin-orbit interaction is negligible, and all bands are spin degenerate as well. Therefore each band has a four-fold degeneracy from valley and spin. This factor of four appears in the Landau level spectrum, where each level is separated by four conductance quanta [20]. Additionally, this degeneracy can be broken upon application of a large magnetic field, giving the full-integer Quantum Hall Effect [103]. These effects are discussed in more detail in Chapter 7.

5.1.2 Phonons in Single Layer Graphene

Graphene has six phonon modes– 3 acoustic modes and 3 optical modes (transverse, longitudinal, and out of plane)– which play a major role in the generation of photocurrents in graphene. The dispersion of these modes are shown in Figure 5.2. Scattering between low energy carriers and phonons can either be valley conserving ($q \approx 0$) or valley flipping ($q \approx K$) and must include an in plane phonon mode (not ZA or Zo) to conserve momentum. It is evident from Figure 5.2 that valley flipping scattering events require an energy of several hundreds of meV and thus are possible for only extremely hot carriers. Valley conserving scattering requires a low momentum phonon so that the electron can stay on the relatively narrow conical dispersion. Near $q = 0$ the in-plane optical phonon modes again have an extremely high energy (several hundred meV) and are therefore not available scatters for lower energy carriers. This leaves only the in-plane acoustic phonons, TA and LA modes, as participants in low energy carrier phonon scattering, and these phonons have very little energy. Under these conditions alone there is a very weak coupling between

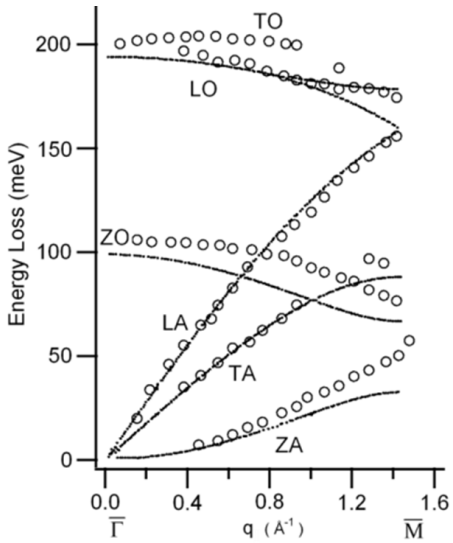

Figure 5.2: Phonon dispersion of single layer graphene. Plot shows the six different phonon modes, 3 acoustic and 3 optical phonon modes. Circles are data taken from EELS and solid lines are DFT calculations. Plot taken from Ref [58].

optically excited hot carriers and the lattice, which implies extremely long carrier cooling time[3, 81]. As will be shown later, however, this is not the case.

5.1.3 Graphene Devices

A typical dual gated graphen FET is shown in Figure 5.3. Graphene devices are formed by mechanically exfoliating (through the so call "scotch tape method") graphite flakes onto heavily doped silicon substrates with 300 nm of SiO_2 grown on top. The doped substrate can be used as a back gate with the Sio_2 as the gate dielectric. This precise thickness of the dielectric is required to gain optimal optical contrast of the exfoliated graphene flakes to facilitate identification of single layer samples [54]. Electron beam lithography can be used to pattern source and drain electrodes which are deposited via an electron beam metal evaporator (typically 1 nm Cr and 30 nm Au). Care must be taken during fabrication for optimal cleanliness, since any residue can severely damage the electrical characteristics. Boron nitride (BN), a wide bandgap insulating cousin of graphene, is often used as a substrate or top gate dielectric for graphene devices [16]. As a substrate, BN serves to smooth the rough surface of thermally grown SiO_2 and serve as a lattice match for the graphene crystal, both of which greatly enhance the electrical performance of the device. Transfered on top of the graphene, the BN can serve as an encapsulation to prevent device degradation or serve as a low leakage top gate dielectric. Finally, the heavily doped substrate can be used a global back gate. Fabrication of pristine graphene devices is the subject of many publications and entire theses [16, 18], but is not the focus here.

The linear nature of the low energy electronic dispersion means that the electrons/holes are best described as massless Dirac fermions. This has interesting ramifications as a condensed matter analogue to relativistic particle physics. Additionally it gives rise to graphene's tremendous electron mobility. Today's typical samples have electron mobilities in the range of 10^4 $cm^2V^{-1}s^{-1}$ with the best devices breaking 10^6 $\mathrm{cm^2V^{-1}s^{-1}}$, compared to typical values for silicon of $10^3\mathrm{cm^2V^{-1}s^{-1}}$.

The electron mobility is best calculated by looking at the Hall conductance of a graphene devices. Typically, however, a capacitive model is used to estimate it. For the typical

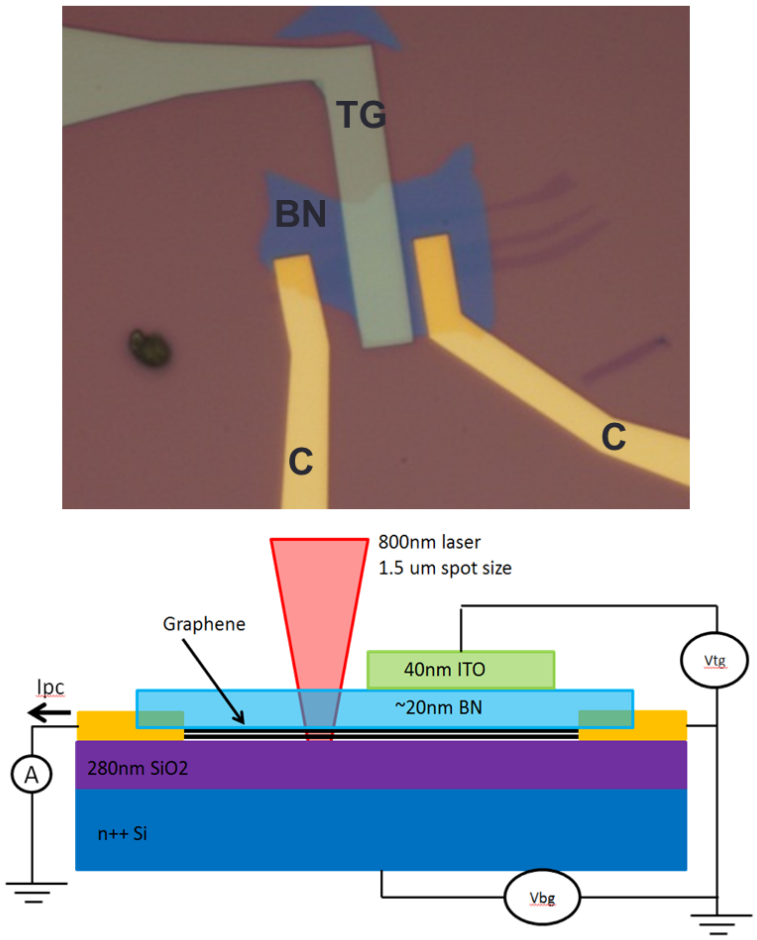

Figure 5.3: Picture of a typical dual gated graphene devices. Graphene appears as thin dark strip in middle. Source and drain electrodes are created using electron beam lithography and are marked as "S" and "D". A piece of thin BN (blue triange) is transfered on as a top gate dielectric. Top gate is written with a second electron beam lithography step and marked "TG". The conducting silicon substrate is used as a global back gate.

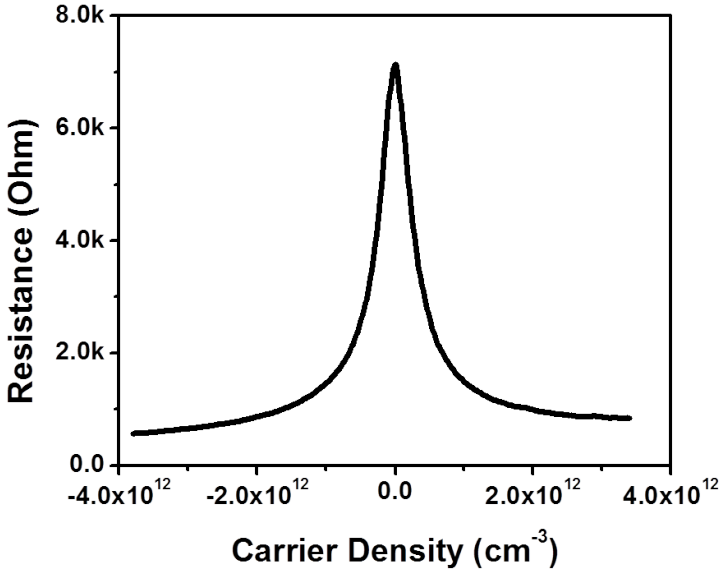

Figure 5.4: Resistance of a typical graphene FET as a function of the global back gate. The peak value corresponds to neutral doping and is referred to as the Dirac point. Steeper falloff from this point in indicative of a larger carrier mobility.

graphene device described above, the electron density can be estimated as $n = c_g(v_g - v_{DP})/e = c_g\Delta V/e$, where c_g is the gate capacitance per unit area and ΔV is the deviation of the gate voltage from the voltage of the Dirac point, with positive (negative) n corresponding to electron (hole) doping. For 300 nm of SiO_2, $c_g = 115$ aF/μm^2. The conductivity, σ, is related to the mobility, μ, by $\sigma = ne\mu$. So from the slope of a typical conductivity versus gate voltage plot (see Figure 5.4) the mobility can be calculated as

$$\mu = \frac{1}{e}\frac{d\sigma}{dn} = \frac{1}{e}\frac{d\sigma}{dv_g}\frac{dv_g}{dn} = \frac{1}{c_g}\frac{d\sigma}{dv_g} \tag{5.1}$$

5.2 Photocurrent Generation in Graphene PN Junctions

Due to its linear dispersion and lack of a band gap, graphene has a remarkably broadband and flat optical absorption. This means that incident optical radiation serves as more

of a local thermal source rather than to excite a specific optical transition. The specific mechanism that describes the creation of photocurrents (PC) has been the study of many different investigations [5, 12]. Clearly for any specific spot to generate PC upon optical excitation the left/right symmetry must be broken. This can be accomplished through either a hetero-junction, such as a single/bilayer graphene junction [94] or a metal/graphene contact junction [36], or at a homojunction in a single material with different spatial doping profiles [69], such as in a pn-junction [17, 21, 75].

5.2.1 Photocurrent Microscopy

A very useful technique for exploring the spatial dependence of the photo-active areas on a devices is scanning photocurrent microscopy (see [36, 75]). A laser beam is focused to a tight spot ($\sim 2\ \mu$m) onto the surface of the sample. At this point the current generated and the light reflected are collected. By modulating the incident laser's amplitude with a mechanical chopper ($f =\sim 1-2$ kHz) and using lockin techniques the signal-to-noise ratio is greatly improved. At this point the laser focus can be raster scanned in two-dimensions using a pair of galvo-scanning mirrors setup in a scanning confocal microscope configurations, see Figure 5.5. In this way a map of the PC generated at different points on the sample is obtained, as well as the reflection image which can be used to correlate photo-active hot spots to physical locations on the device. For all of the work presented in this thesis the excitation laser, whether CW or pulsed, was in the near IR from a Ti:Sapphire laser with an energy of 1.65 eV.

Figure 5.6 shows the output maps of a dual gated graphene device (see Figure 5.3) from the scanning PC microscope. In this image the global back gate has n-doped the entire device, while the local top gate is set to p-dope the region underneath it. This creates a np- and pn- junction to the left and right of the top gate, which one would expect to be strongly photo-active. Clearly the largest generated PC in the right panel appear in lobes of opposite polarity on either side of the top gated region, as seen by comparison with the reflection image on the left. Smaller PC spots are generated at the contacts where the graphene/metal junctions form a Schottkey-junction which is also photo-active. It is important to note that

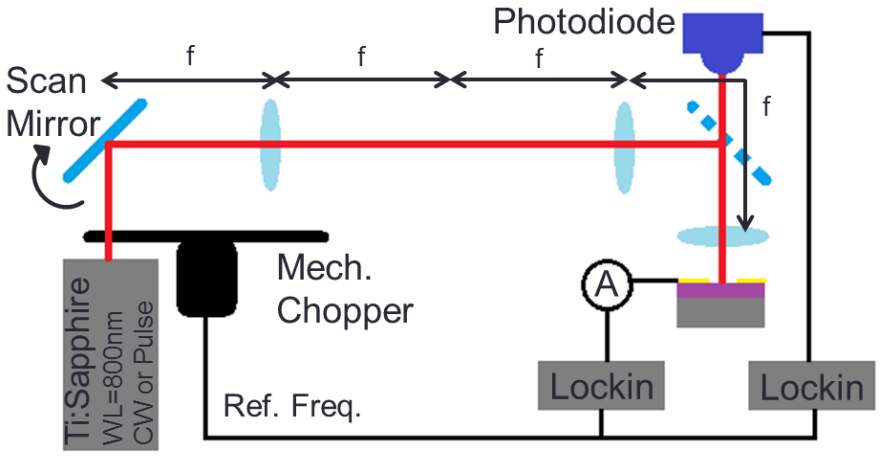

Figure 5.5: Schematic of the optical layout for a scanning photocurrent microscope. The focus of an incident laser beam is scanned across a sample using a 2-D galvo-scanning mirror while the reflected light and PC are simultaneously recorded.

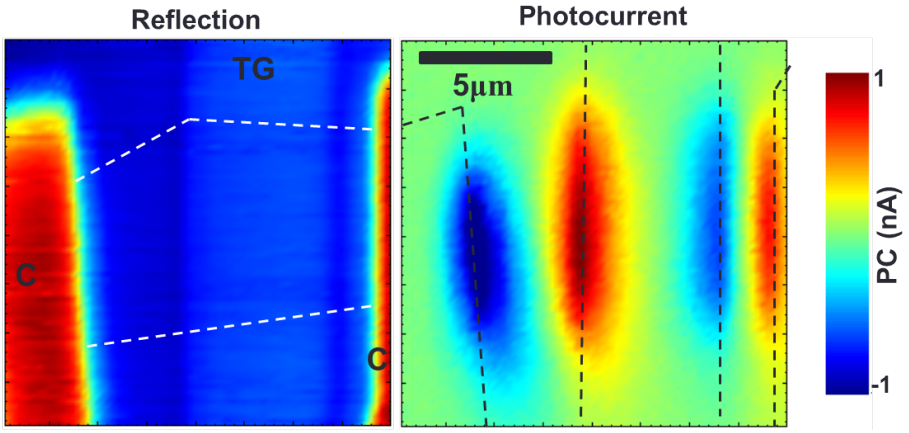

Figure 5.6: Graphene pn junction measured with the scanning photocurrent microscope. Left: optical reflection image of the dual gated graphene device clearly showing the contact ("C"), top gate ("TG"), and graphene channel (dashed white lines). Right: map of the locally generated photocurrents. Clearly the different peaks can be identified with the pn-, np-, and graphene/metal junctions.

the PC generation is highly localized to these specific junction areas, with no PC generated in the bulk of the device. These maps show that PC generation is a local effect and requires a mechanism to break the left/right symmetry so as to separate the photoexcited electrons and holes. The specific mechanism of this generation will be explored in the next section.

5.2.2 Mechanism of Photocurrent Generation

At a pn- or Schottkey- junction the built in electric fields are surely capable of separating the electrons and holes so as to create a net PC, though there is another effect that one must also consider: the photothermoelectric (PTE) effect. In this case a current is generated in response to a laser induced temperature gradient between materials with different thermoelectric powers, S, also known as the Seebeck coefficient.

$$I = \frac{(S_1 - S_2)\Delta T}{R} \tag{5.2}$$

Where R is the device resistance and S given by the Mott relation[94].

$$S = -\frac{\pi^2 k^2 T}{3e}\frac{1}{\sigma}\frac{d\sigma}{dE} = -\frac{\pi^2 k^2 T}{3e}\frac{1}{\sigma}\frac{d\sigma}{dV_G}\frac{dV_G}{dE} \tag{5.3}$$

With conductivity σ and $d\sigma/dV_G$ obtained from the resistance measurement (see Figure 5.4) and $E = \hbar v_f \sqrt{\pi c_g V_G/e} = 31\sqrt{V_G}$ meV is the Fermi energy as a function of gate voltage for monolayer graphene. The dependence of S on the doping is shown in Figure 5.7, showing its characteristic nonmonotonic, "S" shape.

The generated PC is proportional on the difference between the Seebeck coefficients in the two separate regions of the pn-junction. If in one region the doping is constant with a Seebeck coefficient of, for example, 5 μV/K, then as the carrier concentration is swept in the other region the generate PC would switch signs twice— at -2.3 and -0.1 V— as the Seebeck coefficient crosses 5 μV/K.

On the other hand the standard photovoltaic effect at a pn-junction describing the PC generated by the built in electric field, however, follows a monotonic dependence on the sample doping. There exists only one sign reversal, when the doping in one region crosses the doping in the other and the junctions goes from a pn- to a np- junction.

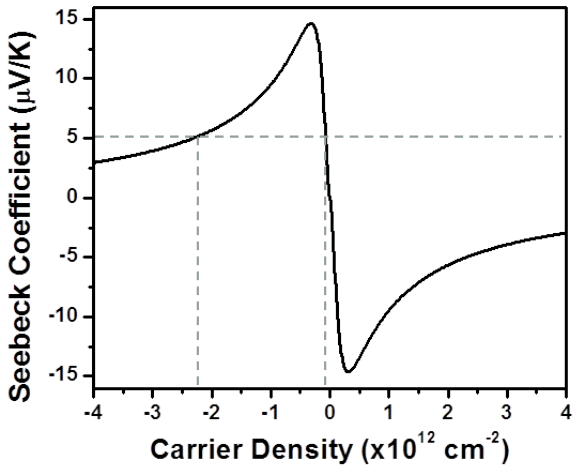

Figure 5.7: The effect of doping on the Seebeck coefficient calculated for the device shown in Figure 5.4.

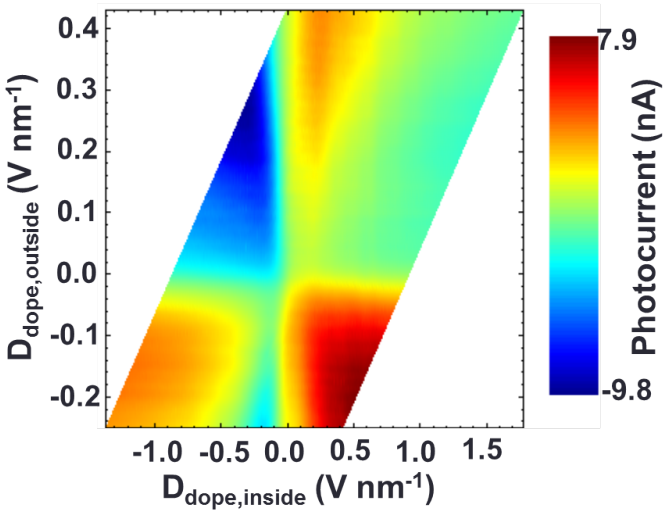

Figure 5.8: Photocurrent generated at a graphene pn-junction as a function of the doping level in the two regions. The characteristic six-fold pattern, with multiple sign reversals as a function of the doping, is indicative of a hot-carrier photothermoelectric effect dominating the PC generation.

Thus by looking at the PC generated as a pn-junction as a function of the doping in both regions the mechanism of PC generation should be obvious by the number of sign reversals [17, 69]. This is shown for a dual gated graphene pn-junction in Figure 5.8 as a function of the doping inducing electric field inside and outside the top gated region. The map here shows and interesting 6-fold pattern of positive and negative PC. The multiple sign reversals are a clear indication that the photothermoelectric effect is the dominant PC generation mechanism, and the hot carriers dominate the optoelectronic properties.

5.3 Pulsed Excitation of Hot Carriers

Things are different under pulsed excitation where now the energy is compressed into a short duration. For the same average intensity, pulsed excitation leads to a substantially higher peak power and long durations of no illumination compared to CW excitation. This will typically lead to an increase in the hot-carrier temperature as well as a saturation in the total photoexcited current as shown in Figure 5.9. Clearly there is strong saturation of the pulsed excited PC compared to the CW excited ones for all temperature due to the fact that the CW excitation occurs over a longer duration than the pulsed one. The lack of any temperature dependence to the pulsed excitation is due to the fact that the carriers in this case are excited to such a high effective temperature (several thousand K) that relatively small changes in the lattice temperature has no real effect, unlike the case for the cooler effective temperature (several tens of K) created from CW excitation [21].

5.3.1 Pump-Probe Photocurrent

One method to determine the cooing times of photo-excited hot carriers in a device is pump-probe photocurrent. Similar to the optical pump probe method described in Section 3.1, this method utilized two pulses of the same laser separated by a fixed time delay to excite the system and then measure the response a moment later; however, in this case the readout will be the photocurrent generated by the probe pulse, *i.e.* the total current measured at the modulation frequency of the probe pulse. So for large time delay the signal should be photocurrent generated by the probe pulse alone. At zero time delay the sample sees a single laser with the power being the sum of the powers of the pump and probe pulses. In

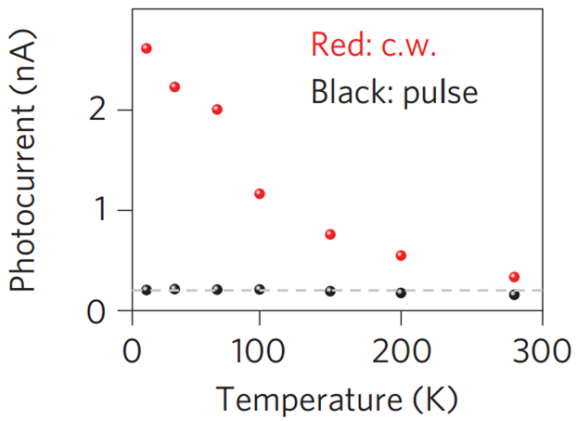

Figure 5.9: Generated photocurrent as a function of temperature for both pulsed (black) and CW (red) excitation with identical average power. Pulsed excitation shows strong saturation compared to CW excitation and no temperature dependence.

the linear regime this would give the same photocurrent reading as long time delay, since the measurement is only sensitive to the current generated by the probe pulse; however, as shown in Figure 5.10a and in the saturated behavior of probe pulses in Figure 5.9 the response of a graphene device to pulsed excitation is not linear. Therefore the combined power of the pump and the probe pulse, while indeed exciting net more current than either pulse alone, excites less per pulse than either pulse alone. In this case the pump probe signal at zero delay should show a dip corresponding to the saturation of the probe pulse's signal in the presence of the currents generated by the pump pulse.

An example time series is shown in Figure 5.10b. The signal is symmetric around zero time delay, so only part of the negative time delay is scanned. Clearly the signal is flat for large time delays, and for $\tau < 20$ ps there is a definite dip corresponding to the saturation effect described above. The depth of the dip tells about the magnitude of the pump induced saturation. The timescale of the dip tells about the cooling time of the hot carriers excited by the *pump* pulse, since it is the presence of these extra carriers that results in the saturation of the photocurrent generated by the probe pulse. The effects on these time series of various effects like temperature and doping have been extensively examined in

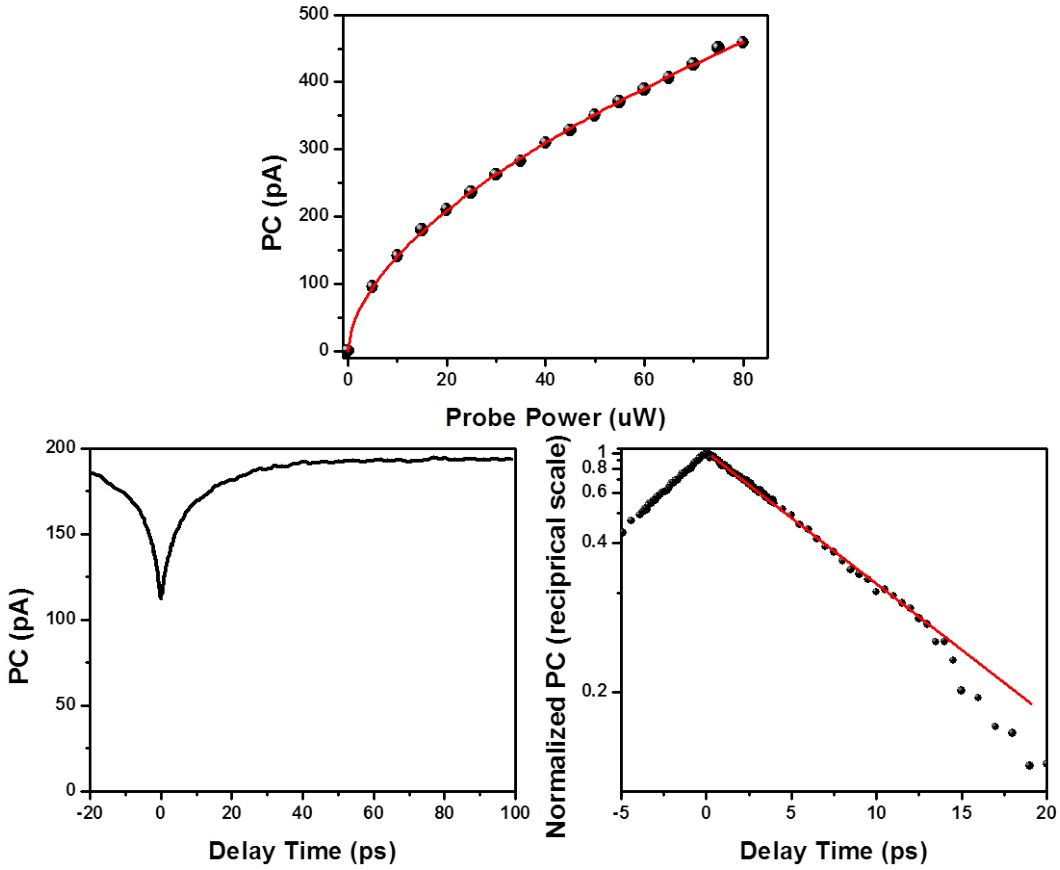

Figure 5.10: Pulsed excitation of photocurrent in single layer graphene. Top: saturation of photocurrent with the incident power of a single excitation pulse. Measured photocurrent fits well to a power law of $P^{0.6}$. Left: pump probe photocurrent time series with pump and probe powers of 20 μW. At long time delay pulses do not interact and the resulting photocurrent is the value expected from the probe pulse alone. At zero delay the two pulses are exciting with a combined power of 40 μW, which from the top plot gives $\sim$320 pA, though $\sim$200pA are generated by the pump pulse, leaving the remaining 120 pA excited by the probe pulse, as measured. Right: normalized time series plotted on a reciprocal scale. The time dependence of the saturation shows a clear 1/t dependence, with the red line as a guide for the eye.

Ref [75, 21]. In general the cooling time was found to be constant with respects to sample doping, and decreased with increasing temperature and laser power. In all cases, though, the cooling time was found to be on the order of several picoseconds.

5.3.2 Hot Carriers

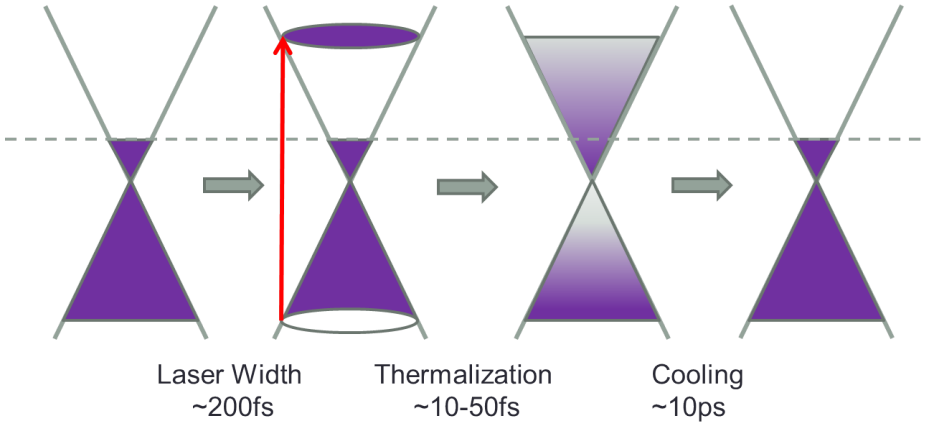

Figure 5.11: Schematic of pulsed photo-excitation in single layer graphene with corresponding time scales. First panel: Initial, cold thermal distribution of carriers in graphene. Second: optical excitation of non-equilibrium carriers. Third: Thermalization of carriers to an elevated temperature. Fourth: Cooling of hot carriers to initial state.

For pulsed excitation the process of photoexcitation can be described as in Figure 5.11, see Ref [3, 74, 76, 77, 79, 81] for more details. Before optical excitation, first panel, carriers in graphene behave as a degenerate Fermi gas with a temperature $T_{lattice}$ (10K). Electrons (dark blue) fill all states below the Fermi energy. Upon excitation, second panel, a non equilibrium distribution of electrons (holes) is created in the conduction (valence) band at an energy of half the optical excitation energy. Very quickly, timescales of 10s-100s of fs, carrier-carrier collisions thermalize the photo-excited carriers to a temperature $T_{carriers} \gg T_{lattice}$, decoupling the hot carriers from the cold lattice. It is a this point that the slow electron-phonon coupling described in section 5.1.2 comes into play. As the hot carriers begin to cool down they quickly become low enough energy that scattering off the high energy optical

phonons becomes impossible. It is then left to the very low energy acoustic phonons to cool to still hot carriers which is an extremely slow process (100's of ps), which is at odds with the measured cooling times from the previous section.

5.3.3 Supercollision Cooling

Clearly the limited phonon phase space available for electrons to scatter from should provide a substantial bottleneck for hot-electron cooling in graphene, theoretically resulting in cooling times on the order of 100's of ps. Experimentally, however, cooling times are much shorter, indicating there must be a faster, competing mechanism for electron-phonon scattering. This theory, developed in Ref [70], describes a three particle "supercollision" which opens up the available phonon phase space allowing for faster hot-carrier cooling.

The source of the electron-phonon bottleneck is the necessity of an electron to scatter from one side of the Dirac cone to the other— a relatively small change in momentum, q. This requirement for small q phonons restricts the available phonons eligible to scatter with electrons to only very low energy acoustic phonons. Therefore to cool down several hundred meV after optical excitation requires scattering of many such phonons, and raising the temperature has little effect since the higher energy phonons have too high of energy for scattering. The competing process makes use of the relatively high disorder in these monolayer crystals (due to residues from fabrication or the surface roughness of the SiO_2 substrate) as local momentum sinks. An impurity atom can act as a third body in an electron phonon collision and can absorb any residual momentum from the phonon that the electron is not capable of taking. In this way the full spectrum of phonons may be used in the scattering process. Obviously the three-body process has a reduced rate compared to the simple two-body one; however, the available phonon phase space is now vastly increased and the energy dissipated per collision is similarly enhanced (now of the order $\sim$kT).

The key premise behind this theory is that the energy loss power goes as the cube of the temperature, *i.e.*

$$\Gamma = A(T_{carrier}^3 - T_{lattice}^3) \tag{5.4}$$

This pathway was an enhancement factor over the traditional two particle acoustic phonon cooling pathway ($\Gamma_0 = A(T_{carriers} - T_{lattice})$) of as much as 100 times [70]. The scaling factor, A, is sensitive on the disorder, scaling linearly with the disorder ($1/k_f l$) which agrees with the experimental results reported in Ref [14]. For an electron density $Q = C\Delta T = (\alpha/2)T_{carrier}^2$, the electron cooling dynamics follow

$$\frac{dQ}{dt} = -\Gamma - \Gamma_0 \tag{5.5}$$

Combining equations 5.4 and 5.5 under the condition that $\Gamma \gg \Gamma_0$, the dynamics of the hot-carrier temperature can be found to be

$$T_{carrier}(t) = \frac{T_{carrier,0}}{1 + (A/\alpha)(t - t_0)T_{carrier,0}} \tag{5.6}$$

Recently several experiments have lent support to this theory. In Ref [21] the profile of hot-carrier cooling, as measured by pump-probe photocurrent, is found to agree well with the $1/t$ dependence predicted by the supercollision model (equation 5.6), see Figure 5.12, instead of an exponential time dependence as would be expected in the two particle process. Indeed, once a few experimental constants are determined, a parameter free fit to the temperature dependent cooling profiles shows remarkable agreement between the model and the data. Additionally a second group [2] was able to use noise thermometry to measure the T^3 dependence from equation 5.4.

The next couple chapters explore how this supercollision mechanism holds up in the case of a band structure broken by a band gap or Landau levels by looking at the functional form of $T_{carrier}(t)$ through pump probe photocurrent.

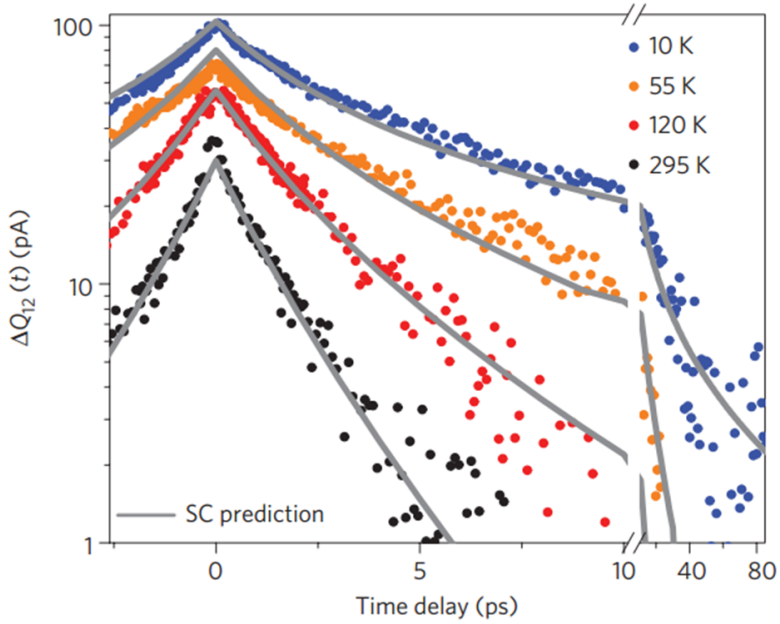

Figure 5.12: Hot-carrier cooling rates as a function of the lattice temperature. Solid lines are parameter-free fits to the data points using the supercollision model. Clearly the time depenence has a complicated structure in both delay time and temperature that is being captured extremely well in the model. Figure taken from Ref [21].

Chapter 6

PHOTOCURRENT GENERATION IN BILAYER GRAPHENE WITH VARIABLE BAND GAP

AB stacked bilayer graphene is composed of two sheets of single layer graphene stacked on top of each other, with the top layer 180^o rotated from the first. In this configuration inversion symmetry remains intact and bilayer graphene behaves as a gapless semi-metal similar to single layer graphene, see Figure 6.1, with the exception of it parabolic bands leading to massive Dirac fermions [51, 102]. However, applying a perpendicular electric field breaks the inversion symmetry and opens up a small band gap that is tunable from zero to several hundred meV with the applied field [47, 48]. In this chapter the optoelectronic properties of bilayer graphene are explored as a function of this opened gap.

6.1 Gate Tunable Band Gap

As seen in Figure 6.1, unperturbed AB stack bilayer graphene maintains its inversion symmetry and thus has no band gap. However when a strong electric field is applied perpendicular the the plane of the graphene the electron cloud is altered between the two layers and inversion symmetry is broken. At this point a small band gap is created that is tunable with the applied field [42, 47, 48, 105].

Experimentally this can be achieved with a dual gated bilayer graphene devices similar to the one shown in Figure 5.3. The top gate dielectric is created by transferring a thin ($\sim$ 5-10 nm) sheet of BN on top of the bilayer graphene and a gate electrode is fabricated out of the transparent conductor indium tin oxide (ITO) so that the dual gated region is optically accessible. The use of two gates allows control of both the doping, through the capacitive coupling described in section 5.1, as well as the opening of the band gap *solely* in the region controlled (underneath) the top gate.

For a given voltage on the top/bottom gate, V_i (i=TG,BG), the electric displacement field seen at the device is $D_i = c_i V_i$, where $c_i = \epsilon_i / d_i$ is the capacitance per unit area for

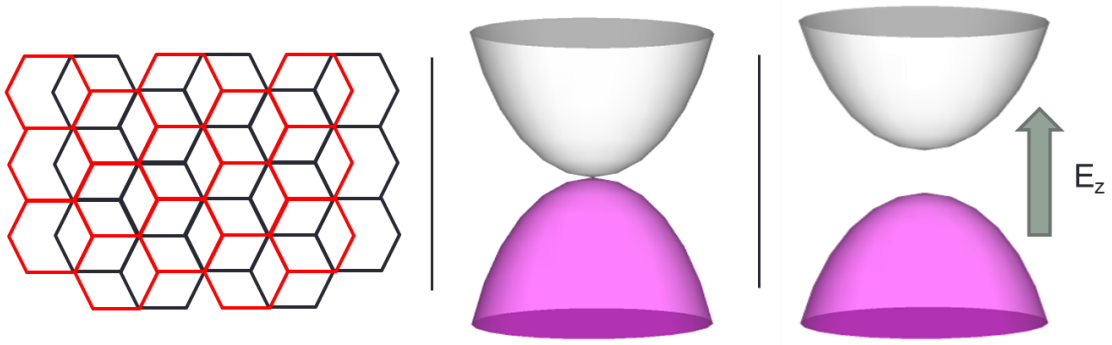

Figure 6.1: Right: schematic of stacking of graphene sheets in AB bilayer graphene shows the presence of inversion symmetry. Center: unperturbed, bilayer graphene's band structure shows parabolic bands meeting a single point, the Dirac point. However when an electric field perpendicular to the plane of graphene is applied, right panel, inversion symmetry is broken and a gap is opened.

the top/bottom gate dielectric. The total field at the device is the sum of these two fields, which can be combined in two ways to either dope the sample or to open up a band gap [105].

$$D_{dope} = D_{BG} - D_{TG} \tag{6.1}$$

$$D_{gap} = \frac{D_{BG} + D_{TG}}{2} \tag{6.2}$$

6.1.1 Infrared Detection of Band Gap

In Ref [105] infrared absorption is used to probe the band gap in a similar dual gated bilayer graphene. When a strong D_{gap} field is applied a peak in the absorption is seen at a the band gap energy, and a reduction in the absorption is seen below this band gap level. The experimentally measured gaps are compared with theoretical models and found to agree well with a self consistent tight binding model [102]. The results are shown in Figure 6.2.

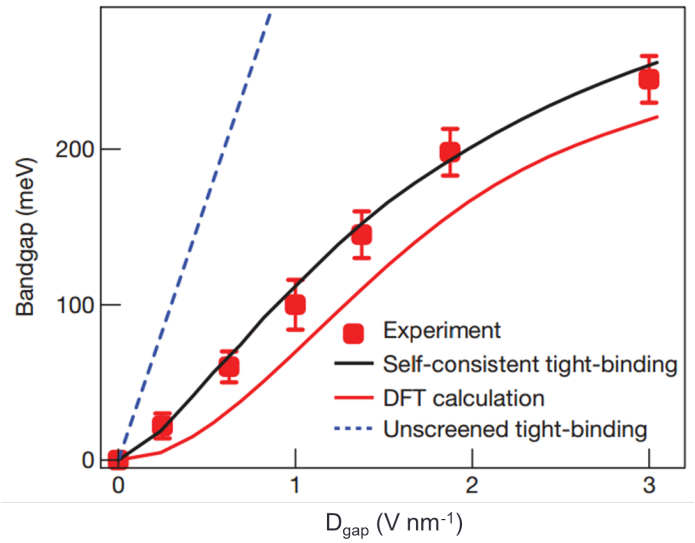

Figure 6.2: Observed band gap as a function of the applied perpendicular electric field D_{gap} measured by infrared absorption (red squares). Results match up well with the self-consistent tight-binding model described in Ref [102]. Image taken from Ref [105].

6.1.2 Resistive Measurement of Band Gap

Obviously the presence of a band gap will lead to an increase in the resistivity of a material than one without a band gap, so a resistance measurement can be an easy way to confirm the presence of a field induced gap in a bilayer graphene device. Figure 6.3 shows a two dimensional map of the resistance as the dual gates are both swept. The horizontal and vertical axes have been transformed into the two relevant electric displacement fields from 6.1 and 6.2. Immediately obvious is the saddle point in the middle corresponding to the zero applied field condition. In this case the device is neutrally doped and the gap is closed. Moving vertically the field induces a widening of the band gap and the resistance rises dramatically as the gap inhibits conduction of carriers. Moving right (left) causes an increases in the sample doping, or the Fermi level, which quickly overcomes the gap and fills electrons (holes) in the conduction (valence band) resulting in a decrease in the resistivity.

In this sample the gap is clearly opened, but estimating the gap size is difficult from this measurement alone. By comparing the maximum applied D_{gap} field to Figure 6.2 the

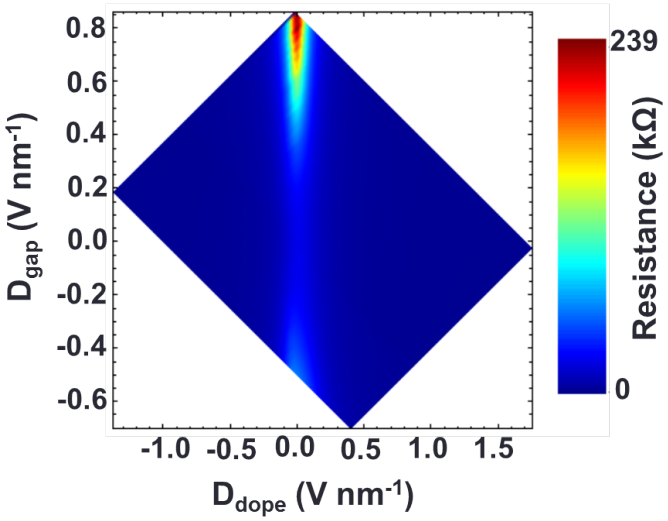

Figure 6.3: 2D map of the electrical resistance of the dual gate bilayer graphene device as a function of the applied electric fields D_{dope} and D_{gap}. Saddle point in the middle is the zero field point, resistance grows quickly vertically as a gap is opened and drops off quickly left/right as the sample is doped.

maximum band gap can be estimated to be ∼100 meV. This gap is much smaller than the laser energies used in the experiments (∼1.65 eV), so there should be little effect on the absorption of radiation. However, it is much larger than thermal energy ($k_BT \approx 2$ meV) and the available acoustic phonons. It would then be expected that this gap would have significant ramifications on the cooling of carriers after excitation.

6.2 Spatially Resolved PC

Scanning PC microscopy images were taken of the dual gated bilayer graphene device to determine the spatial profiles of the photo-active regions once the band gap is opened. Again, with the use of two gate the band gap and the doping can be independently controlled only in the region underneath the top gate. Outside of this area, effectively D_{TG} is zero in equations 6.1 and 6.2 meaning that as the global back gate is tuned, the doping and the band gap are both changed. So outside of the top-gated region there is less control on

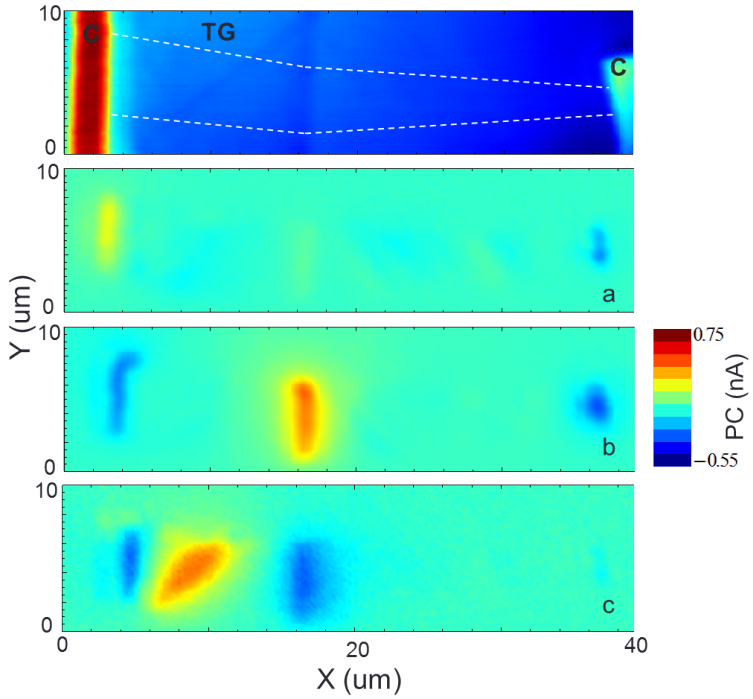

Figure 6.4: Scanning PC images of the dual gated bilayer graphene device. Top: reflected laser image of the device, showing the contacts ("C"), top gate ("TG), and graphene channel (while dashed line). Below are corresponding photocurrent maps for different gate configurations.

these knobs. Still by tuning the gates appropriately a PN junction can be formed at the edges of the top-gated region and Schottkey junctions can be formed at the graphene/metal junctions. Now, unlike for single layer graphene, these interfaces are between materials with a band gap.

In Figure 6.4 the scanning PC microscopy images are plotted for several different gate configurations. The top image shows the reflected laser map of the device, clearly showing the two contacts and the top gated region on the left. The graphene channel is highlighted in the white line. Below are the PC maps, that show the gate tunability of the graphene/metal contact hotspots, the PN junctions, and an anomalous spot directly underneath the top gate. This final map is set at low doping and large band gap strength in the top gated region.

6.3 Gap Enhanced Photoresponse

To investigate the dependence of the gate voltages on the photo-response the laser is fixed on the PN junction while the gates are swept, see Figure 6.5. In this case since the region not under the top gate does not have independent control of its band gap and doping there is not good basis to plot the axes in, so they are left in terms of their gate voltages. In this case the opening of the band gap in the top gated region is on the major negative diagonal, while a pure doping of the top gated region is on a positive diagonal.

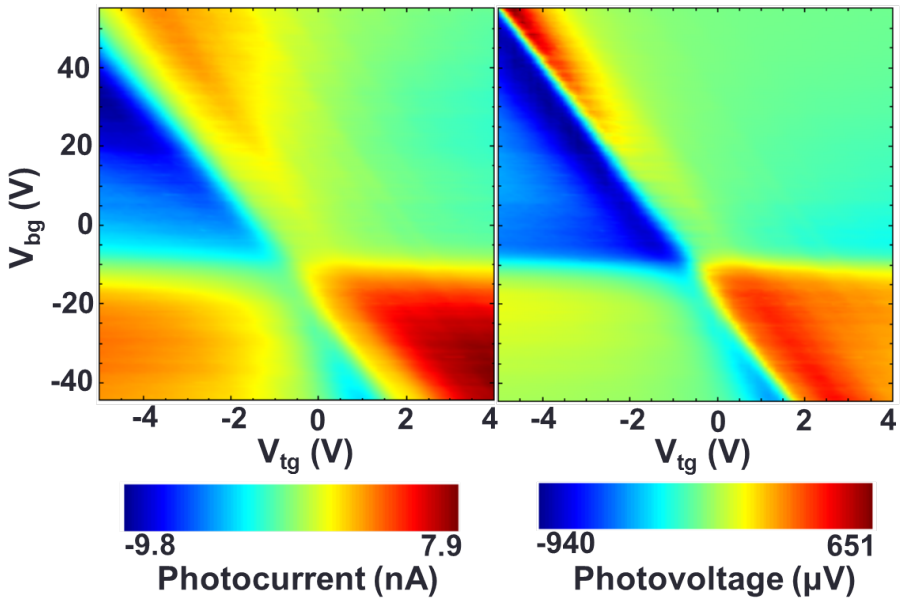

Figure 6.5: Photo-response of PN junction in bilayer graphene FET as a function of the top and bottom gate voltages. Left: photocurrent map shows the typical 6-fold pattern indicating PC is dominated by hot carriers. Right: photovoltage map shows strong enhancement of the response along the diagonal line, corresponding to the opening of the band gap.

In the left map the PC of the PN junction is plotted. Clearly it shows the signature 6-fold pattern discussed in Section 5.2, indicating that here, too, hot carriers dominated the PC response [17, 69]. What is interesting, though, is that along the main negative diagonal, the generated PC is nearly constant, while this is where the resistance is increasing exponentially

due to the opening of the band gap. To illustrate this further the photovoltage (PV=PC*R) is calculated and plotted in the right panel. The PV along the main negative diagonal shows a very strong enhancement due to the opening of the band gap.

Several papers have discussed the increased thermopower of bilayer graphene when the gap is opened [24, 29, 83], so this gap enhancement of the PV should be expected.

6.4 Hot-Carrier Cooling with Opened Gap

Finally the hot-carrier cooling time can be measured using the pump probe photocurrent method described in section 5.3. A time series taken from the top-gated region under zero applied electric fields is shown in the left panel of Figure 6.6. This curve has a very similar shape to those from single layer graphene with a flat tail at long time delay when the pulses are not interacting and a substantial dip near zero time delay corresponding to saturation in the probe induced photocurrent. The width of the dip is slightly larger than the single layer case, corresponding to a hot-carrier cooling time closer to 10ps. While this is longer than that measured in monolayers it is still much less than the theoretical cooling times ($\sim$100 ps) predicted from models using only two particle electron/phonon cooling.

The most striking difference however is the profile of the dip. In the right panel of Figure 6.6 the normalized time series is plotted on a logarithmic scale. Clearly this follows an exponential decay in contrast to the $1/t$ dependence predicted by the supercollision model [21, 70], see section 5.3. This hints that in bilayer graphene, with its different electron dispersion, that the supercollision mechanism is no longer the dominant cooling process. Indeed the wider electronic dispersion created by the parabolic bands may be less restrictive for the simpler two-body scattering mechanism for cooling. More work needs to be done to investigate this possible mechanism.

The previous data was taken without any applied fields to dope the sample or open up the band gap. It is found that when the gate voltages are turned on the time series maintain their exponential behavior, so hot-carrier cooling times can easily be extracted as the time constant of an exponential fit to the $t > 0$ data.

In Figure 6.7 the sample is held at zero doping ($D_{dope} = 0$ V/nm) while the band gap field (D_{gap}) is swept from zero upward. The left panel shows the extracted hot-carrier

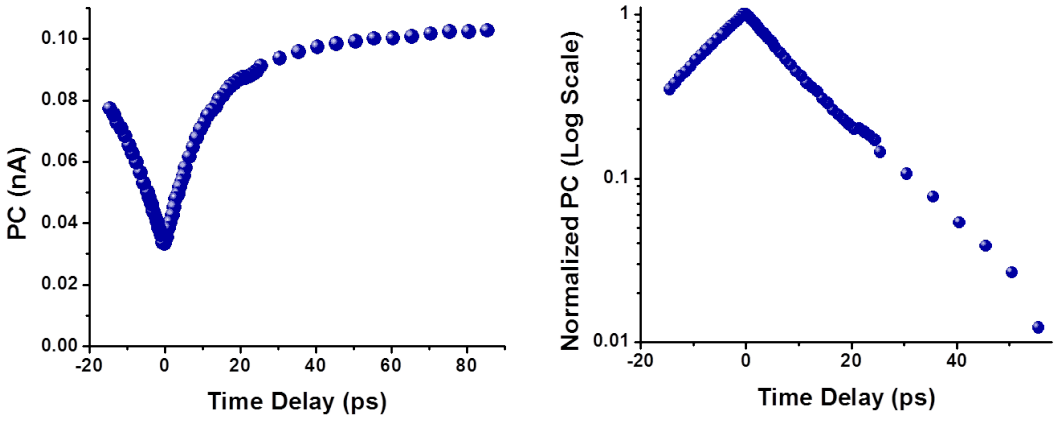

Figure 6.6: Pump probe photocurrent time series for unperturbed bilayer graphene. Left: time series shows similar dip as for the single layer case, timescale of approximately 10ps is slightly longer. Right: normalized time series on a logarithmic scale shows a clear exponential dependence in contrast to the supercollision model, see equation 5.6.

cooling times which show a definitive, though not drastic, linear increase with the applied field. The right panel shows several normalized time series with increasing field strength plotted on a logarithmic scale. Clearly the curves maintain their exponential character and the slope gets steadily shallower with increasing field.

From Figure 6.2 the band gap magnitude is roughly proportional to the applied electric displacement field, D_{gap}, for fields less than $\sim$2 V/nm, as is the case here. Therefore, the cooling time is found to be roughly proportional to the gap size, $\tau \propto \Delta_{gap}$, for small gaps. This is expected as the opening of the gap provides a barrier holding apart the photo-excited electron/hole pairs. The linear dependence may provide insight into the mechanism through which the carriers are able to recombine across the gap.

A cut of constant band gap is taken in Figure 6.8. The gap field is held at $D_{gap} = 0.5$ V/nm while the doping field, D_{dope}, is swept from hole to electron doping. The hot-carrier cooling time, τ, is extracted and shows no dependence on the doping. The hole in the data near $D_{dope} = 0$ V/nm is due to the fact that the single pulse photocurrent crosses sign there.

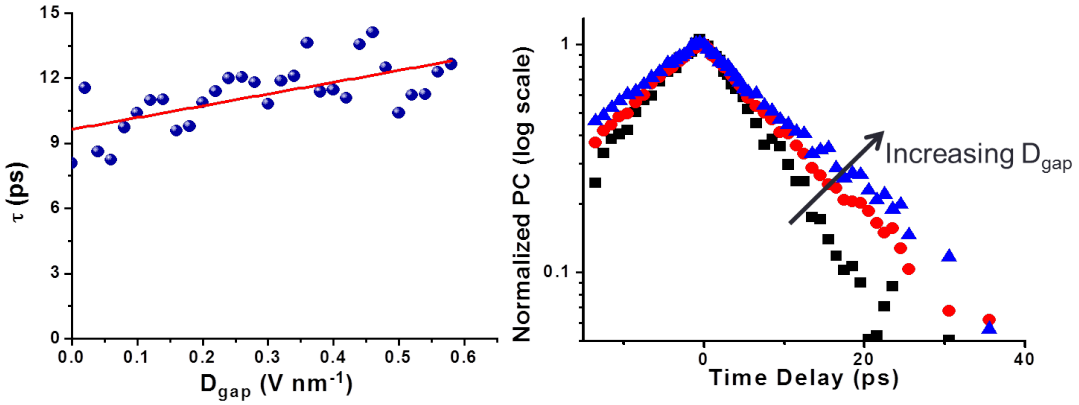

Figure 6.7: Hot-carrier cooling times as a function of the band gap inducing displacement field D_{gap}. Left: extracted exponential cooling times as a function of the applied field shows a clear linear increase. Right: several representative time series normalized and plotted on a logarithmic scale again show the exponential dependence and the definitive increase in the cooling times with the band gap. Sample is held at neutral doping, $D_{dope} = 0$ V/nm.

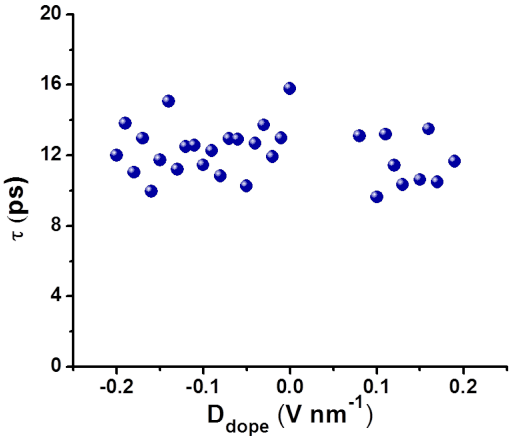

Figure 6.8: Hot-carrier cooling times as a function of the sample doping displacement field D_{dope}. The data shows no clear dependence. Missing data points in the middle correspond to a zero crossing in the single pulse photocurrent making the signal unreliable. $D_{gap} = 0.5$ V/nm.

6.5 Outlook and Future Work

In general, there are few exemplary optoelectronic materials in the far IR. Bilayer graphene, with its tunable band gap, could serve an important niche as a photodetector in these low energy regimes [29, 97], but first its optoelectronic properties must be investigated. This work has demonstrated an enhancement of the photo-voltage with the opening of a band gap through the increased Seebeck coefficient under these conditions. Additionally it shows the tunability of the device response time, as indicated by the hot-carrier cooling times, by changing the band gap. For a high speed photodetector [50, 82] once the carriers are excited they need to be quickly converted to a current and exit the device before the next bit of light can be absorbed. Faster hot-carrier cooling times allow this reset time between information bits to be shorter, increasing the detector bandwidth. Luckily, as this measurement shows, the response time as the gap is opened up does not change dramatically, indicating that a potential device could still operate very quickly even when working with an open band gap to increase the photoresponse.

Work still needs to be done to investigate the amplified photo-voltage produced when the gap is opened up, specifically the development of a concise theory to explain this phenomena. Additionally the hot-carrier cooling times where found to have a time dependence at odds with the current supercollision cooling model applicable to monolayer graphene. New theory must be developed to explain the cooling of hot carriers in this material, including the linear dependence of cooling time on the band gap, so that future devices may be optimized.

One potential device architecture that may be of particular interest would be a bilayer graphene FET with the bottom and top gates split into two. This would provide two regions where the doping and band gap could be completely, and independently, controlled. At their interface an inhomogeneous pn-junction could be formed, with a tunable band gap on either side. This architecture would allow for complete investigation of the band gap effects on the photoresponse and would be an important architecture for a far-IR detector. However, it is a complicated structure and much would would need to be done to optimize it.

Chapter 7

PHOTOCURRENT GENERATION UNDER LANDAU LEVEL QUANTIZATION IN SINGLE LAYER GRAPHENE

In two-dimensional systems in a large out of plane magnetic field the resulting electronic cyclotron orbits leads to a quantization of the Hall conductivity known as the quantum Hall effect (QHE). The continuous band structure is condensed into highly degenerate, discrete Landau levels. In graphene, with its exceptionally large cyclotron gap [23], this effect is especially pronounced allowing the quantization to occur at lower magnetic fields and higher temperatures– even having been reported at room temperature [56]. The aim of this chapter is to investigate the effect of this discretization of the band structure on the optoelectronic properties of graphene.

7.1 Quantum Hall Effect in Graphene

The QHE was discovered in 1980 in the seminal paper by von Klitzing [31] which would eventually lead to a Nobel prize. The theory was then quickly worked out by Laughlin [34]. Upon application of a magnetic field perpendicular to the plane of a 2D electronic system, the electrons will begin to precess in cyclotron obits with frequency ω_c. When treated quantum mechanically these orbits become quantized, occupying only certain orbits with discrete energies, known as Landau levels (LLs). In a standard 2D system the energy spectrum behaves identically to a quantum harmonic oscillator with energy levels

$$E_{QHE} = \hbar\omega_c(n + 1/2) = \frac{\hbar e}{mc}B(n + 1/2) \tag{7.1}$$

for integer values of n, corresponding the the Landau level index, and B the magnetic field strength. The levels are equally spaced and there is no zero energy Landau level. As the magnetic field strength is increased the spacing increases forming a fan.

The electron cyclotron orbits are shown schematically in Figure 7.1. In the interior the electrons follow closed cyclotron orbits (red curves), locking the electrons in their present

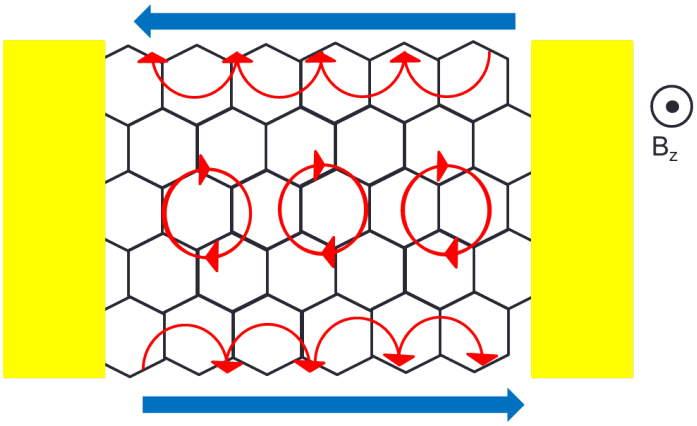

Figure 7.1: Schematic depicts electron cyclotron orbits (red) in a graphene device in an out of plane magnetic field. In the interior electrons orbits are closed resulting in no net current; however, on the edges the orbits do not close on themselves due to scattering from the edges, resulting in a net drift of carriers. This drift generates an edge current that is canceled out by a similar current on the opposite edge.

position. At the edges the electrons are unable to form a closed orbit due to scatter from the edges themselves. The combination of edge scattering with the cyclotron orbit results in a net drift of electrons generating an edge current depicted by the blue arrows. This effect is opposite on opposite edges, and switches polarity with the magnetic field. Each Landau level carriers a conductivity quanta, e^2/h, in these edge states, so by changing the Fermi energy to include more Landau levels the edge conductivity increases by ne^2/h. This quantization is extremely precise, even in repetitively dirty condensed matter systems [31], such that this effect leads to the current precision Ohm standard. It is important to note that these edge currents flow even in the absence of an applied electrical bias; however, since the two edges contribute equal and opposite currents there is no net current flow in a device without some other symmetry breaking process.

Each LL is highly degenerate, with occupation numbers related to the ratio of the physical sample size times the mangetic field strength to the magnetic flux quantum. When the field is strong enough that all of the free carriers are concentrated in only a few Lan-

dau levels, the QHE effect is observed. It is characterized by a quantization in the Hall conductivity in units of e^2/h that steps with increasing sample doping or magnetic field; corresponding to the change in the number of occupied Landau levels. Additionally the longitudinal, magneto-resistance shows dips as new Landau levels are filled due to the extra edge channels.

Graphene, due to its unique massless dispersion and nonzero Berry phase, has an anomalous QHE theorized by Gusynin and Sharapov [23] in 2005 and quickly demonstrated [53, 104] with the isolation of monolayer graphene, eventually leading to a Nobel prize for Novoselov and Geim. Instead of the linear spaced quantum harmonic oscillator spectrum from equation 7.1, graphene's energy spectra is given by

$$E_{graphene} = \pm\sqrt{2e\hbar v_f^2 nB} \tag{7.2}$$

where again n is the Landau level index (positive integer values), B is the magnetic field strength, and v_f is the Fermi velocity of graphene ($\sim 1{*}10^6$ m/s). This anomalous nonlinear spectra in n is due to the linear dispersion of graphene. Additionally this spectra allows

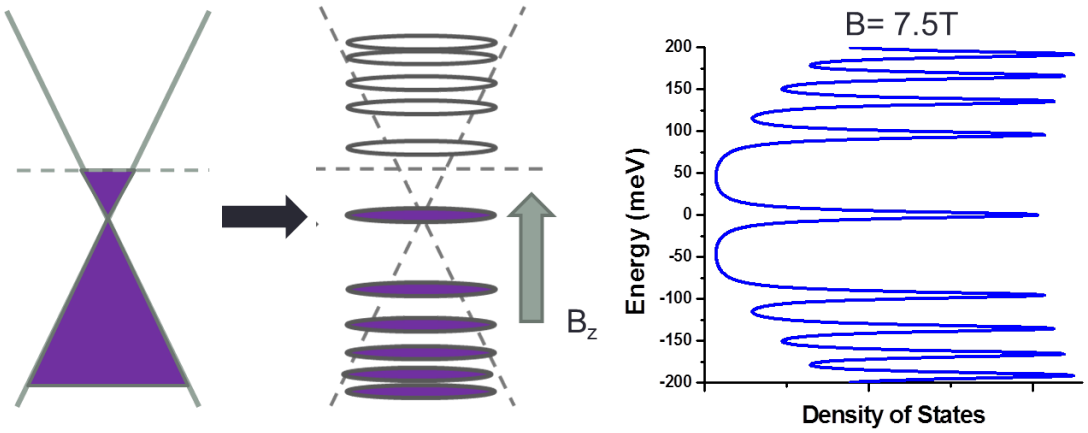

Figure 7.2: Upon application of a perpendicular magnetic field graphene's continuous band structure (left) breaks down into highly degenerate, discrete Landau levels (middle). In graphene these Landau levels have a nonlinear energy spacing and as well as a zero energy level. Right: simulated density of states for graphene Landau levels at B= 7.5T.

for a zero energy Landau level unlike in conventional semiconductors. This spectrum is shown schematically in Figure 7.2, showing the zero energy Landau level at the Dirac point, and the bunching of Landau level at higher carrier energies. As a function of magnetic fields these will space out even further, scaling with $\sqrt{B}$. The width of a Landau level is approximated as $\Gamma \approx \hbar/\tau$ where τ is the scattering time of the particles. Higher mobility samples have a longer τ, thus narrower Landau levels, and therefore the QHE effect can be seen at smaller field strengths.

This square root dependence on both the field and the Landau level index have been investigated using infrared spectroscopies in References [27, 64].

Due to the four-fold (two spin and two valley) degeneracy of carriers in graphene each Landau level adds $4e^2/h$ to the conductivity when filled. However, the zero energy Landau level contributes only half of these quantum when filled, contributing half its quanta to electron and half to hole conductivity. Therefore the conductivity is quantized in units of

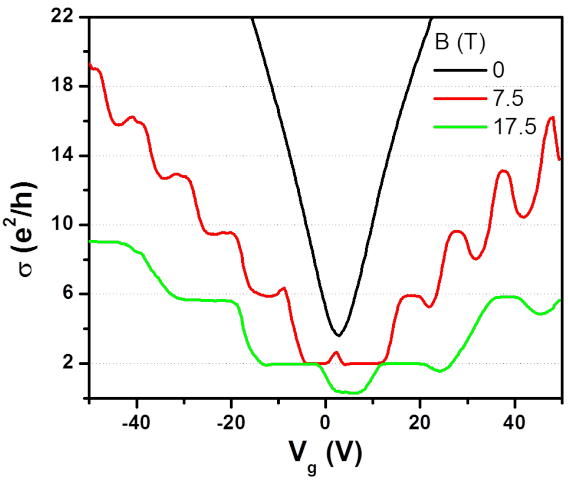

Figure 7.3: Two terminal conductivity of a graphene FET for various magnetic fields showing the formation Laundau levels. As the field is increased the conductivity forms plateaus at values of 2, 6, 10,... e^2/h, indicating the addition of an extra Landau level to the conductivity.

$4(n+1/2)e^2/h$, forming plateaus of conductivity then at 2, 6, 10, ... e^2/h. Figure 7.3 shows the two-terminal conductance of a graphene FET for various magnetic fields. At zero field (black) the curve shows a smooth dip characteristic of the Dirac point. However, once a large field is turned on, quantized steps begin to appear at the conductivity quanta. These plateaus become increasingly wide and more spaces out as the field is further increased.

The four-fold degeneracy can be broken by further increasing the magnetic field or the sample quality to the point where full integer quantization occurs, effectively Zeeman splitting the spin and valley degeneracy [103]. Finally with an even further increase in field or quality extra plateaus with non-integer multiples of e^2/h begin to appear, primarily n=1/3, known as the fractional quantum hall effect [4, 15, 26]. This effect is much more complicated, but stems from carrier interactions.

Graphene's unique quantum Hall behavior is explored more fully in the review of Ref [20].

7.2 National High Magnetic Field Lab

To reach magnetic field strength large enough to sufficiently form Landau levels, this work is done at the National High Magnetic Field Lab, in Tallahassee. There a 17.5T superconducting magnet has been built around a two inch bore with an optical window. The sample is loaded onto a 12 foot long probe which is lowered into the liquid helium magnet and cooled with a helium exchange gas to 4K. The sample sits, upside down, at the bottom of the probe. The magnet is suspended off the ground with the optics window underneath, allowing laser excitation in free space onto the sample from below.

Alignment of the system is especially challenging as the sample is located several feet inside the bore of the magnet and the last alignment mirror is outside. To allow for precise focusing of the pump and probe laser beams onto the small exfoliated sample area, a special sample mount was developed. Three Attocube nanopositioners are used to move the sample around and precisely focus it. A low-temperature compatible microscope objective is attached to the sample mount as well to allow for tight focusing.

The system must be first optically aligned without the sample probe, making sure the laser light passes all the way through the center of the bore of the magnet. The sample is positioned and focused at room temperature on the optics table in the probe sample

mount. At which point the whole probe may then be carefully inserted into the magnet, maintaining the sample and objectives orientation in the center of the bore. Finally the optics can be slightly realigned to center the laser light onto the microscope objective to create the most tightly focused beam. A white-light microscope is also built in conjunction with the pump probe photocurrent setup to help locate the sample and precisely position the focused beams.

All in all the system allows for a 1-2 μm focused spot for a pump and probe beam at 1.55 eV, precise (sub 50 nm) position of the sample in 3D, detection of photocurrents below 10 pA, and the ability to measure the ultrafast hot-carrier cooling times through the pump probe photocurrent method, all at 4K in a bipolar field of amplitudes up to 17.5T.

7.3 Photocurrents in QHE Regime

To separate the photocurrents generated due to the QHE from other currents like those measured in the previous two chapters, the excitation laser is focused on the edge of the graphene device, well away from either contact. One contact is grounded, and the photo-excited current is detected at the other contact using a lockin amplifier at the probe modulation frequency. It is important to note that no electrical bias is applied in this measurement, and the currents arise solely from the QHE edge currents depicted in Figure 7.1. Previous studies have explored the spatial nature of these edge currents [52].

The gate dependent PC collected at one of edges for various magnetic fields is shown in Figure 7.4. At zero applied field (black line) the current is zero as would be expected. When the field is turned on, however, the QHE effect sets up the DC edge currents, which by themselves result in no net current since there is an equal but opposite current on either edge. However, the laser is exciting only one edge, and therefore the left/right symmetry is broken and a net current flows along one edge as shown in the red and green curves with the field applied. In both cases the field only has one sign as a function of the gate voltage, decided by the magnetic field generated edge current. The sign of the PC changes when the other edge is excited or when the magnetic field is switched in polarity.

The other dominant feature of this PC is that it is periodic in the gate voltage, just like the conductivity. In fact, by looking at the dominant frequency of the FFT of the PC signal

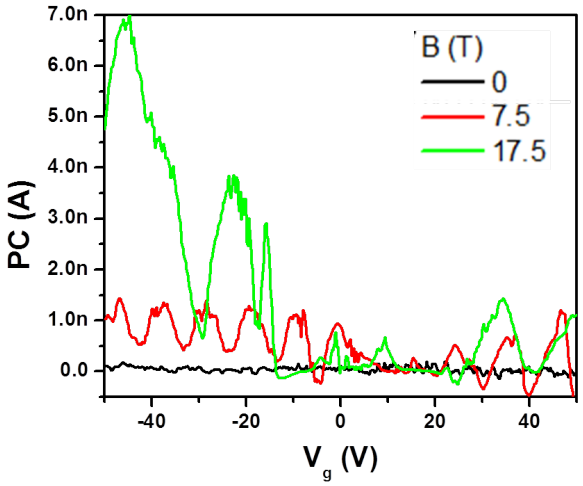

Figure 7.4: Photocurrent generated at the edge of a graphene device for various magnetic fields. No current is generated without applying a field (black). Under high field the current is oscillatory and also predominantly of a single sign.

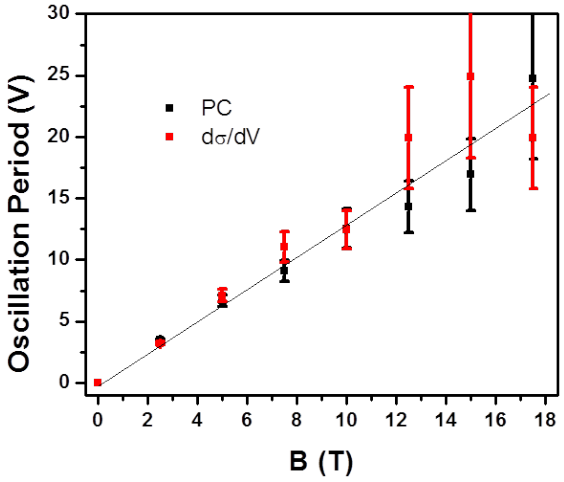

Figure 7.5: Period of oscillation of the edge photocurrent (black) and the differential conductance (red) with back gate voltage. Periods determined by FFT of data in Figures 7.3 and 7.4, error bars are from FFT resolution. Linear relationship with B confirms Landau level origin. Line is best linear fit with slope 1.26 volts/tesla.

from Figure 7.4 and the same from the differential conductance ($d\sigma/dV_g$) from Figure 7.3, they share the same linear relationship with B (see Figure 7.5). The energy spectrum of the Landau levels is given by equation 7.2 while the change in the Fermi level with gate is given by $E = \hbar v_f \sqrt{\pi c_g V_G / e}$ (from Section 5.2). Combining these two gives

$$\frac{\Delta V_G}{\Delta n} = \frac{2e^2}{\hbar \pi C_g} B = 1.35 B(volts) \tag{7.3}$$

Which agrees very well with the fitted slope from Figure 7.5 of 1.26±0.05 V/T, confirming the fact that both of these oscillations stem from the underlying Landau level physics.

7.4 Hot-Carrier Cooling in QHE Regime

It was shown in the previous section the the breaking of the band structure into discrete Landau levels has profound impacts on the excited edge photocurrent. Naively one would also think that it would cause photoexcited hot carriers to cool more slowly, as shown in Figure 7.6, and has been reported previously [57]. Whereas in unperturbed graphene, hot carriers could relax through collisions with available phonons of any energy (with momentum conservation being the only limiting factor), now with the allowed electronic states condensed into a few Landau levels, only a small subset of the total phonons can scatter

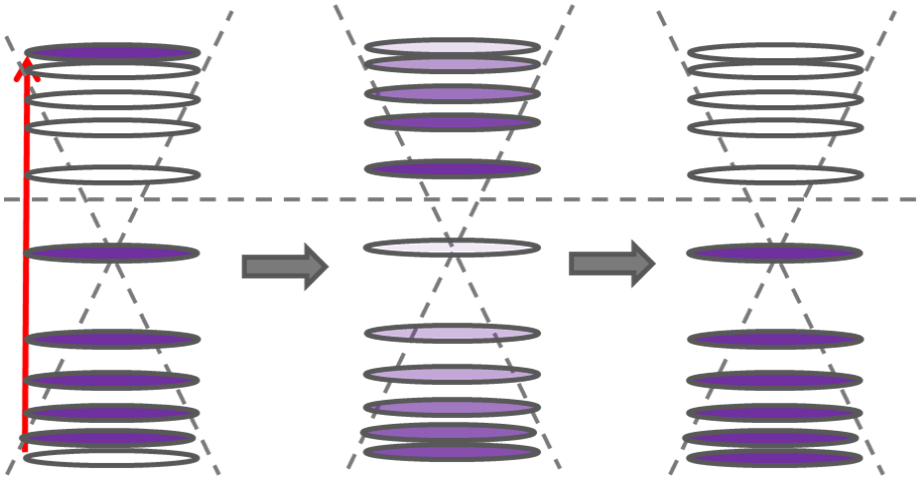

Figure 7.6: Hot-electron cooling is affected by the discretization of graphene's band structure in the QHE regime.

between these Landau level states. This may cause the process to take longer. It would also be expected that if there were fewer Landau levels below the excitation energy (the case for high field) this would take even longer as the Landau level spectrum creates an effective band gap. Additionally by tuning the Fermi level to fill or empty one of the low lying Landau level, the cooling should quicken or lengthen, respectively.

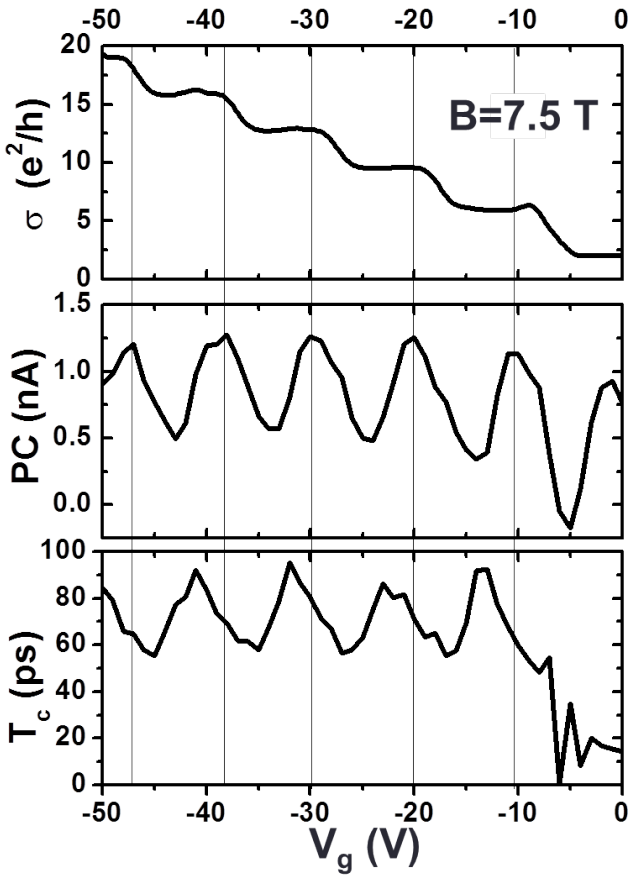

Figure 7.7: Photo-response of graphene under Landau level quantization. Top: longitudinal conductivity (σ_{xx}) versus gate shows Landau level steps. Middle: single pulse photocurrent versus gate oscillates with gate, peaking after the addition of each Landau level. Bottom: hot-carrier cooling time (HWHM) as a function of gate also oscillates, peaking in between Landau levels. B= 7.5T

To investigate this, photocurrent pump probe was performed on these edge currents in the high magnetic field, as shown in Figure 7.7 for B= 7.5T. On the top is the two-terminal conductivity as a function of the applied gate, from Figure 7.3. The middle is the similar oscillating single pusle photocurrent from Figure 7.4. And on the bottom is the hot-carrier cooling time extracted from a pump probe time series (similar to Figure 5.10). However, as the field is turned on the timeseries no longer conform to either an exponential nor a 1/t decay, so the cooling time is extracted as the half-width at half-max (HWHM) of the pump probe dip. Surprisingly, the cooling time as well shows an oscillatory nature, whereas one might it expect to look as a stair-step as the ground state is brought further/closer to the hot carriers.

Vertical lines are drawn through all three plots at the points where a Landau level has been filled (with holes in this case). At this point the conductivity reaches a plateau as the new edge state is allowed; the single pulse PC reaches a maximum; whereas the cooling time reaches its middle value. The cooling time, in fact, is the longest when the Fermi energy (the ground state of the hot-carrier cooling) is in between the Landau level, and its minimum when the Fermi energy has just reach, but not filled, a new Landau level. Also note that the cooling times are substantially longer than those measured in either single or bilayer graphene, $\sim$80 ps.

It would be interesting to investigate how this cooling time changes as a function of the Landau level spacing, by increasing the magnetic field. However, this is a much more difficult experiment. As can be seen in Figure 7.6, there is a large variation in the cooling depending on the relation between the Fermi energy and the Landau level energies. And since the Landau level energies change with the magnetic field, to get a good idea how the spacing plays a role in this the gate voltages need to be precisely set in the same location relative to the changing Landau levels for each new magnetic field. While technically challenging this experiment would provide the most concrete insights into how the Landau levels effect the hot-carrier cooling.

7.5 Outlook and Future Work

This work investigated the gate dependence of the optoelectronic properties of graphene's quantum hall edge currents at large magnetic fields. Both the PC and the hot-carrier cooling times showed periodic behavior that matched up with the Landau level periods, confirming the fact that it is the Landau levels that are dominating the optoelectronic properties of graphene even at optical energies much larger than the Landau level gaps. However, using PC as a probe for the inner electronic workings is complicated. The measurement integrates the electronic mechanisms not only over the hot-carrier lifetimes but also over the area of the device, in addition to being an inherently nonlinear effect. The results is that developing a model to explain the data can be very difficult. While results presented in this chapter look beautiful, much work needs to be done now to explain them and draw out the meaningful physics.

Measurements that are easier to interpret physically are usually much more complicated to perform. For instance to study the effects of hot-carrier cooling through the Landau levels a better measurement would be a non-degenerate pump probe spectroscopy experiment. A high energy probe could initially setup a hot-carrier distribution that would effect the absorption of all of the lower energy Landau levels. A lower energy probe pulse could investigate this change in absorption as a function of time and energy to discern how carriers are moving through the available states. A similar measurement was performed at THz excitation looking at Auger process between the n=0 and n=$\pm$1 LLs in Ref [49]. These nondegenerate measurements are tricky, involving multiple synchronized lasers. Also probing at the low Landau level energies involves using far-IR or THz sources which are very challenging to work with.

It is also important to remember that in the experiments performed in this chapter it is the ground state configuration that is swept with the gate voltage. The optical pulses are exciting carriers to a quasi-continuum, where the Landau level spacing is similar to the Landau level width, at which point they thermalize and start feeling the effects of the discretized band structure. By sweeping the gate voltage Landau levels are added or subtracted from the bottom of the spectrum through which the hot carriers must cool

through. A different experiment would involve fixing the gate voltage, setting the ground state configuration, and sweeping the excitation laser frequency to include more or fewer Landau levels in the cooling process. Again it is tricky working with optics at low enough energies such that the Landau level spacing is not quasi-continuous, especially sweeping the laser energy over such a large range in these long wavelength regimes.

All that being said, future optoelectronic devices will most likely operate in the conditions presented here: excitation into the quasi-continuum and control over the ground state configuration. So these experiments are probing the properties most relevant to those future applications, despite their relative complications in understanding.

BIBLIOGRAPHY

[1] G. Aivazian, Zhirui Gong, Aaron M. Jones, Rui-Lin Chu, J. Yan, D. G. Mandrus, Chuanwei Zhang, David Cobden, Wang Yao, and X. Xu. Magnetic control of valley pseudospin in monolayer WSe2. *Nature Physics*, 11(2):148–152, January 2015.

[2] A. C. Betz, S. H. Jhang, E. Pallecchi, R. Ferreira, G. Fève, J-M. Berroir, and B. Plaçais. Supercollision cooling in undoped graphene. *Nature Physics*, advance on, December 2012.

[3] R. Bistritzer and A. MacDonald. Electronic Cooling in Graphene. *Physical Review Letters*, 102(20):206410, May 2009.

[4] Kirill I Bolotin, Fereshte Ghahari, Michael D Shulman, Horst L Stormer, and Philip Kim. Observation of the fractional quantum Hall effect in graphene. *Nature*, 462(7270):196–9, November 2009.

[5] F Bonaccorso, Z Sun, T Hasan, and AC Ferrari. Graphene photonics and optoelectronics. *Nature Photonics*, pages 1–15, 2010.

[6] M. Breusing, S. Kuehn, T. Winzer, E. Malić, F. Milde, N. Severin, J. P. Rabe, C. Ropers, A. Knorr, and T. Elsaesser. Ultrafast nonequilibrium carrier dynamics in a single graphene layer. *Physical Review B*, 83(15):153410, April 2011.

[7] Ting Cao, Gang Wang, Wenpeng Han, Huiqi Ye, Chuanrui Zhu, Junren Shi, Qian Niu, Pingheng Tan, Enge Wang, Baoli Liu, and Ji Feng. Valley-selective circular dichroism of monolayer molybdenum disulphide. *Nature communications*, 3:887, January 2012.

[8] a. Castro Neto, F. Guinea, N. Peres, K. Novoselov, and a. Geim. The electronic properties of graphene. *Reviews of Modern Physics*, 81(1):109–162, January 2009.

[9] Tawinan Cheiwchanchamnangij and Walter R. L. Lambrecht. Quasiparticle band structure calculation of monolayer, bilayer, and bulk MoS2. *Physical Review B*, 85(20):205302, May 2012.

[10] Alexey Chernikov, Timothy C. Berkelbach, Heather M. Hill, Albert Rigosi, Yilei Li, Ozgur Burak Aslan, David R. Reichman, Mark S. Hybertsen, and Tony F. Heinz. Exciton Binding Energy and Nonhydrogenic Rydberg Series in Monolayer WS2. *Physical Review Letters*, 113(7):076802, August 2014.

[11] Rui-Lin Chu, Xiao Li, Sanfeng Wu, Qian Niu, Wang Yao, Xiaodong Xu, and Chuanwei Zhang. Valley-splitting and valley-dependent inter-Landau-level optical transitions in monolayer MoS2. *Physical Review B*, 90(4):045427, July 2014.

[12] DR Cooper and B D'Anjou. Experimental review of graphene. *arXiv preprint arXiv: ...*, 2011.

[13] Qiannan Cui, Frank Ceballos, Nardeep Kumar, and Hui Zhao. Transient absorption microscopy of monolayer and bulk WSe2. *ACS nano*, 8(3):2970–6, March 2014.

[14] Jahan M. Dawlaty, Shriram Shivaraman, Mvs Chandrashekhar, Farhan Rana, and Michael G. Spencer. Measurement of ultrafast carrier dynamics in epitaxial graphene. *Applied Physics Letters*, 92(4):042116, January 2008.

[15] C R Dean, L Wang, P Maher, C Forsythe, F Ghahari, Y Gao, J Katoch, M Ishigami, P Moon, M Koshino, T Taniguchi, K Watanabe, K L Shepard, J Hone, and P Kim. Hofstadter's butterfly and the fractal quantum Hall effect in moiré superlattices. *Nature*, 497(7451):598–602, May 2013.

[16] C R Dean, A F Young, I Meric, C Lee, L Wang, S Sorgenfrei, K Watanabe, T Taniguchi, P Kim, K L Shepard, and J Hone. Boron nitride substrates for high-quality graphene electronics. *Nature nanotechnology*, 5(10):722–6, October 2010.

[17] Nathaniel M Gabor, Justin C W Song, Qiong Ma, Nityan L Nair, Thiti Taychatanapat, Kenji Watanabe, Takashi Taniguchi, Leonid S Levitov, and Pablo Jarillo-Herrero. Hot carrier-assisted intrinsic photoresponse in graphene. *Science (New York, N.Y.)*, 334(6056):648–52, November 2011.

[18] A K Geim. Graphene: status and prospects. *Science (New York, N.Y.)*, 324(5934):1530–4, June 2009.

[19] A K Geim and I V Grigorieva. Van der Waals heterostructures. *Nature*, 499(7459):419–25, July 2013.

[20] M. O. Goerbig. Electronic properties of graphene in a strong magnetic field. *Reviews of Modern Physics*, 83(4):1193–1243, November 2011.

[21] Matt W. Graham, Su-Fei Shi, Daniel C. Ralph, Jiwoong Park, and Paul L. McEuen. Photocurrent measurements of supercollision cooling in graphene. *Nature Physics*, 9(2):103–108, December 2012.

[22] O. Gunawan, Y. Shkolnikov, K. Vakili, T. Gokmen, E. De Poortere, and M. Shayegan. Valley Susceptibility of an Interacting Two-Dimensional Electron System. *Physical Review Letters*, 97(18):186404, November 2006.

[23] V. Gusynin and S. Sharapov. Unconventional Integer Quantum Hall Effect in Graphene. *Physical Review Letters*, 95(14):146801, September 2005.

[24] Lei Hao and T. K. Lee. Thermopower of gapped bilayer graphene. *Physical Review B*, 81(16):1–8, April 2010.

[25] Keliang He, Nardeep Kumar, Liang Zhao, Zefang Wang, Kin Fai Mak, Hui Zhao, and Jie Shan. Tightly Bound Excitons in Monolayer WSe2. *Physical Review Letters*, 113(2):026803, July 2014.

[26] B Hunt, J D Sanchez-Yamagishi, A F Young, M Yankowitz, B J Leroy, K Watanabe, T Taniguchi, P Moon, M Koshino, P Jarillo-Herrero, and R C Ashoori. Massive Dirac Fermions and Hofstadter Butterfly in a van der Waals Heterostructure. *Science (New York, N.Y.)*, May 2013.

[27] Z. Jiang, E. A. Henriksen, L. C. Tung, Y.-J. Wang, M. E. Schwartz, M. Y. Han, P. Kim, and H. L. Stormer. Infrared Spectroscopy of Landau Levels of Graphene. *Physical Review Letters*, 98(19):197403, May 2007.

[28] Aaron M Jones, Hongyi Yu, Nirmal J Ghimire, Sanfeng Wu, Grant Aivazian, Jason S Ross, Bo Zhao, Jiaqiang Yan, David G Mandrus, Di Xiao, Wang Yao, and Xiaodong Xu. Optical generation of excitonic valley coherence in monolayer WSe2. *Nature nanotechnology*, 8(9):634–8, September 2013.

[29] M.-H. Kim, J. Yan, R. J. Suess, T. E. Murphy, M. S. Fuhrer, and H. D. Drew. Photothermal Response in Dual-Gated Bilayer Graphene. *Physical Review Letters*, 110(24):247402, June 2013.

[30] D. Kleinman and R. Miller. Band-gap renormalization in semiconductor quantum wells containing carriers. *Physical Review B*, 32(4):2266–2272, August 1985.

[31] K. Klitzing, G. Dorda, and M. Pepper. New Method for High-Accuracy Determination of the Fine-Structure Constant Based on Quantized Hall Resistance. *Physical Review Letters*, 45(6):494–497, August 1980.

[32] Andor Kormányos, Viktor Zólyomi, Neil D. Drummond, Péter Rakyta, Guido Burkard, and Vladimir I. Fal'ko. Monolayer MoS2: Trigonal warping, the Γ valley, and spin-orbit coupling effects. *Physical Review B*, 88(4):045416, July 2013.

[33] D. Lagarde, L. Bouet, X. Marie, C. R. Zhu, B. L. Liu, T. Amand, P. H. Tan, and B. Urbaszek. Carrier and Polarization Dynamics in Monolayer MoS2. *Physical Review Letters*, 112(4):047401, January 2014.

[34] R. Laughlin. Quantized Hall conductivity in two dimensions. *Physical Review B*, 23(10):5632–5633, May 1981.

[35] Michele Lazzeri, Claudio Attaccalite, Ludger Wirtz, and Francesco Mauri. Impact of the electron-electron correlation on phonon dispersion: Failure of LDA and GGA DFT functionals in graphene and graphite. *Physical Review B*, 78(8):081406, August 2008.

[36] Max C Lemme, Frank H L Koppens, Abram L Falk, Mark S Rudner, Hongkun Park, Leonid S Levitov, and Charles M Marcus. Gate-activated photoresponse in a graphene p-n junction. *Nano letters*, 11(10):4134–7, October 2011.

[37] Yilei Li, Jonathan Ludwig, Tony Low, Alexey Chernikov, Xu Cui, Ghidewon Arefe, Young Duck Kim, Arend M. van der Zande, Albert Rigosi, Heather M. Hill, Suk Hyun Kim, James Hone, Zhiqiang Li, Dmitry Smirnov, and Tony F. Heinz. Valley Splitting and Polarization by the Zeeman Effect in Monolayer MoSe2. *Physical Review Letters*, 113(26):266804, December 2014.

[38] Gui-Bin Liu, Wen-Yu Shan, Yugui Yao, Wang Yao, and Di Xiao. Three-band tight-binding model for monolayers of group-VIB transition metal dichalcogenides. *Physical Review B*, 88(8):085433, August 2013.

[39] David MacNeill, Colin Heikes, Kin Fai Mak, Zachary Anderson, Andor Kormányos, Viktor Zólyomi, Jiwoong Park, and Daniel C. Ralph. Breaking of Valley Degeneracy by Magnetic Field in Monolayer MoSe2. *Physical Review Letters*, 114(3):037401, January 2015.

[40] Cong Mai, Andrew Barrette, Yifei Yu, Yuriy G Semenov, Ki Wook Kim, Linyou Cao, and Kenan Gundogdu. Many-body effects in valleytronics: direct measurement of valley lifetimes in single-layer MoS2. *Nano letters*, 14(1):202–6, January 2014.

[41] K F Mak, K L McGill, J Park, and P L McEuen. Valleytronics. The valley Hall effect in MoS2 transistors. *Science (New York, N.Y.)*, 344(6191):1489–92, June 2014.

[42] Kin Mak, Chun Lui, Jie Shan, and Tony Heinz. Observation of an Electric-Field-Induced Band Gap in Bilayer Graphene by Infrared Spectroscopy. *Physical Review Letters*, 102(25):256405, June 2009.

[43] Kin Fai Mak, Keliang He, Changgu Lee, Gwan Hyoung Lee, James Hone, Tony F Heinz, and Jie Shan. Tightly bound trions in monolayer MoS2. *Nature materials*, 12(3):207–11, March 2013.

[44] Kin Fai Mak, Keliang He, Jie Shan, and Tony F Heinz. Control of valley polarization in monolayer MoS2 by optical helicity. *Nature nanotechnology*, 7(8):494–8, August 2012.

[45] Kin Fai Mak, Changgu Lee, James Hone, Jie Shan, and Tony F. Heinz. Atomically Thin MoS2: A New Direct-Gap Semiconductor. *Physical Review Letters*, 105(13):136805, September 2010.

[46] J. Maultzsch, S. Reich, C. Thomsen, H. Requardt, and P. Ordejón. Phonon Dispersion in Graphite. *Physical Review Letters*, 92(7):075501, February 2004.

[47] Edward McCann. Asymmetry gap in the electronic band structure of bilayer graphene. *Physical Review B*, 74(16):161403, October 2006.

[48] Hongki Min, Bhagawan Sahu, Sanjay Banerjee, and A. MacDonald. Ab initio theory of gate induced gaps in graphene bilayers. *Physical Review B*, 75(15):155115, April 2007.

[49] Martin Mittendorff, Florian Wendler, Ermin Malic, Andreas Knorr, Milan Orlita, Marek Potemski, Claire Berger, Walter A. de Heer, Harald Schneider, Manfred Helm, and Stephan Winnerl. Carrier dynamics in Landau-quantized graphene featuring strong Auger scattering. *Nature Physics*, 11(1):75–81, November 2014.

[50] Thomas Mueller, Fengnian Xia, and Phaedon Avouris. Graphene photodetectors for high-speed optical communications. *Nature Photonics*, 4(5):297–301, March 2010.

[51] Seung-Geol Nam, Dong-Keun Ki, and Hu-Jong Lee. Thermoelectric transport of massive Dirac fermions in bilayer graphene. *Physical Review B*, 82(24):245416, December 2010.

[52] G. Nazin, Y. Zhang, L. Zhang, E. Sutter, and P. Sutter. Visualization of charge transport through Landau levels in graphene. *Nature Physics*, 6(11):870–874, August 2010.

[53] K S Novoselov, A K Geim, S V Morozov, D Jiang, M I Katsnelson, I V Grigorieva, S V Dubonos, and A A Firsov. Two-dimensional gas of massless Dirac fermions in graphene. *Nature*, 438(7065):197–200, November 2005.

[54] K S Novoselov, A K Geim, S V Morozov, D Jiang, Y Zhang, S V Dubonos, I V Grigorieva, and A A Firsov. Electric field effect in atomically thin carbon films. *Science (New York, N.Y.)*, 306(5696):666–9, October 2004.

[55] K S Novoselov, D Jiang, F Schedin, T J Booth, V V Khotkevich, S V Morozov, and A K Geim. Two-dimensional atomic crystals. *Proceedings of the National Academy of Sciences of the United States of America*, 102(30):10451–3, July 2005.

[56] KS Novoselov, Z Jiang, and Y Zhang. Room-temperature quantum Hall effect in graphene. *Science*, 315(March):2007, 2007.

[57] P. Plochocka, P. Kossacki, A. Golnik, T. Kazimierczuk, C. Berger, W. A. de Heer, and M. Potemski. Slowing hot-carrier relaxation in graphene using a magnetic field. *Physical Review B*, 80(24):245415, December 2009.

[58] Antonio Politano, Antonio Raimondo Marino, and Gennaro Chiarello. Phonon dispersion of quasi-freestanding graphene on Pt(111). *Journal of physics. Condensed matter : an Institute of Physics journal*, 24(10):104025, March 2012.

[59] Ashwin Ramasubramaniam. Large excitonic effects in monolayers of molybdenum and tungsten dichalcogenides. *Physical Review B*, 86(11):115409, September 2012.

[60] Pasqual Rivera, John R Schaibley, Aaron M Jones, Jason S Ross, Sanfeng Wu, Grant Aivazian, Philip Klement, Kyle Seyler, Genevieve Clark, Nirmal J Ghimire, Jiaqiang Yan, D G Mandrus, Wang Yao, and Xiaodong Xu. Observation of long-lived interlayer excitons in monolayer MoSe2-WSe2 heterostructures. *Nature communications*, 6:6242, January 2015.

[61] G. Rochat, C. Ciuti, V. Savona, C. Piermarocchi, A. Quattropani, and P. Schwendimann. Excitonic Bloch equations for a two-dimensional system of interacting excitons. *Physical Review B*, 61(20):13856–13862, May 2000.

[62] Jason S Ross, Philip Klement, Aaron M Jones, Nirmal J Ghimire, Jiaqiang Yan, D G Mandrus, Takashi Taniguchi, Kenji Watanabe, Kenji Kitamura, Wang Yao, David H Cobden, and Xiaodong Xu. Electrically tunable excitonic light-emitting diodes based on monolayer WSe2 p-n junctions. *Nature nanotechnology*, 9(4):268–72, April 2014.

[63] Jason S. Ross, Sanfeng Wu, Hongyi Yu, Nirmal J. Ghimire, Aaron M. Jones, Grant Aivazian, Jiaqiang Yan, David G. Mandrus, Di Xiao, Wang Yao, and Xiaodong Xu. Electrical control of neutral and charged excitons in a monolayer semiconductor. *Nature Communications*, 4:1474, February 2013.

[64] M. L. Sadowski, G. Martinez, and M. Potemski. Landau Level Spectroscopy of Ultrathin Graphite Layers. *Physical Review Letters*, 97(26):266405, December 2006.

[65] G. Sallen, L. Bouet, X. Marie, G. Wang, C. R. Zhu, W. P. Han, Y. Lu, P. H. Tan, T. Amand, B. L. Liu, and B. Urbaszek. Robust optical emission polarization in MoS2 monolayers through selective valley excitation. *Physical Review B*, 86(8):081301, August 2012.

[66] H. C. Schneider and S. W. Koch. Excitation-induced dephasing in semiconductor quantum dots. *Physical Review B*, 70(23):235308, December 2004.

[67] Sangwan Sim, Jusang Park, Jeong-Gyu Song, Chihun In, Yun-Shik Lee, Hyungjun Kim, and Hyunyong Choi. Exciton dynamics in atomically thin MoS2: Interexcitonic interaction and broadening kinetics. *Physical Review B*, 88(7):075434, August 2013.

[68] Akshay Singh, Galan Moody, Sanfeng Wu, Yanwen Wu, Nirmal J. Ghimire, Jiaqiang Yan, David G. Mandrus, Xiaodong Xu, and Xiaoqin Li. Coherent Electronic Coupling in Atomically Thin MoSe2. *Physical Review Letters*, 112(21):216804, May 2014.

[69] JCW Song, MS Rudner, CM Marcus, and LS Levitov. Hot carrier transport and photocurrent response in graphene. *Nano letters*, pages 3–7, 2011.

[70] Justin C. W. Song, Michael Y. Reizer, and Leonid S. Levitov. Disorder-Assisted Electron-Phonon Scattering and Cooling Pathways in Graphene. *Physical Review Letters*, 109(10):106602, September 2012.

[71] Justin C. W. Song, Klaas J. Tielrooij, Frank H. L. Koppens, and Leonid S. Levitov. Photoexcited carrier dynamics and impact-excitation cascade in graphene. *Physical Review B*, 87(15):155429, April 2013.

[72] Andrea Splendiani, Liang Sun, Yuanbo Zhang, Tianshu Li, Jonghwan Kim, Chi-Yung Chim, Giulia Galli, and Feng Wang. Emerging photoluminescence in monolayer MoS2. *Nano letters*, 10(4):1271–5, April 2010.

[73] Ajit Srivastava, Meinrad Sidler, Adrien V. Allain, Dominik S. Lembke, Andras Kis, and A. Imamolu. Valley Zeeman effect in elementary optical excitations of monolayer WSe2. *Nature Physics*, January 2015.

[74] B. Sun, Y. Zhou, and M. Wu. Dynamics of photoexcited carriers in graphene. *Physical Review B*, 85(12):1–8, March 2012.

[75] Dong Sun, Grant Aivazian, Aaron M Jones, Jason S Ross, Wang Yao, David Cobden, and Xiaodong Xu. Ultrafast hot-carrier-dominated photocurrent in graphene. *Nature nanotechnology*, 7(2):114–8, March 2012.

[76] Dong Sun, Charles Divin, Claire Berger, Walt a. de Heer, Phillip N. First, and Theodore B. Norris. Hot carrier cooling by acoustic phonons in epitaxial graphene by ultrafast pump-probe spectroscopy. *Physica Status Solidi (C)*, 8(4):1194–1197, April 2011.

[77] Dong Sun, Zong-Kwei Wu, Charles Divin, Xuebin Li, Claire Berger, Walt de Heer, Phillip First, and Theodore Norris. Ultrafast Relaxation of Excited Dirac Fermions in Epitaxial Graphene Using Optical Differential Transmission Spectroscopy. *Physical Review Letters*, 101(15):157402, October 2008.

[78] F. Tassone and Y. Yamamoto. Exciton-exciton scattering dynamics in a semiconductor microcavity and stimulated scattering into polaritons. *Physical Review B*, 59(16):10830–10842, April 1999.

[79] K. J. Tielrooij, J. C. W. Song, S. A. Jensen, A. Centeno, A. Pesquera, A. Zurutuza Elorza, M. Bonn, L. S. Levitov, and F. H. L. Koppens. Photoexcitation cascade and multiple hot-carrier generation in graphene. *Nature Physics*, 9(4):248–252, February 2013.

[80] Andrea Tomadin, Daniele Brida, Giulio Cerullo, Andrea C. Ferrari, and Marco Polini. Nonequilibrium dynamics of photoexcited electrons in graphene: Collinear scattering, Auger processes, and the impact of screening. *Physical Review B*, 88(3):035430, July 2013.

[81] Wang-Kong Tse and S. Das Sarma. Energy relaxation of hot Dirac fermions in graphene. *Physical Review B*, 79(23):235406, June 2009.

[82] Alexander Urich, Karl Unterrainer, and Thomas Mueller. Intrinsic response time of graphene photodetectors. *Nano letters*, 11(7):2804–8, July 2011.

[83] Chang-Ran Wang, Wen-Sen Lu, Lei Hao, Wei-Li Lee, Ting-Kuo Lee, Feng Lin, I-Chun Cheng, and Jian-Zhang Chen. Enhanced Thermoelectric Power in Dual-Gated Bilayer Graphene. *Physical Review Letters*, 107(18):1–5, October 2011.

[84] Feng Wang, Yang Wu, Mark Hybertsen, and Tony Heinz. Auger recombination of excitons in one-dimensional systems. *Physical Review B*, 73(24):245424, June 2006.

[85] G. Wang, L. Bouet, D. Lagarde, M. Vidal, A. Balocchi, T. Amand, X. Marie, and B. Urbaszek. Valley dynamics probed through charged and neutral exciton emission in monolayer WSe2. *Physical Review B*, 90(7):075413, August 2014.

[86] G. Wang, X. Marie, I. Gerber, T. Amand, D. Lagarde, L. Bouet, M. Vidal, A. Balocchi, and B. Urbaszek. Non-linear Optical Spectroscopy of Excited Exciton States for Efficient Valley Coherence Generation in WSe2 Monolayers. March 2014.

[87] Qinsheng Wang, Shaofeng Ge, Xiao Li, Jun Qiu, Yanxin Ji, Ji Feng, and Dong Sun. Valley carrier dynamics in monolayer molybdenum disulfide from helicity-resolved ultrafast pump-probe spectroscopy. *ACS nano*, 7(12):11087–93, December 2013.

[88] Torben Winzer and E MaliÄ. Impact of Auger processes on carrier dynamics in graphene. *Physical Review B*, (1):1–4, 2012.

[89] Sanfeng Wu, Chunming Huang, Grant Aivazian, Jason S Ross, David H Cobden, and Xiaodong Xu. Vapor-solid growth of high optical quality MoS2 monolayers with near-unity valley polarization. *ACS nano*, 7(3):2768–72, March 2013.

[90] Sanfeng Wu, Jason S. Ross, Gui-Bin Liu, Grant Aivazian, Aaron Jones, Zaiyao Fei, Wenguang Zhu, Di Xiao, Wang Yao, David Cobden, and Xiaodong Xu. Electrical tuning of valley magnetic moment through symmetry control in bilayer MoS2. *Nature Physics*, 9(2):1–5, January 2013.

[91] Di Xiao, Ming-Che Chang, and Qian Niu. Berry phase effects on electronic properties. *Reviews of Modern Physics*, 82(3):1959–2007, July 2010.

[92] Di Xiao, Gui-Bin Liu, Wanxiang Feng, Xiaodong Xu, and Wang Yao. Coupled Spin and Valley Physics in Monolayers of MoS2 and Other Group-VI Dichalcogenides. *Physical Review Letters*, 108(19):196802, May 2012.

[93] Di Xiao, Wang Yao, and Qian Niu. Valley-Contrasting Physics in Graphene: Magnetic Moment and Topological Transport. *Physical Review Letters*, 99(23):236809, December 2007.

[94] Xiaodong Xu, Nathaniel M Gabor, Jonathan S Alden, Arend M van der Zande, and Paul L McEuen. Photo-thermoelectric effect at a graphene interface junction. *Nano letters*, 10(2):562–6, February 2010.

[95] Xiaodong Xu, Wang Yao, Di Xiao, and Tony F. Heinz. Spin and pseudospins in layered transition metal dichalcogenides. *Nature Physics*, 10(5):343–350, April 2014.

[96] Jiamin Xue, Javier Sanchez-Yamagishi, Danny Bulmash, Philippe Jacquod, Aparna Deshpande, K Watanabe, T Taniguchi, Pablo Jarillo-Herrero, and Brian J LeRoy. Scanning tunnelling microscopy and spectroscopy of ultra-flat graphene on hexagonal boron nitride. *Nature materials*, 10(4):282–5, April 2011.

[97] Jun Yan, M-H Kim, J A Elle, A B Sushkov, G S Jenkins, H M Milchberg, M S Fuhrer, and H D Drew. Dual-gated bilayer graphene hot-electron bolometer. *Nature nanotechnology*, 7(7):472–8, January 2012.

[98] Matthew Yankowitz, Jiamin Xue, Daniel Cormode, Javier D. Sanchez-Yamagishi, K. Watanabe, T. Taniguchi, Pablo Jarillo-Herrero, Philippe Jacquod, and Brian J. LeRoy. Emergence of superlattice Dirac points in graphene on hexagonal boron nitride. *Nature Physics*, 8(5):382–386, March 2012.

[99] Wang Yao, Di Xiao, and Qian Niu. Valley-dependent optoelectronics from inversion symmetry breaking. *Physical Review B*, 77(23):235406, June 2008.

[100] Hongyi Yu, Gui-Bin Liu, Pu Gong, Xiaodong Xu, and Wang Yao. Dirac cones and Dirac saddle points of bright excitons in monolayer transition metal dichalcogenides. *Nature communications*, 5:3876, January 2014.

[101] Hualing Zeng, Junfeng Dai, Wang Yao, Di Xiao, and Xiaodong Cui. Valley polarization in MoS2 monolayers by optical pumping. *Nature nanotechnology*, 7(8):490–3, August 2012.

[102] L. Zhang, Z. Li, D. Basov, M. Fogler, Z. Hao, and M. Martin. Determination of the electronic structure of bilayer graphene from infrared spectroscopy. *Physical Review B*, 78(23):235408, December 2008.

[103] Y. Zhang, Z. Jiang, J. P. Small, M. S. Purewal, Y.-W. Tan, M. Fazlollahi, J. D. Chudow, J. a. Jaszczak, H. L. Stormer, and P. Kim. Landau-Level Splitting in Graphene in High Magnetic Fields. *Physical Review Letters*, 96(13):1–4, April 2006.

[104] Yuanbo Zhang, Yan-Wen Tan, Horst L Stormer, and Philip Kim. Experimental observation of the quantum Hall effect and Berry's phase in graphene. *Nature*, 438(7065):201–4, November 2005.

[105] Yuanbo Zhang, Tsung-Ta Tang, Caglar Girit, Zhao Hao, Michael C Martin, Alex Zettl, Michael F Crommie, Y Ron Shen, and Feng Wang. Direct observation of a widely tunable bandgap in bilayer graphene. *Nature*, 459(7248):820–3, June 2009.

[106] Z. Y. Zhu, Y. C. Cheng, and U. Schwingenschlögl. Giant spin-orbit-induced spin splitting in two-dimensional transition-metal dichalcogenide semiconductors. *Physical Review B*, 84(15):153402, October 2011.

VITA

Grant was born in Casper, Wyoming in 1987 to Tammie and Bryan Aivazian, school teachers of unquestionable reputation. He learned to walk; he learned to ski; he learned to rock out on the trombone; and somewhere along the way learned that this physics thing was pretty interesting. After graduating from Natrona County High School, he ventured down to the hippy stronghold of University of Colorado- Boulder (GO BUFFS!) to pursue a degree in physics and rock out some more on the trombone. A few years, a little physics, and a lot of beer later he graduated and headed west to the rain and to the University of Washington- Seattle. A few more years, a little more physics, and *a lot* more beer later he got his PhD in physics and the rest is history. He lives happily ever after with his wife, his dog, and his trombone— and quite a bit of beer.